UCLouvain

epl

École polytechnique de Louvain

Experimental biomechanics – Microstructural assessment of the mitral valve chordae tendineae based on CECT and cryo-CECT

Author: **Brice WAUTERS**
Supervisor: **Greet KERCKHOFS**
Readers: **Delia HOFFMANN, Nele FAMAEY**
Academic year 2022–2023
Master [120] in Biomedical Engineering

Acknowledgments

First, I would like to thank my supervisor Prof. Greet Kerckhofs for her support this year. I would also like to thank her for her availability, during our regular meetings and for her constant feedback.
My gratitude also goes to Dr. Camille Pestiaux for her countless pieces of advice and for always identifying the "less good" in our work and guiding us to improve it. Her help during the scanning days, the processing and the writing of this master thesis was invaluable.
I would also like to thank Gregory Pyka for the 2 days of training on the Nanotom and help throughout the optimization of the sample holder and acquisition parameters. Overall, I would also like to thank all the contrastTeam members for their insights and help.
On a more personal note, I would like to thank Guillaume and Alexandra for their support and help during this year.

Abstract

The microstructure of chordae tendineae, crucial fibrous components of the mitral valve apparatus, plays a significant role in maintaining proper cardiac function by transmitting force from the papillary muscles to the leaflets and allowing the closing/opening of the mitral valve. In this master thesis, we aimed to assess the microstructure of chordae tendineae using CECT and cryo-CECT imaging, which offer detailed 3D visualization and analysis of soft tissues. Our study involved the development of an optimized sample preparation and imaging protocol, enabling high-resolution imaging of chordae tendineae microstructure. Through 3D imaging and analysis, we aimed to uncover new insights into the microstructural composition of the mitral valve chordae tendineae, their tissue characteristics, and potential variations within and among individuals. By comparing the imaging data obtained from CECT and cryo-CECT, we observed complementary information regarding the microstructure of chordae tendineae. CECT at low- and high-resolution enables the assessment of the macroscopic organisation and general morphology of the chordae tendineae, and the characterization of the microstructure of the chordae tendineae, respectively. CECT could, hence, be used to characterize substructures of the chordae tendineae e.g., the adipocytes and blood vessels. Cryo-CECT allowed for the visualization of fine-scale features such as fibrous organization. Hence, cryo-CECT should, thus, be preferred to study the structure and organization of the fibres, i.e., collagen, elastin and muscle fibres. However, cryo-CECT exhibited limitations notably decreasing the visibility of the vessels in the muscle tissue and inducing CESA segregation in the adipocytes.

This study serves as a proof of concept for the application of cryo-CECT and CECT in assessing chordae tendineae microstructure. Our findings contribute to a deeper understanding of the structural characteristics and variations within these essential cardiac structures. It opens the path to further studies that can expand our knowledge and explore the potential clinical significance of microstructural variations. Future investigations may focus on comparative studies involving different types of chordae tendineae, evaluation of microstructural changes under specific loading conditions, and examination of the relationship between microstructure and disease progression.

List of Figures

2.1 **Overview of the vascular apparatus anatomy and functioning**. (a) A schematic cross-sectional view of the heart and its anatomy (adapted from [1]). (b) Diastole and systole steps with the opening/closing stages of the valves (adapted from [2]). (c) Pulmonary and systemic circulation (adapted from [1]). 3

2.2 **Overview of the mitral valve components.** (a) Apical view of the heart, the mitral valve is on the right with the Carpentier's nomenclature (adapted from [3]). (b) Top view of the two leaflets, with the Carpentier's nomenclature, the posterior (P) and anterior (A). The posterior leaflet is divided into three different sections (P1, P2, P3). The anterior region is also divided into three regions (A1, A2, A3). Clefts are located between P1/P2 and P2/P3. The commissures are observed at the joint between the anterior and posterior leaflet (adapted from [4]). (c) Zoom on the commissural area. (d) Coaptation zone of the leaflet. (e) Annulus. (f) Subvalvular apparatus with the chordae tendineae and the two groups of papillary muscles (adapted from [5]). 4

2.3 **Anatomical overview of the MV leaflets.** Diagram of a typical mitral valve. The space between B and C is the anterior leaflet, and between D and A' posterior leaflet; c = cleft; pm = papillary muscle.3 zones are described in the leaflets, the basal zone (dotted area), the rough zone (cross-hatched), and the clear zones (blank in between) (adapted from [6]). . . . 5

2.4 **Microstructural overview of the MV leaflets.** (a) Four leaflet layers. A is the atrialis, S, is the spongiosa, F, is the fibrosa, and V, is the ventricularis (adapted from [7]). (b) Collagen fibres orientation (adapted from [8]). 5

2.5 **PM and chordae tendineae functioning.** (A) The heart muscle relaxes. The pressure in the atrium is higher than in the ventricle, the blood flows from the atrium to the ventricle. The MV is open, and the PM and chordae tendineae are loose. (B) Leaflets are not fully opened. (C) Atrial contraction, blood flows from the atrium to the ventricle. The MV is open and the PM and chordae tendineae are tense. (D) Ventricular contraction, leaflets are closed due to the severe pressure change. PMs and chordae are tensed in order to prevent prolapse of the leaflet and regurgitation. (E) The opening of the aortic valve by pressure gradient allows the blood to flow from the ventricle to the aorta. The PMs and chordae are still tense. (adapted from[9]) 6

2.6 **Different subset of chordae.** (a) Primary chordae are inserted in the free margin of the leaflet. Secondary chordae are attached on the rough zone of the leaflet (adapted from [5]). (b) 2 anterior strut chordae (black arrows)(adapted from [10]). 7

2.7 **Overview of the chordae tendineae microstructure.** (a) Schematic representation of a chordae tendineae and its different layers. (b) SEM images of the mitral valve, from top to bottom, a layer of endothelial cells, elastin fibres, and crimped collagen fibres (adapted from [11]). (c) Crimping direction of the collagen fibres (adapted from [12]). 8

2.8 **Chordae insertion site into the ventricular side of the leaflet.**(a) Schematic representation of the collagen fibres at the insertion site distribution. Collagen fibres go from vertically aligned to horizontal (adapted from [13]). (b) Electron micrograph of the insertion of the chordae in the leaflet. Fb represents the fibrosa extending from the chordae core with collagen fibres reorienting themselves to merge into the fibrosa of the leaflet. C, the collagen fibres. El, the elastic fibres. F, a fibroblast (adapted from [14]). 9

2.9 **Chordae insertion site into the PM.** (a) Longitudinal section with the chordae tissue (CT) and the papillary muscle (M). The arrows represent the penetration of the fibrous tissue of the chordae into the muscle. (b) Chordae collagen fibres digging into the PM. Collagen fibres lose their packed structure while digging into the PM. (Cp) small capillaries, (F) fibroblast, (c) Basal lamina, (BL) with microfibrils. In the end, the collagen fibres (C) are bound to microfibrils (MF) of the basal lamina (adapted from [13]). 10

2.10 **Blood vessel in the chordae tendineae.** (a) Classical 2D histological section of a chordae tendineae with white dots that are the blood vessels. (b) The wavy shape of the blood vessel in the chordae is based on classical 2D histology (adapted from [12]). 11

2.11 **Sections of chordae from different chordal types.** While the global structure with core and elastin layers can be seen, the shape and size of those regions vary between chordae types. The microstructure varies particularly in the posterior basal chordae referred to as second order and in the marginal or second order chordae with unorganized collagen fibres or separated core and elastin layers. (adapted from [15]). 12

2.12 **Classical 2D histological section of degenerative chordae.** (a) In the above picture, S represents the elastin-rich regions separating from the chorda. Arrows show elastin accumulation. Below, the asterisk represents the rupture of the core, the black arrow shows the core that is retracting. It also shows the disorganization of the microstructure (scale: a, 250 [µm]; inset of a, 250 [µm]; b, 100 [µm]). (b) a and b are degenerative chordae, and c is healthy. The delimitation between the core and the elastin sheath is the darker circle shown with a black arrow. a and b exhibit multilayered and partially detached layers while c does not (scale = 100 [µm]) (adapted from [16]). 14

2.13 **BD and FDE anatomical and microstructural consequences in the leaflet**. (a) Anatomical differences between BD and FED. (b) In G, there is a formation of elastin plaques induced by BD. In H, there is an elastin deposition due to FED (adapted from [17]). 14

2.14 **Chordae repair technique using PTFE**.(a) Replacement of a first-order chordae using PTFE suture. (b) 2 PTFE and 1 native chordae after 9 months covered by fibrous tissue (c) Histological section of a PTFE chordae after 9 months with no cellular in or out the artificial chordae. months postoperatively.(adapted from [18]) 15

2.15 **CECT of a rat aorta using Hf-WD 1:2 POM**. The elastic fibres, collagen matrix, and adventitia are observable. The individual fibres are not visible (adapted from [19]). 18

2.16 **Fast vs low freezing rate of muscle tissue.** Slow freezing results in the formation of extracellular ice crystal nuclei outside of the muscle fibres while fast freezing leads to the formation of ice crystals inside and outside the muscle fibres. Ice crystals are homogeneously distributed in the tissue (adapted from [20]). 19

2.17 **Achilles tendon section using CECT and cryo-CECT.**(a) Comparison of the resolution using different freezing parameters and stained with Hf-WD 1:2 POM. The Slow freezing at −80℃ exhibits high contrast between the fibres. (red arrow) shows an individual collagen fibre and (blue arrow) a blood vessel. (b) Comparison of cryo-CECT result versus classical histology. (c) Individual collagen fibres 3D visualization (adapted from [20]). 20

4.1 **Sample holder n°1,*the toothpick*.** On the left the toothpick is inserted in the aluminium holder. The sample corresponds to the darker dot on the toothpick. The parafilm outer layer is also visible. 23

4.2 **Sample holder cross sections (I) and position of the sample (II) in the field of view (FOV).** (A) Cross section of the 1st sample holder (toothpick) with a diameter of 2 mm. The sample is not centred in the field of view. (B) Cross section of the 3rd sample holder (half toothpick) with a smaller radius below 1 mm. The sample is in the centre of the FOV. 23

5.1 **Visual assessment of the chordae anatomy and macromorphology.** (A) Mitral valve apparatus with the chordae used in this study, the white inset is shown in (B). (I) The anterior leaflet,(II) P1, the first anterior scallop of the posterior leaflet, (III) papillary muscle. (B) Chordae used in this study and dissected from the mitral valve (I) the posterior leaflet,(III) the PM and (IV) 2 chordae visible. 29

5.2 **Quantitative assessment of the chordae morphology.** (A) 3D rendering of the entire sample obtained with low-resolution CECT (protocol n°1). The white inset indicates the zoom region used in (B) where three chordae are visible. (B) 3D rendering of the zoomed region obtained with low-resolution CECT (protocol n°1) in which individual chordae are respectively named 1,2 and 3. Chorda 1 is represented in (C-E). (C) 3D rendering of the first chorda, the centerline (red) was used to assess the curved length of the chorda which is equal to 10.42 mm^2. (D) 3D rendering of chorda 1 coloured depending on the aspect ratio. (E) 3D rendering of the chorda 1 coloured depending on the cross-sectional area. The evolution of the axial cross-sectional area over the height of chorda 1 is observable. 31

5.3 **Qualitative comparison of the visibility and preservation of the adipocytes between different acquisition protocols.** (A-H) 2D axial section of the muscle insertion region containing adipocytes, obtained with low-resolution CECT (protocol n°1)(A-B), high-resolution CECT (protocol n°2)(C-D), high-resolution cryo-CECT (protocol n°3) (E-F) and high-resolution cryo CECT (protocol n°4) (G-H). The white inset shown on images of the left column corresponds to the zoom region used in the right column. (B) shows the zoomed region with low contrast between the adipocytes and the surrounding tissue due to partial volume effect, (D) the zoomed region, where there is satisfying contrast between the adipocytes and the surrounding tissue, and (F) where identifying individual adipocytes is difficult and a dark region is observable (yellow arrow). In comparison to (E), individual adipocytes are identifiable more easily in (H) and a dark region is also shown (yellow arrow). (I) 3D rendering of the entire sample obtained with low-resolution CECT (protocol n°1). The white dotted line indicates the location of the axial regions used in (A-H). 32

5.4 **Qualitative assessment of the location and packing of the adipocytes.** (A)3D rendering of the entire sample obtained with low-resolution CECT (protocol n°1). The white inset indicates the zoom region used in (B) where most of the identified adipocytes lie. (B) 3D rendering of the zoomed region obtained with high-resolution CECT (protocol n°2) in which individual adipocytes are represented in different colours. 34

5.5 **Quantitative assessment of the sphericity and volume of individual adipocytes.**(A) 3D rendering of the zoomed region represented in the white inset in (Fig.5.4.A) obtained with high-resolution CECT (protocol n°1), individual adipocytes are coloured depending on their sphericity, red adipocytes have high sphericity while blue has lower one. The sphericity varies from 0.3 to 0.9 [-], and the mean sphericity is 0.64. (B) 3D rendering of the zoomed region (Fig.5.4.A) obtained with high-resolution CECT (protocol n°2), individual adipocytes are coloured depending on their volume, red adipocytes have a bigger volume. The volume varies from 0 to 0.5 um^3. The colourmap upper limit is 0.2 um^3 in order to highlight the variability between smaller individual adipocytes. The mean volume is 0.05 um^3. 35

5.6 **Qualitative comparison of the visibility and preservation of the fibres.** (A-F) 2D sagital section of the muscle insertion region obtained with low-resolution CECT (protocol n°1) (A-D), high-resolution CECT (protocol n°2) (B-E) and high-resolution cryo-CECT (protocol n°4). (A) Sagital section of the sample with visible beam-hardening, in the dotted white inset. (D) Zoomed region where the chorda is homogeneously grey and no fibres are visible. (E) No fibres are visible but in comparison to (D), the centre of the chorda is not homogenously grey. (F) Individual fibres are observable and have a crimped shape. 36

5.7 **Qualitative assessment of the fibre organisation and orientation.**(A)3D rendering of the muscle insertion obtained with high-resolution cryo-CECT (protocol n°4). The white line indicates the position of the cut in (B) where the fibre organisation and orientation is observable. (B) 2D sagittal section showed in (A), the organisation of the fibre is visible with a region more densely packed and crimped (I), a looser and less crimped region (II), the muscle fibres (III) and outer sheaths (IV). 37

5.8 **Quantitative assessment of the orientation of the muscle and collagen fibres.** (A) 3D rendering of the muscle insertion obtained with high-resolution cryo-CECT (protocol n°4). Segments oriented in the direction of local orientation are visible and coloured based on their phi orientation. In the white inset, an interpretation of the phi orientation and the colourmap is represented, hot tones mean that the segments are oriented in the xy-plane . (B) 3D rendering of the muscle insertion obtained with high-resolution cryo-CECT (protocol n°4). Segments oriented in the direction of local orientation are visible and coloured based on their theta orientation. In the white inset, an interpretation of the theta orientation and the colourmap is represented, cold tones mean that the segments are oriented in the yz-plane. 38

5.9 **Qualitative assessment of the phi orientation of the muscle and collagen fibres.** (A) 3D rendering of the muscle insertion obtained with high-resolution cryo-CECT (protocol n°4) from an axial point of view, the coloured segments are visible and in the middle of the muscle insertion, blue segments are located in the centre of the chordae. (B) 3D rendering of the muscle insertion obtained with high-resolution cryo-CECT (protocol n°4) represented in (A), both chordae are visible at the left. (C) 3D rendering of the muscle insertion obtained with high-resolution cryo-CECT (protocol n°4) from a sagittal point of view, the coloured segments are visible and in the middle of the muscle insertion, blue segments are located in the centre lower part of the chorda visible, the orientation change from the muscle to the chorda is visible with muscle fibres gradually changing orientation from horizontal to vertical. (D) 3D rendering of the muscle insertion obtained with high-resolution cryo-CECT (protocol n°4) from a sagital point of view represented in (C), the chorda centre is darker and the fibre orientation is visible. The phi orientation variation through the sample can be found in the supplemental video (Supplementary video 3 [link: Video 3]). 38

5.10 **Qualitative assessment of the theta orientation of the muscle and collagen fibres.** (A) 3D rendering of the muscle insertion obtained with high-resolution cryo-CECT (protocol n°4) from an axial point of view, the coloured segments are visible.(B) 3D rendering of the muscle insertion obtained with high-resolution cryo-CECT (protocol n°4) represented in (A), both chordae are visible at the left. (C) 3D rendering of the muscle insertion obtained with high-resolution cryo-CECT (protocol n°4) from a sagital point of view, the coloured segments are visible. (D) 3D rendering of the muscle insertion obtained with high-resolution cryo-CECT (protocol n°4) from a sagital point of view represented in (C), the chorda centre is darker and the fibre orientation is visible. The theta orientation variation through the sample can be found in the supplemental video (Supplementary video 4 [link: Video 4]). 39

5.11 **Qualitative analysis of the muscle fibres visibility and segmentation**(A) 2D axial section of the muscle insertion region with cryo-CECT (protocol n°3). (B) 2D axial section of the zoomed region. (C) 3D rendering of the zoomed region, (light blue) muscle fibres; (dark blue) blood vessels. 40

5.12 **Qualitative comparison of the junctional zone between acquisition protocols.**(A) 2D axial section of the muscle insertion obtained with high-resolution CECT mounted on the full toothpick (protocol n°2). The white inset is the zoom region shown in (D) with the junctional zone visible. (B) 2D axial section of the muscle insertion obtained with high-resolution cryo-CECT mounted on the full toothpick (protocol n°3). The white inset is the zoom region shown in (E) with the junctional zone visible. (C) 2D axial section of the muscle insertion obtained with high-resolution cryo-CECT mounted on the half toothpick (protocol n°4). The white inset is the zoom region shown in (F) with the junctional zone not visible and the two chordae are less stretched apart in comparison with (A) and (B). (D) In the zoomed region shown in (A), the junctional zone is overall homogeneously and comprised of vessels and fat droplets. (E) The zoomed region shown in (B), the junctional zone is composed of bright elastin fibres and dark interstitial spaces, vessels and fat droplets are also present. (F) Zommed on the junctional region shown in (C), the junctional zone is not visible and should be located at the indicated position (yellow arrow). 41

5.13 **Comparison of the vessels visible between CECT and cryo-CECT, and vessels of different sizes.** (A-D) 2D axial sections of the muscle insertion region with high-resolution CECT (protocol n°2), the white insets visible in (A) represent from left to right the vessels zoomed in (D), (B) and (C). (B) the large vessel is shown in (A). (C) Medium size vessel shown in (A), the lumen of the vessel is not clearly visible. (D) A small vessel running into the chorda appears as a bright and blurry dot. (E-H) 2D axial sections of the muscle insertion region were obtained with high-resolution cryo-CECT (protocol n°3) with the white insets indicating the 3 vessels of varying sizes corresponding to vessels shown in (A) and represented in (F-G-H). (F) The large vessel is shown in (E). (G) In the medium-sized vessel shown in (E), the vessel wall can be separated from the surrounding tissue and the lumen. (H) Small vessel running into the chorda shown in (E). 42

5.14 **Quantitative comparison of the fibre visibility based on the number of observable vessels and contrast in the muscle insertion.** (A)2D axial section of the muscle insertion region obtained with high-resolution CECT (protocol n°2) where there is plenty of vessels corresponding to the bright dots. The white inset indicates the zoom region used in (C) where a vessel is present. (B) Approximately the same 2D axial section of the muscle insertion region showed in (A) obtained with high-resolution cryo-CECT (protocol n°3). There are few vessels observable in the muscle region. The white inset represents the zoomed region used in (E). (C) The zoomed vessel is visible with the line traced through the thickness of the vessel and surrounding tissue used to evaluate the grey-value intensity in (D). One bright region can be visually observed and correspond to the vessel. (D) Grey value evaluated over the line traced in (C), one peak is visible and corresponds to the vessel. (E)The zoomed vessel is visible with the line traced through the thickness of the vessel and surrounding tissue used to evaluate the grey-value intensity in (F). Different bright lines are visible and correspond to the walls of the vessel (1-2) and muscle fibre (3). (F) Grey value intensity variation along the line shown in (E), 3 peaks can be identified and correspond to the vessel walls and muscle fibre visible in (E). 43

5.15 **Quantitative assessment of the curved length and mean radius of the vessels running into the chordae.** (A)3D rendering of the vessels segmented in the full volume of the sample obtained with low-resolution CECT. The surface of the sample is coloured orange and the vessels are white. A vessel runs through the left chorda until the middle of its length. Two vessels appear running respectively in the left and right chord. (B) 3D rendering of the muscle insertion region obtained with high-resolution cryo-CECT (protocol n°4), the muscle is segmented (pink), and the segmented vessels are visible (blue). 3 vessels are observable running along the chordae (yellow arrow). (C) 3D rendering of the two blood vessels quantitatively studied in (D-E) and shown in (B). (D) The curved length of the individual segments is represented and ranges from 0.12 to 1.9 mm. (C) The mean radius of the segments is visible, and the largest values are attributed to the upper segments. The full segmented vessel network using high-resolution CECT (protocol n°2) is available in the supplemental video (Supplementary video 5 [link: Video 5]). 45

5.16 **Qualitative and quantitative assessment of the leaflet insertion of the chordal layers visibility and the number of chordae tendineae.** In (B-C-D-G), (I) indicates the darker layers referred to as the fibrosa, (II) to the lighter layer, referred to as the spongiosa and (III) the thin surrounding lighter layer referred to as the ventricularis, atrialis or endothelial cells. (A) 3D rendering of the leaflet insertion region with high-resolution cryo-CECT (protocol n°4). (B) Axial section in the upper part of the region, (C) Axial section in the middle part of the region. (D) An axial section in the bottom part of the region. (E) 3D rendering of individually segmented chordae. (F) Sagital section of the leaflet insertion. (G) 3D subvolume with both layers visible. 47

5.17 **Quantitive and qualitative assessment of the number of elastin laminae.**(A) 3D rendering of a chorda above muscle insertion. (B)The 2D axial section of the chorda is shown in (A). (C) Oversaturated section with three sections (x,y,z) and the layers visible. (D) 3D rendering of a chorda below the leaflet insertion. (E) 2D axial section of the chorda is available in (D). (F) Variation of the number of layers from bottom to top in the 3 sections (x,y,z) visible above in (C). 48

List of Tables

2.1 **Micromorphometrical parameters of the leaflet four layers (adapted from [8]).** . . 5

4.1 **MicroCT acquisition parameters** 24

4.2 **MicroCT reconstruction parameters** 25

List of abbreviations and symbols

µCT Microfocus X-ray computed tomography

BD Barlow's disease

CECT Contrast-enhanced computed tomography

CESA X-ray contrast-enhancing staining agents

CMR Cardiac magnetic resonance imaging

cryo-CECT Contrast-enhanced µCT with cryogenic sample preparation

ECM Extracellular matrix

FED Fibroelastic defficiency

FF Fast freezing

FOV Field of view

GAGs Glycosaminoglycans

HE Hematoxylin and eosin

Hf-WD 1:2 POM (1:2) Hafnium substituted Wells-Dawson polyoxometalate

MRI Magnetic resonance imaging

MV Mitral valve

PBS Phosphate-buffered saline solution

PET Positron emission tomography

PM Papillary muscle

POM Polyoxometalate

PTFE Polytetrafluoroethylene

ROI Region of interest

SEM Scanning electron microscopy

SPECT Single-photon emission computed tomography

TEE Transoesophageal echocardiography

TMVR Transcatheter mitral valve replacement

Disclaimer

In this master thesis, artificial intelligence, particularly OpenAI's ChatGPT, was used as a tool for writing assistance. It facilitated text revision and overall stylistic improvements. It is important to note that no experimental results were obtained using AI, and as the author, I take full responsibility for the content of this thesis.

Contents

Acknowledgments ii

Abstract iii

List of figures xi

List of tables xii

List of abbreviations and symbols xiii

Disclaimer xiv

Contents xvii

1 Introduction 1

2 State of the art 2

2.1 Heart . . . 2

2.2 Mitral valve . . . 3

2.2.1 Annulus . . . 3

2.2.2 Leaflets . . . 4

2.2.3 Papillary muscle . . . 5

2.2.4 Chordae tendineae . . . 6

2.2.4.1 Anatomy of the chordae tendineae . . . 7

2.2.4.2 Microstructure of the chordae tendineae . . . 8

2.2.4.2.1 General microstructure . . . 8

2.2.4.2.2 Chordae insertion into the leaflets . . . 9

2.2.4.2.3 Chordae insertion into the PM . . . 10

2.2.4.2.4 Chordae insertion into the heart wall . . . 10

2.2.4.2.5 Blood vessels . . . 10

2.2.4.3 Microstructural variations impact on the mechanical properties . . . 11
2.2.4.4 Microstructural variations between chordal types . . . 11
2.2.4.5 Microstructural variations between species . . . 12
2.2.4.6 Microstructural variations between healthy and diseased chordae tendineae . 13
2.2.5 Treatment of the MV and the chordae tendineae . . . 13
2.2.6 Computational modeling . . . 15
2.3 Imaging technique for chordae tendineae . . . 16
2.3.1 *In vivo* imaging . . . 16
2.3.2 2D histology . . . 17
2.3.3 X-ray based 3D histology . . . 18

3 Problem statement, aim and objectives **21**

4 Materials and methods **22**
4.1 Sample . . . 22
4.2 Sample preparation . . . 22
4.2.1 Sample fixation and CESA staining . . . 22
4.2.2 Sample mounting and holders . . . 22
4.2.3 Freezing protocol . . . 23
4.3 MicroCT acquisition parameters . . . 24
4.4 Reconstruction parameters . . . 24
4.5 Image processing and analysis . . . 25
4.5.1 Artefact removal . . . 25
4.5.2 Segmentation of the sample from the background . . . 25
4.5.3 Anatomical features and morphology . . . 25
4.5.4 Microstructure . . . 26
4.5.4.1 Adipocytes . . . 26
4.5.4.2 Muscle, collagen and elastin fibres orientation . . . 26
4.5.4.3 Vessels . . . 26
4.5.4.4 Muscle fibers . . . 27
4.5.5 Leaflet insertion . . . 27
4.5.6 Chordal layers . . . 27

5 Results and discussion **28**
5.1 Anatomical features and morphology . . . 28
5.2 Adipocytes . . . 31
5.2.1 Comparison between different acquisition protocols . . . 31
5.2.2 Microstructural assessment . . . 33
5.3 Muscle, collagen and elastin fibres organisation . . . 35
5.3.1 Comparison between acquisition protocols . . . 35

5.3.2 Microstructural assessment . . . 36
5.4 Muscle fibres . . . 39
5.5 Junctional zone . . . 40
5.6 Vessels . . . 41
5.6.1 Comparison between acquisition protocols . . . 41
5.6.2 Microstructural assessment of the vessel network . . . 44
5.7 Leaflet insertion . . . 46
5.8 Chordal layers . . . 48

6 General conclusion and further perspective **49**

1 Introduction

Chordae tendineae are essential components of the mitral valve apparatus, playing a crucial role in maintaining the proper functioning of the heart. These fibrous structures connect the papillary muscles to the leaflets of the mitral valve, ensuring the opening and closing of the valve during the cardiac cycle. Understanding the microstructure of chordae tendineae is of significant importance, as it provides insights into their mechanical properties, functional adaptations, and potential implications in various cardiac conditions such as degenerative and rheumatic diseases.

Classical 2D histology has provided valuable information about the microscopic organization of chordae tendineae but is limited by its 2D destructive nature. Hence, the complex 3D architecture and fine-scale features of these structures demand advanced imaging methods for a microstructural assessment. In recent years, 3D imaging techniques such as microfocus X-ray computed tomography (µCT) have emerged as powerful tools for non-destructive visualization and analysis of biological tissues at high resolution. Among these techniques, cryo-CECT (contrast-enhanced µCT with cryogenic sample preparation) and CECT (contrast-enhanced µCT) have been shown relevant for studying soft tissues and might be relevant for studying chordae tendineae.

The aim of this master thesis is to thoroughly investigate the microstructure of chordae tendineae using cryo-CECT and CECT imaging techniques to obtain detailed 3D representations of chordae tendineae, allowing the characterization of their structural components such as collagen and elastin fibres. Furthermore, this research aims to explore the potential applications of cryo-CECT and CECT in characterizing the chordae tendineae microstructure by analyzing and comparing the imaging data and identifying any intra-variability within the same chordae tendineae. Such knowledge can contribute to a better understanding of the functional adaptations, pathological changes, and clinical implications associated with the microstructural variations of chordae tendineae.

Overall, this master thesis strives to contribute to the existing knowledge of chordae tendineae microstructure and provide a foundation for future studies focusing on the role of these structures in cardiac biomechanics, disease mechanisms, and treatment strategies.

2 State of the art

2.1 Heart

The heart is a hollow muscular organ that pumps the blood carrying nutrients and oxygen into the circulatory system. The right and left sides of the heart are sagitally divided by the interventricular septum. It is composed of four chambers namely two ventricles and two atria. A valve is located at the exit of each heart chamber (Fig.2.1.a). In the left side of the heart, the atrium and the ventricle are separated by the mitral or bicuspid valve, and the aortic valve separates the ventricle and the aorta. Similarly, the right side of the heart contains the tricuspid and the pulmonary valves. Those four valves allow the unidirectional blood flow with a complex opening/closing mechanism based on pressure differences. The valves only open when the pressure in the previous heart chamber exceeds the next one. Then, they close as soon as the balance is inverted [21, 22, 23].

The cardiac cycle can be divided into two phases, the diastole and the systole (Fig.2.1.b). During the diastole, the blood flows from the atria to the ventricles through the two open atrioventricular valves. The two semilunar valves, the aortic and pulmonary valves are closed. During the second phase of the cardiac cycle, the systole, the blood flows from the ventricles to the arteries and the semilunar valves are thus open. The atrioventricular valves are closed in order to prevent the regurgitation of blood from the ventricles to the atria. Blood circulation is divided into the pulmonary and systemic circulation. The first happens in the left side of the heart and transports non-oxygenated blood to the lungs and re-oxygenated blood to the heart. The second takes place on the right side sending oxygenated blood to the rest of the body (Fig.2.1.c) [1, 2].

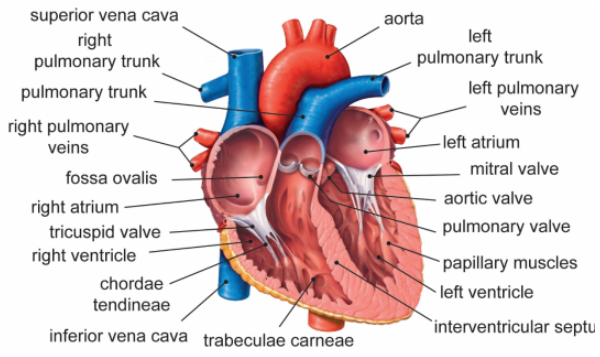

(a)

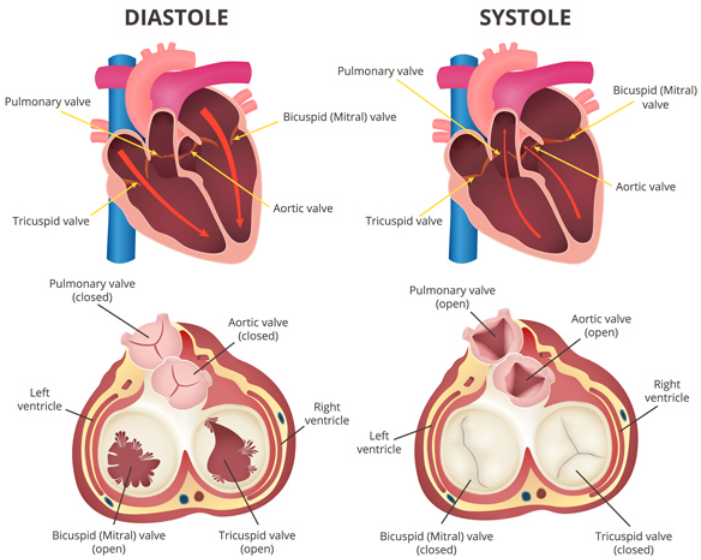

(b)

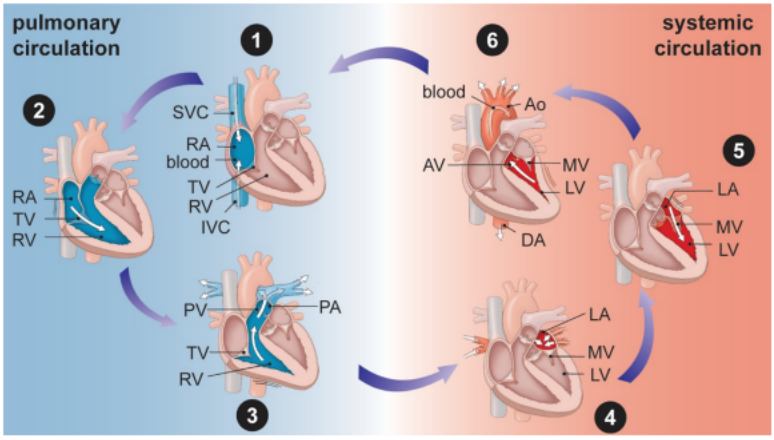

(c)

Figure 2.1: Overview of the vascular apparatus anatomy and functioning. (a) A schematic cross-sectional view of the heart and its anatomy (adapted from [1]). (b) Diastole and systole steps with the opening/closing stages of the valves (adapted from [2]). (c) Pulmonary and systemic circulation (adapted from [1]).

2.2 Mitral valve

The mitral valve (MV) is located in the left side of the heart between the ventricle and the atrium (Fig.2.2.a). It is composed of four elements namely the annulus, the leaflets, the chordae tendineae, and the papillary muscles (Fig.2).

2.2.1 Annulus

The annulus is a fibrous saddle-shaped structure that separates the left atrium and ventricle. The annulus also attaches the mitral valve leaflets to the heart wall [24, 25] and can be referred to as a transitional zone between the leaflet and the myocardium (Fig.2.2.e). It is mainly composed of collagen and elastin fibres [26].

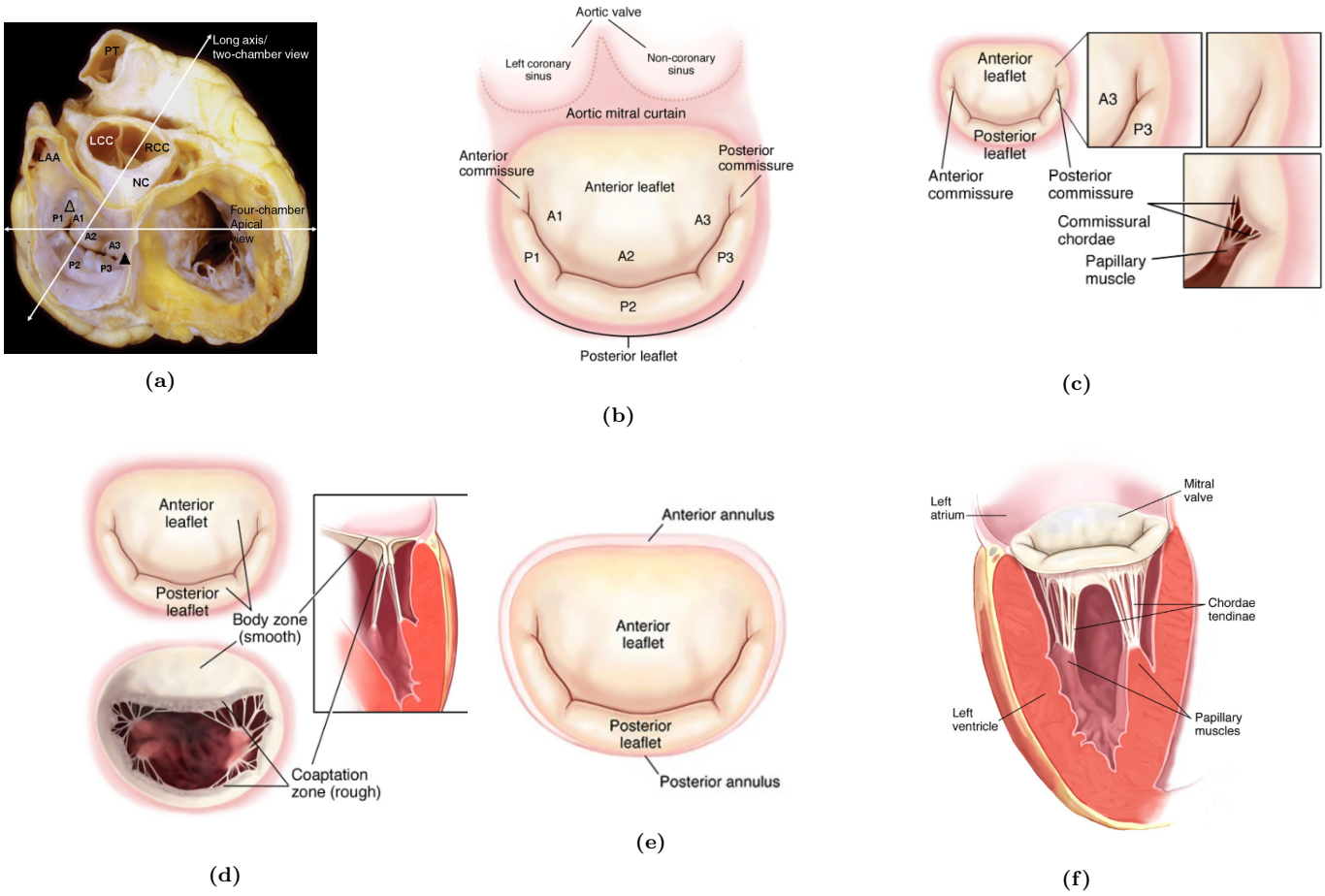

Figure 2.2: Overview of the mitral valve components. (a) Apical view of the heart, the mitral valve is on the right with the Carpentier's nomenclature (adapted from [3]). (b) Top view of the two leaflets, with the Carpentier's nomenclature, the posterior (P) and anterior (A). The posterior leaflet is divided into three different sections (P1, P2, P3). The anterior region is also divided into three regions (A1, A2, A3). Clefts are located between P1/P2 and P2/P3. The commissures are observed at the joint between the anterior and posterior leaflet (adapted from [4]). (c) Zoom on the commissural area. (d) Coaptation zone of the leaflet. (e) Annulus. (f) Subvalvular apparatus with the chordae tendineae and the two groups of papillary muscles (adapted from [5]).

2.2.2 Leaflets

The mitral valve is composed of two leaflets called anterior (or aortic) and posterior (or mural). They are mainly described using Carpentier's nomenclature that designates the anterior and posterior leaflets and divides them into three, i.e., A1, A2, and A3 for the anterior leaflet and similarly P1, P2, and P3 for the posterior. The three posterior parts are often divided by clefts (Fig.2.2.b) [25]. By convention, the leaflets can be divided into different zones named, basal, rough, and clear zones (Fig.2.3).

The leaflet microstructure is divided into four layers (Fig.2.4.a). From the atrial to the ventricular side, they are respectively the atrialis, the spongiosa, the fibrosa, and the ventricularis [8, 26]. The spongiosa is composed of loose collagen fibres, elastin and proteoglycan. The fibrosa is composed of dense wavy collagen fibres. The ventricularis and atrialis are described as more elastic suggesting a higher concentration of elastin fibres [8, 13]. Anatomical and microstructural parameters of those four layers were already studied with classical 2D histology, mechanical testing and second harmonic generation microscopy (Table.2.1, Fig.2.4.b) [7, 8]. The outer layer of the leaflet on the ventricular and atrial side is the endocardium composed of a layer

of endocardial cells. On the ventricular side, those are plumped while on the atrial side they are flattened [13] .

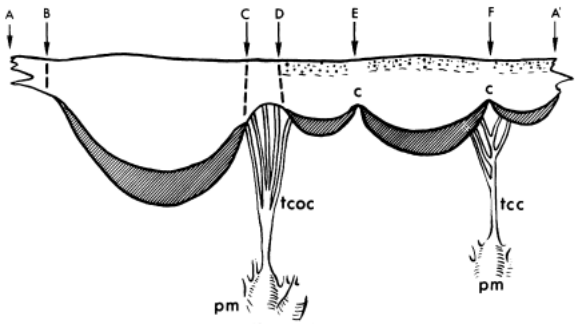

Figure 2.3: Anatomical overview of the MV leaflets. Diagram of a typical mitral valve. The space between B and C is the anterior leaflet, and between D and A' posterior leaflet; c = cleft; pm = papillary muscle.3 zones are described in the leaflets, the basal zone (dotted area), the rough zone (cross-hatched), and the clear zones (blank in between) (adapted from [6]).

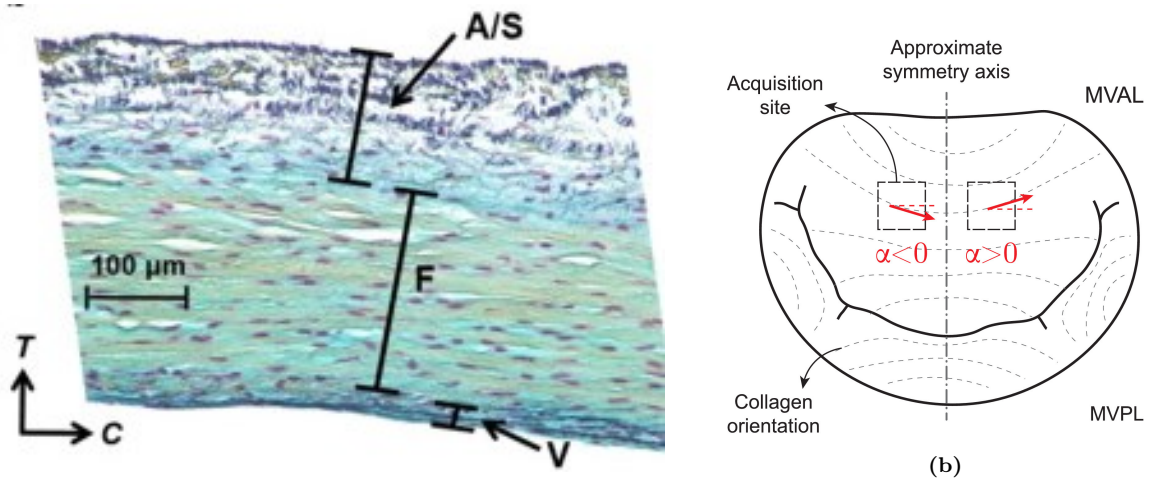

(a) (b)

Figure 2.4: Microstructural overview of the MV leaflets. (a) Four leaflet layers. A is the atrialis, S, is the spongiosa, F, is the fibrosa, and V, is the ventricularis (adapted from [7]). (b) Collagen fibres orientation (adapted from [8]).

Table 2.1: Micromorphometrical parameters of the leaflet four layers (adapted from [8]).

	Atrialis	Spongiosa	Fibrosa	Ventricularis
Thickness(μm)	43.2	41.5	319.6	17.3
Collagen mass fraction	0.231	0.203	0.671	0.309
Elastin mass fraction	0.601	0.198	0.088	0.555

2.2.3 Papillary muscle

Among the papillary muscles (PM), two groups can be distinguished, the anterolateral and posteromedial respectively located below the anterior and posterior commissures (Fig.2.2.d-f). PMs arise from the middle third of the left ventricular wall [27]. At their extremity, both PMs are connected to the anterior and posterior leaflets [24] through the chordae tendineae. The PM contraction cycle can be divided into five steps (Fig.2.5).

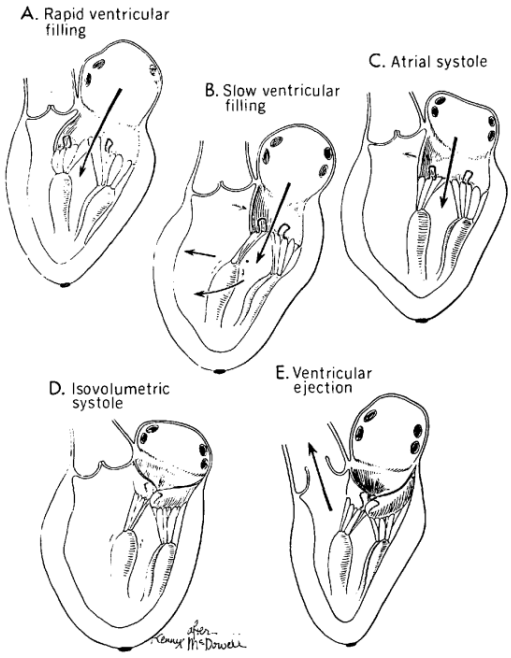

Figure 2.5: PM and chordae tendineae functioning. (A) The heart muscle relaxes. The pressure in the atrium is higher than in the ventricle, the blood flows from the atrium to the ventricle. The MV is open, and the PM and chordae tendineae are loose. (B) Leaflets are not fully opened. (C) Atrial contraction, blood flows from the atrium to the ventricle. The MV is open and the PM and chordae tendineae are tense. (D) Ventricular contraction, leaflets are closed due to the severe pressure change. PMs and chordae are tensed in order to prevent prolapse of the leaflet and regurgitation. (E) The opening of the aortic valve by pressure gradient allows the blood to flow from the ventricle to the aorta. The PMs and chordae are still tense. (adapted from[9])

In summary, the chordae tendineae and PMs can either pull on the leaflets to open or prevent them from moving upwards in the atrium.

2.2.4 Chordae tendineae

Chordae tendineae are fibrous chordae arising from the PM to both leaflets of the MV (Fig.2.2.d-f). They have a significant mechanical role in the opening/closing mechanism of the MV since in a healthy MV, they play a force transmission role from the PM to the leaflet. A malfunction of the chordae tendineae such as a rupture can thus result in non-efficient closing of the MV resulting in regurgitation, i.e., blood going counterflow from the ventricle to the atrium.

In biology, its common knowledge that the structure follows the function [28], understanding the microstructure of the chordae is thus essential to better understand their functioning. It can also help to understand malfunctions and diseases related to the chordae at the microstructural level and *in fine* improve the treatment of such defects. Therefore, this study aims to characterize the chordae tendineae microstructure.

The following sections will investigate and highlight the current knowledge and remaining questions about the chordae micro- and macrostructure.

2.2.4.1 Anatomy of the chordae tendineae

The same MV contains plenty of chordae tendineae and if their general aim is to allow the good opening and closing of the MV, every chordae has a more specific function leading to a specific microstructure and shape. To distinguish the chordae, different nomenclatures have been defined according to parameters: the origin, the insertion site into the leaflet, the structure, and the branching pattern. The nomenclature used in this work and in a lot of previous studies is a simplified one that relies only on the insertion site [5, 6, 29]. It divides the chordae into 3 types (Fig.2.6.a):

- The primary or first order chordae tendineae inserting into the marginal zone of the leaflet and preventing prolapse of the coaptation zone.
- The secondary or second-order chordae insert in the rough zone of the leaflet and prevent excess tension into the leaflet.
- The tertiary or third-order chordae tendineae are only observed in the posterior leaflet and attach the annulus and the base of the leaflet to the PM.

A particular type of secondary chordae; named "strut chordae", is also described. Those chordae tendineae arise from the top of the PMs and differentiate from the others by their thickness and the important mechanical role they play (Fig.2.6.b) [6, 14]. It is worth noting that a fourth type of chordae has also been described; named "false chordae", that bound PM to each other or PM to the ventricular wall [6, 29].

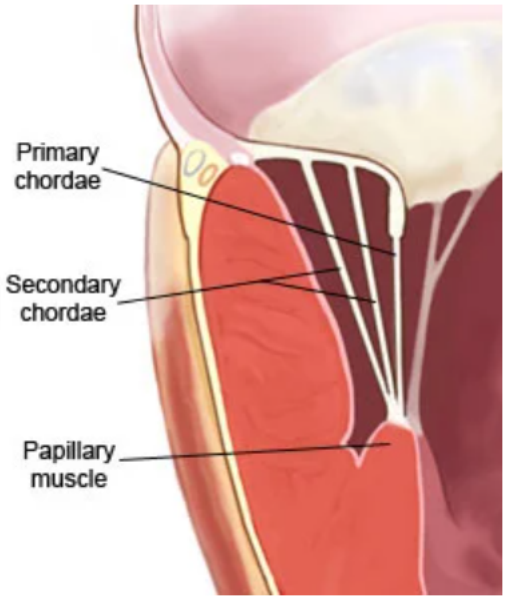

(a)

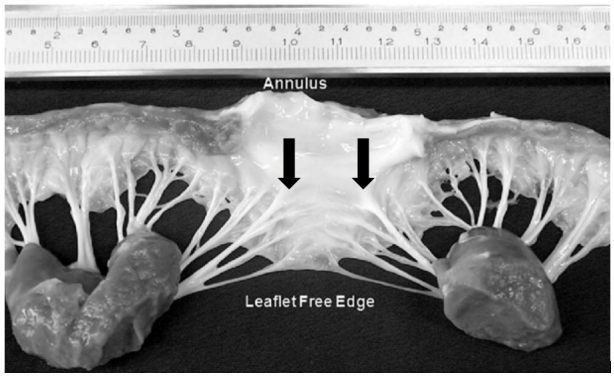

(b)

Figure 2.6: Different subset of chordae. (a) Primary chordae are inserted in the free margin of the leaflet. Secondary chordae are attached on the rough zone of the leaflet (adapted from [5]). (b) 2 anterior strut chordae (black arrows)(adapted from [10]).

2.2.4.2 Microstructure of the chordae tendineae

To prevent any misunderstanding, having a proper definition of terms used in the following sections is essential.

The microstructure is at the microscale and refers to the internal structure of the tissue. It refers to the different micromorphometric parameters of the components of a tissue.

The anatomy is at the meso/macroscale and refers to the shape and geometry of the tissue from the exterior.

2.2.4.2.1 General microstructure

Chordae tendineae connect the PM to the leaflets and are thus referred to as connective tissue. This type of tissue has mainly three components: the cells providing the metabolic properties, a network of interweaving fibres providing the mechanical properties, and the ground substance that allows the plasticity of the tissue [30]. In the chordae tendineae, there are two types of fibres, collagen fibres, and elastin fibres. The first ones are made of collagen I and III and their diameter varies from 0.2 and 12 μm [31]. The collagen fibres present in chordae tendineae have heterogeneous micromorphometric parameters (Fig.2.7). In the core, fibres are

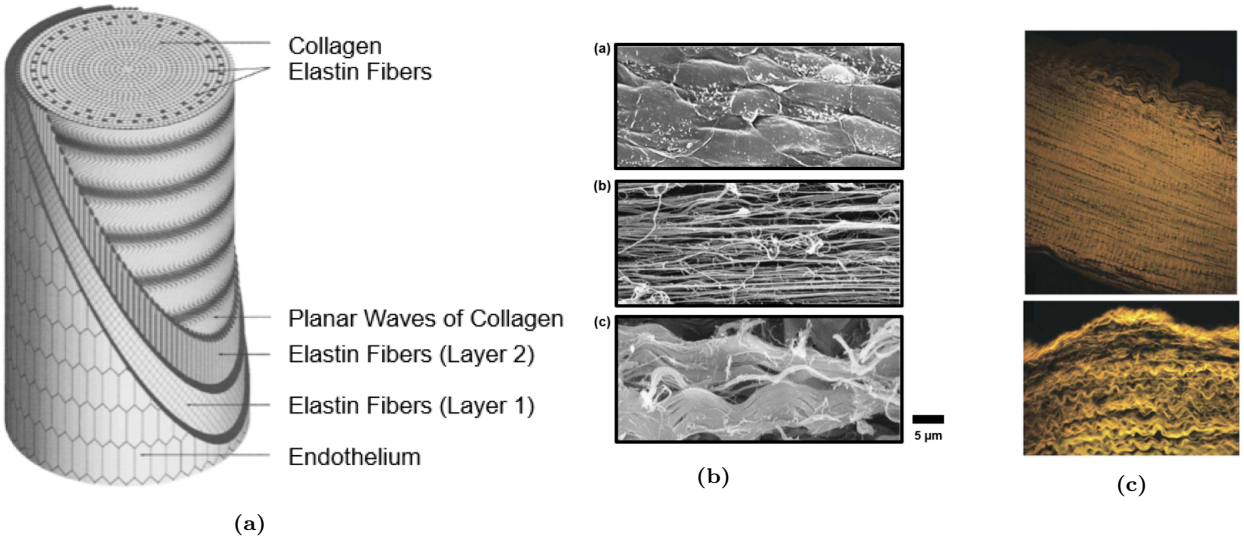

Figure 2.7: Overview of the chordae tendineae microstructure. (a) Schematic representation of a chordae tendineae and its different layers. (b) SEM images of the mitral valve, from top to bottom, a layer of endothelial cells, elastin fibres, and crimped collagen fibres (adapted from [11]). (c) Crimping direction of the collagen fibres (adapted from [12]).

dense and straight while around it, they are more spaced and crimped with more elastin fibres. Chordae tendineae are thus composed of a core surrounded by elastin sheaths. The collagen fibres are crimped in the direction of the load and straightened when elongated. They provide the mechanical integrity of the tissue. The elastic fibres are made of elastin, and their diameter ranges from 0.2 and 1.5 μm [31]. They allow the tissue to be resilient to deformation, which is crucial for the chordae to withstand cyclic stresses. They give elastic properties to the chordae by returning the collagen fibres to their wavy shape after stress release [26]. In the chordae, the ground substance is mainly composed of glycosaminoglycans (GAGs) which are unbranched hetero-polysaccharides [31]. GAGs have three essential properties for connective tissues. First, they are negatively charged which causes a high inflow of water into the extracellular matrix (ECM) composed

of the ground substance and the fibres. The water sucked in provokes swelling of the ECM enabling the tissue to withstand compression. Moreover, GAGs are long sugar chains that cannot fold up resulting in a high stiffness. They are also highly hydrophilic which enables them to form with water a sponge-like structure described as a hydrated gel having a large volume-to-mass ratio, a high viscosity, and a low compressibility. Besides providing compliance to the chordae tendineae, this hydrated gel structure allows the diffusion of molecules necessary to the cell nutrition and plays the role of lubricant and binder between the collagen and elastin fibres [30, 31, 32]. Finally, the most represented cells are the fibroblasts that produce the collagen fibres [30].

While being accurate for the major part of the chordae, the microstructure described above cannot be applied to their insertion sites.

2.2.4.2.2 Chordae insertion into the leaflets

The transition zone between the leaflet and the chordae is the region where the chordae merge into it. Previous studies exhibit results showing variations in the orientation of the fibres forming the chordae. Indeed, at the insertion site into the leaflet, the collagen fibres are aligned with the longitudinal direction of the chordae. Then, their orientation progressively changes to correspond to the direction of the collagen fibres in the fibrosa layer of the leaflet (Fig.2.8.a-b).

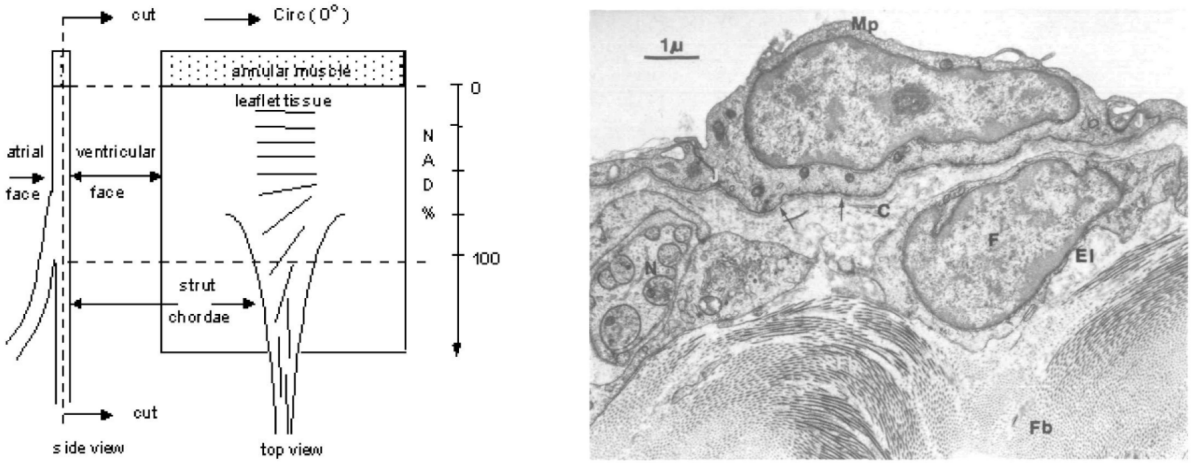

(a) (b)

Figure 2.8: Chordae insertion site into the ventricular side of the leaflet.(a) Schematic representation of the collagen fibres at the insertion site distribution. Collagen fibres go from vertically aligned to horizontal (adapted from [13]). (b) Electron micrograph of the insertion of the chordae in the leaflet. Fb represents the fibrosa extending from the chordae core with collagen fibres reorienting themselves to merge into the fibrosa of the leaflet. C, the collagen fibres. El, the elastic fibres. F, a fibroblast (adapted from [14]).

2.2.4.2.3 Chordae insertion into the PM

The transition zone between the PM and the chordae has been previously described as abrupt (Fig.2.9) [33]. Surprisingly, collagen fibres do not insert deep in the papillary muscles, which might represent a risk since tremendous tension is applied on chordae and a deeper insertion would lead to a better anchorage. The anchorage of the collagen fibre into the myofibres of the PMs is mainly due to a microfibril network [33, 34]. This network bounds the collagen fibres end to the basal lamina of the muscle by enmeshing [13].

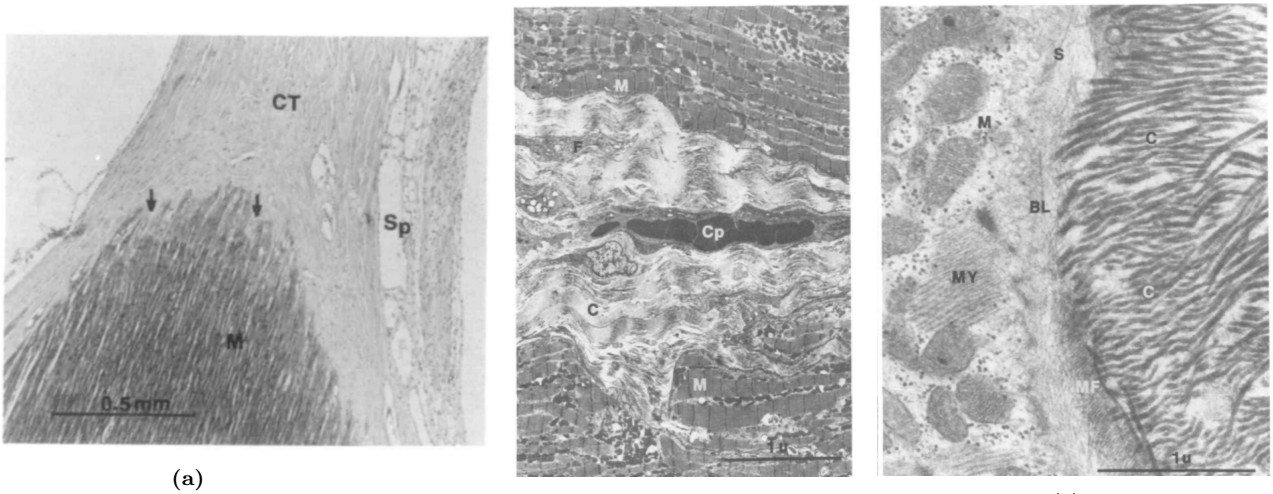

(a) (b) (c)

Figure 2.9: Chordae insertion site into the PM. (a) Longitudinal section with the chordae tissue (CT) and the papillary muscle (M). The arrows represent the penetration of the fibrous tissue of the chordae into the muscle. (b) Chordae collagen fibres digging into the PM. Collagen fibres lose their packed structure while digging into the PM. (Cp) small capillaries, (F) fibroblast, (c) Basal lamina, (BL) with microfibrils. In the end, the collagen fibres (C) are bound to microfibrils (MF) of the basal lamina (adapted from [13]).

2.2.4.2.4 Chordae insertion into the heart wall

Finally, certain chordae are referred to as "false" chordae and do not join a PM to a leaflet but a PM to another or to the ventricular wall. No data is available to describe the microstructure of such chordae at the insertion site [35].

2.2.4.2.5 Blood vessels

Until recently, chordae tendineae were considered as an avascular tissue [36]. In tendinous tissues, the feed of nutrients mainly diffuses from the synovial sheath and no vascularization is needed [37]. However, no synovial sheath is described in the chordae. They also differ from tendons by being made of a single fascicle [38], i.e., collagen bundle. The presence of blood vessels running in the chordae raises some questions. The first is the origin of those vessels, indeed, previous studies reported that they originate from an inflammation reaction while others stated they were normally present in the chordae tendineae. Their importance is also debatable, the insertion and origin of those vessels were not much studied. Those vessels can originate from the leaflet and feed the PM but they can also go from the PM to the leaflet [12]. No study was conducted

to evaluate the degree of penetration of those vessels in the leaflet in order to evaluate the importance of the blood feed provided by the chordae. Quantitative studies were conducted in order to evaluate the proportion of chordae having blood vessels depending on their type and the number of them. While every chordae type contains blood vessels, the strut chordae are the ones having the most of them [12]. The shape of those blood vessels was not extensively studied but their location between the core and the elastin layers of the chordae was reported (Fig.2.10.b).

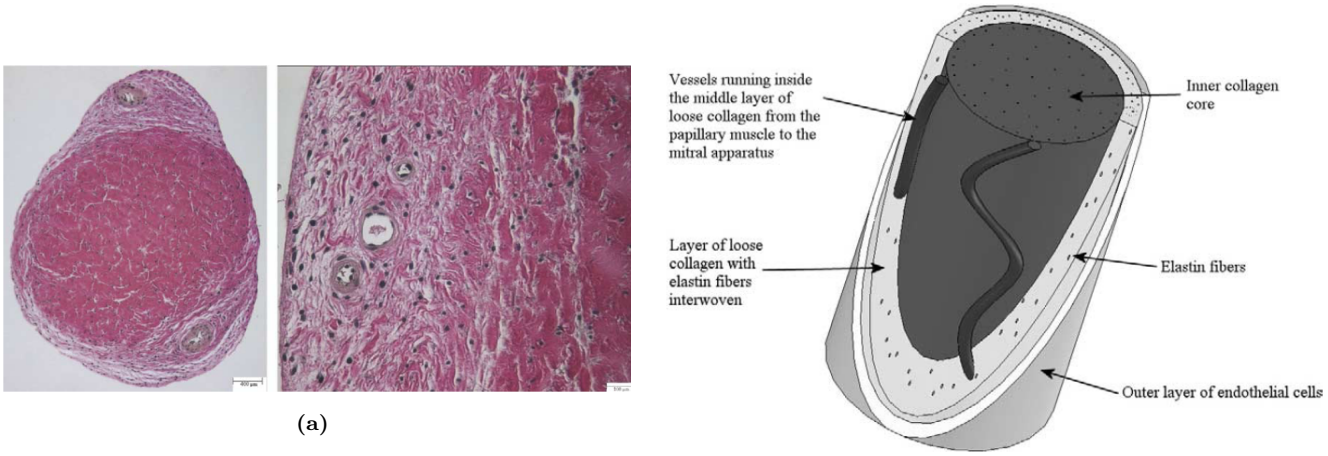

(a) (b)

Figure 2.10: Blood vessel in the chordae tendineae. (a) Classical 2D histological section of a chordae tendineae with white dots that are the blood vessels. (b) The wavy shape of the blood vessel in the chordae is based on classical 2D histology (adapted from [12]).

Unlike the chordae geometry, blood vessels follow a wavy path, as observed in 2D studies (Fig.2.10.b). Indeed, classical 2D histology was performed and chordae were cut radially (Fig.2.10.a), those radial sections exhibited longitudinal and radial cuts of blood vessels [12]. This supports the wavy shape of the blood vessels.

2.2.4.3 Microstructural variations impact on the mechanical properties

Chordae tendineae undergo cyclic stresses during the cardiac cycle. Changes in shape and microstructure occur according to those stresses. Mechanical studies were performed to characterize the mechanical properties of the chordae [10, 39]. The mechanical properties vary depending on the type and size of the chordae [28]. For the same type, thicker chordae are more extensible and have lower Young's moduli. This is linked to microstructural differences. Indeed, thicker chordae have highly crimped collagen fibres, which explains their greater extensibility. The moduli difference is explained by the "fibril-to-fibril" interactions. If the chordae is composed of fibrils with a small diameter, they have more interactions and the chordae moduli are larger [28]. These differences prove that depending on their function, chordae have a different microstructure.

2.2.4.4 Microstructural variations between chordal types

The classification of the chordae is based on diverse criteria and highlights their different functions, shapes, and locations. As structure follows the function, it is also expected to have variable microstructure among the chordae [28]. Previous studies show qualitatively that even if a global structure composed of a compact

collagen core surrounded by elastin layers can be observed in a majority of the chordae, the size and shape of those structures vary a lot from one type to another (Fig.2.11). The microstructural variation between chordae types was also quantitatively studied. J.Liao *et al.* notably described with classical 2D histology that marginal or first-order chordae have on average thinner fibrils and more fibrils per unit area [28]. Other 2D studies reported that elastic fibres are larger in the anterior chordae than in the posterior [40].
While data are available regarding the microstructural variation depending on their type or size, they are only averaged data and some of them contradict each other [28].

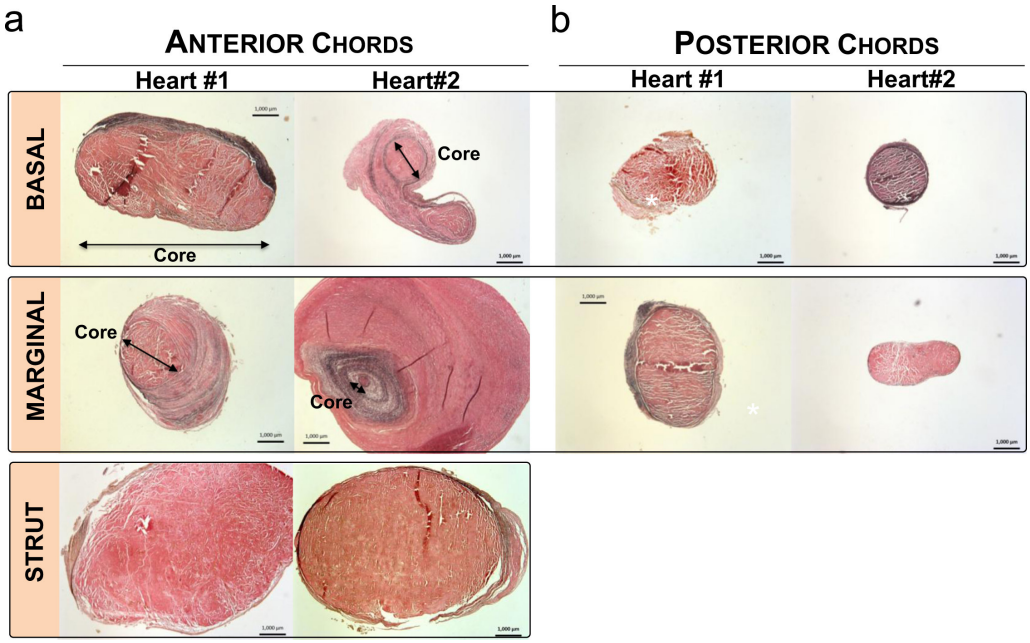

Figure 2.11: Sections of chordae from different chordal types. While the global structure with core and elastin layers can be seen, the shape and size of those regions vary between chordae types. The microstructure varies particularly in the posterior basal chordae referred to as second order and in the marginal or second order chordae with unorganized collagen fibres or separated core and elastin layers. (adapted from [15]).

2.2.4.5 Microstructural variations between species

Not only the function has an influence on the microstructure of the chordae tendineae but species and functioning of the entire cardiovascular system will influence it. Many studies of the chordae tendineae were not conducted on human samples and the result presented in previous sections are often animal samples from different species. Since chordae tendineae are very variable structures, it is interesting to evaluate if the findings in one species can be applied to others. The variation of the number of chordae and microstructure were compared between sheep and cows and resulted in no statistically significant morphological differences [34]. However, another study of the chordae was conducted and showed anatomical differences between humans, ovine and bovine tissue. Indeed, A. Degandt *et al.* reported that in ovine and bovine hearts, posterior strut chordae are shorter than in the anterior while they have the same size in the human (the explanation proposed for the such anatomical difference is that humans are bipedal) [41]. In conclusion, since working on human tissue is ethically more complicated, many studies of the chordae are conducted on animal samples. While the differences between animal and human chordae are currently considered not significant,

only anatomical studies and a few 2D comparisons of the microstructure are available to prove it. Moreover, some studies show contrary conclusions. No 3D comparison of the microstructure was conducted and the presence of vasculature was not studied either. A comparative study of the 3D microstructure of the chordae between different species and humans would thus be highly beneficial to assess the relevance of animal results regarding human applications.

2.2.4.6 Microstructural variations between healthy and diseased chordae tendineae

The proper functioning of the MV ensures correct blood flow in the heart and by extension to the whole body. Chordae tendineae ensure the correct closing of the MV and are thus an essential component of the MV apparatus. However, they are often subjected to defects inducing a loss of their mechanical properties or their rupture. The main causes of such defects are degeneration and rheumatic disease. 24.8% of the chordae rupture are due to rheumatic disease and 11.7% to degeneration [42]. The rheumatic disease consists in the deposition of calcium aggregates in the MV that makes the chordae and the MV, in general, more rigid, while the degeneration involves a change in the microstructure of the collagen fibres in the core that goes from dense to loose [42, 43]. Two types of degeneration are described: Barlow's disease (BD) and fibroelastic deficiency (FED), both as an impact on the leaflet and chordae anatomy and microstructure (Fig.2.13). The first one has a chronicle evolution and induces the thickening of the MV tissue, also called myxomatous degeneration, and the second induces a decrease in the elastic response and thinner valve. This second type of degeneration is observed in ageing people. Regarding the microstructure, myxomatous chordae were reported to have 62% more GAGs than normal [16, 44]. The proportion of the different types of collagen also varies with an increase of 10% of collagen III. An increase in the fragmentation of the elastic fibres is also observed [16] along with an increase in cell proliferation [17]. Some assume that the high increase in GAGs can influence the nature of the chordae tendineae tissue and is the cause of the chordae lengthening or rupture [45] but no 3D qualitative nor quantitative data is available to prove it. Regarding the FED, an increase in GAGs in the spongiosa and fragmented elastin fibres in the fibrosa are also observed [17]. Previously, those two types of degenerative diseases were considered as two different stages of the same one since they have relatively the same consequences but they are in fact completely different diseases (Fig.2.13) [17]. While a 2D qualitative assessment of degenerative chordae microstructure is available (Fig.2.12), no comparison between BD and FED effects on the chordae is available. Only classical 2D histology differences are qualitatively described in the leaflet (Fig.2.13.b). This lack of knowledge regarding the microstructure of the chordae can be transposed to other diseases such as rheumatic disease.

2.2.5 Treatment of the MV and the chordae tendineae

While degenerative and rheumatic diseases affect the whole MV apparatus, important malfunction can be the result of chordal elongation or rupture. In fact, one out of five patients suffering from important MV malfunctioning arise from a chordal deficiency [46, 18].

While MV replacement is a standard method used for MV deficiency, MV repair is preferable because it in-

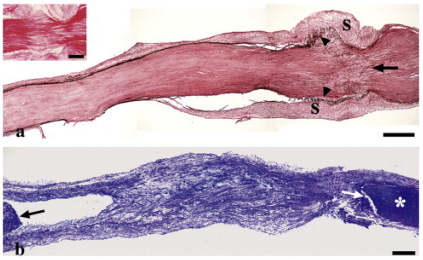

(a)

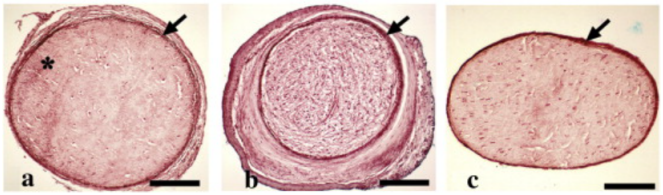

(b)

Figure 2.12: Classical 2D histological section of degenerative chordae. (a) In the above picture, S represents the elastin-rich regions separating from the chorda. Arrows show elastin accumulation. Below, the asterisk represents the rupture of the core, the black arrow shows the core that is retracting. It also shows the disorganization of the microstructure (scale: a, 250 [μm]; inset of a, 250 [μm]; b, 100 [μm]). (b) a and b are degenerative chordae, and c is healthy. The delimitation between the core and the elastin sheath is the darker circle shown with a black arrow. a and b exhibit multilayered and partially detached layers while c does not (scale = 100 [μm]) (adapted from [16]).

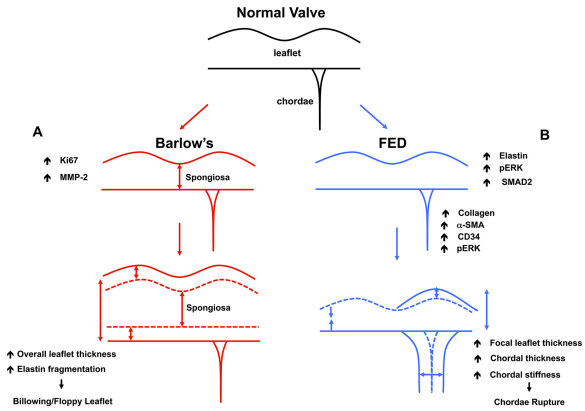

(a)

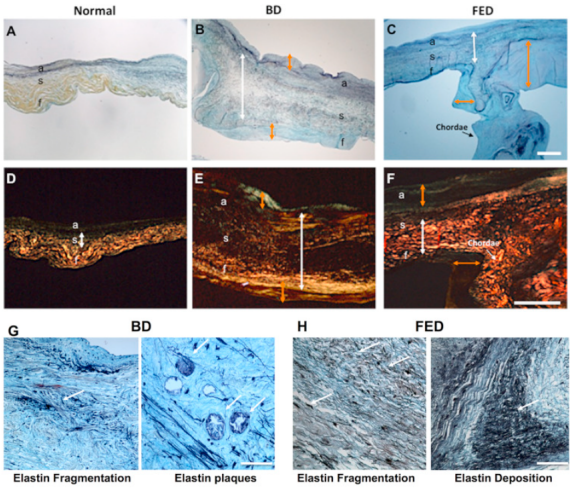

(b)

Figure 2.13: BD and FDE anatomical and microstructural consequences in the leaflet. (a) Anatomical differences between BD and FED. (b) In G, there is a formation of elastin plaques induced by BD. In H, there is an elastin deposition due to FED (adapted from [17]).

duces better thromboembolism rates, endocarditis resistance, and durability and does not request a systematic anticoagulation treatment of the patients [47]. New MV repair techniques have thus been investigated and described by P.Fedak *et al.* [47]. A well-known MV repair technique is the replacement of chordae tendineae by polytetrafluoroethylene sutures (PTFE) (Fig.2.14.a). Previously, chordae replacement was done using Teflon or nylon. However, animal studies reported very promising results using PTFE. The PTFE filaments are covered with fibrous tissue and their gross structure is very similar to the native ones (Fig.2.14.b). A human study was conducted and no such results were observed after 9 months, the artificial chordae is not

colonized with native tissue (Fig.2.14.c). Despite that, the insertion site of the artificial chordae into the leaflet and PM is well-healed and covered by native tissue. It can thus be assumed that more time is required for fibrous tissue to cover the PTFE chorda [18].

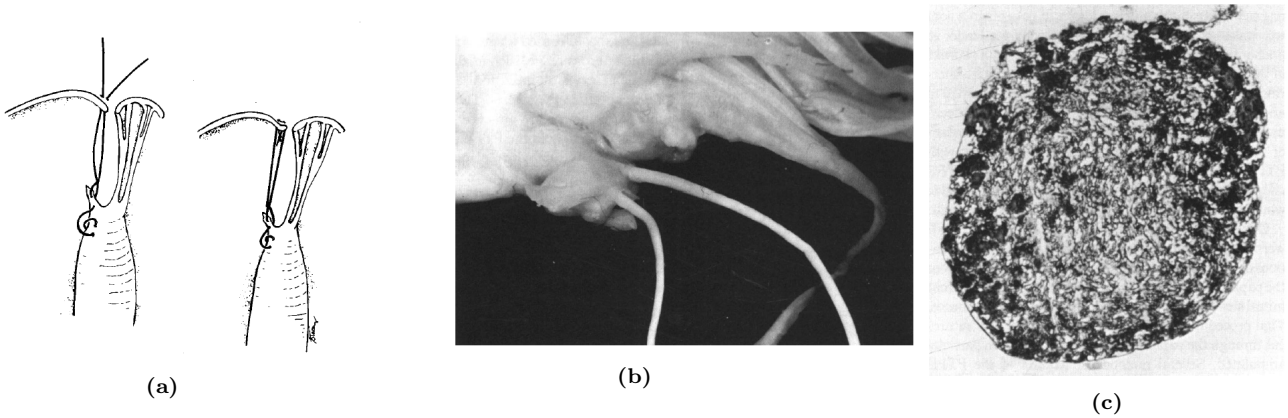

(a) **(b)** **(c)**

Figure 2.14: Chordae repair technique using PTFE.(a) Replacement of a first-order chordae using PTFE suture. (b) 2 PTFE and 1 native chordae after 9 months covered by fibrous tissue (c) Histological section of a PTFE chordae after 9 months with no cellular in or out the artificial chordae. months postoperatively.(adapted from [18])

As explained for the PTFE, the microstructure and physical properties of the native tissue are very important criteria to determine the most efficient material for surgical repair. A material that mimics and blends in the native tissue must be sought.

2.2.6 Computational modeling

"Computational modelling is the use of mathematics, statistics, physics, and computer science to study the mechanism and behaviour of complex systems by computer simulation. A computational model contains numerous variables that characterize the system being studied. Simulation is done by adjusting these variables and observing how the changes affect the outcomes predicted by the model [48]."

It allows for performing a large number of experiments by simulation resolving problems much faster, easier and cheaper. In the case of the chordae tendineae and biological tissue in general, it could help understand the disease's causes and consequences and assess the efficiency of a given treatment addressing a specific dysfunction [49].

The finest way of modelling a biological tissue is multiscale modelling which *"uses mathematics and computation to quantitatively represent and simulate a system at more than one scale while functionally linking the mathematical models across these scales. Biological and behavioural scales include atomic, molecular, molecular complexes, sub-cellular, cellular, multi-cell systems, tissue, organ, multi-organ systems, organism/individual, group, organization, market, environment, and populations [48]."*

Being able to accurately describe a biological tissue in such a way is useful, but extensive data at different scales must be available. Previous studies provide some insight on that matter by trying to model the chordae [48]. Khalighi *et al.* describe the topology and geometry of the chordae tendineae using 3D images derived from high-resolution µCT. The result was that the ovine MV chordae could be represented with a

full binary tree model. They also found that in an individual MV, the number of chordae tendineae could be topologically approximate with 12 chordae. Each of them having five insertion sites [50].
In the following study, Khalighi *et al.* developed computational models using *in vivo* imaging and the result was that *in vivo* data was not relevant to model the complex geometrical structure of the chordae tendineae with such fidelity that it could be used for *in silico* studies [51].
Mechanical properties of healthy tissue are available [40]. Regarding diseased tissue, A. Siefert *et al.* worked on providing data set using mechanical testing to simulate ischemic mitral regurgitation and undersized mitral annuloplasty with computational model [49].
The microstructural characterization for modelling purposes was successfully performed by Khalighi *et al.* using small angle light scattering technique [51]. While this method is relevant for such study, A. Maes *et al.* described that this method also called phase-contrast µCT is very time-consuming and often requires dehydration of the sample that could lead to a deformation of the native tissue [20].
In conclusion, providing a computational multiscale model of the chordae tendineae requires lots of data regarding the gross anatomy, geometry, and topology which is currently available. It also requires mechanical properties of the different chordae at a large scale which is also available [40]. However, providing a multiscale model requires a large set of quantitative data concerning the microstructure of the chordae which is currently not available. This lack of data prevents the establishment of an accurate model for the chordae tendineae.

2.3 Imaging technique for chordae tendineae

2.3.1 *In vivo* imaging

In vivo imaging of the cardiovascular apparatus has many applications such as diagnosing heart conditions, assessing the structure of the heart, monitoring the blood flow and diseases or treatment progress [52]. *In vivo* imaging is thus used to assess the anatomy or the functioning of the vascular apparatus [19]. Most used *in vivo* techniques are the echocardiogram, X-ray computed tomography (CT), nuclear imaging and magnetic resonance imaging (MRI) [19, 52, 53].
An echocardiogram is an ultrasound imaging technique that provides real-time and functional imaging. The maximum spatial resolution in small animals is in the range of 30 - 60 μm. Nuclear imaging refers to mainly two imaging techniques known as positron emission tomography (PET) and single-photon emission computed tomography (SPECT). They are functional imaging techniques relying on β^+ and γ radiation emitted by the biological sample observed. Their maximum spatial resolutions are respectively 0.7 mm and 0.25 mm. CT is an ionizing structural imaging technique relying on X-ray attenuation in the biological sample observed. It has a high spatial resolution (100 μm) but poor soft tissue contrast. Finally, MRI is a non-ionizing radiation-based imaging technique relying on electromagnetic waves that enable high spatial resolution (100 μm) with high soft tissue contrast [19, 52, 53].
Echocardiograms were used to recognize ruptured chordae tendineae [54, 55]. A special type of echocardiogram called transoesophageal echocardiography (TEE) was used to assess the length of the chordae tendineae

[56]. MRI applied to the vascular apparatus and referred to as cardiac magnetic resonance imagery (CMR) was used to describe the gross anatomy of the chordae [57] and detect anomalies in the subvalvular apparatus [58]. CT applications are for example planning transcatheter mitral valve replacement (TMVR) [59].
While *in vivo* imaging has many clinical applications, due to their poor resolution and contrast, they are not relevant to study the microstructure of the chordae tendineae.

2.3.2 2D histology

2D histology is the gold standard to describe the microstructure of soft tissues. Chordae tendineae are no exception. Different 2D histology techniques can be described namely, classical 2D histology, immunohistology, and scanning electron microscopy (SEM).
For classical 2D histology, preparation of the sample is needed and consists of different steps (fixation, embedding, and cutting) [19]. Chordae tendineae samples are first fixed in PBS. Then, dehydrated using ethanol and embedded in paraffin. After that, it is cut into a few micrometres (5 μm) thin slices [19, 60, 61]. These slices are then stained using various staining agents depending on the structure of interest [60]. Classical histology relies on light or polarized light microscopy. Staining agents are used to improve contrast and pinpoint the structure of interest using both techniques. Staining agents described in the literature are Movat's pentachrome, picrosirius red staining [60, 61], hematoxylin and eosin (HE) and Verhoeff's pentachrome [61].
Immunohistology uses antibodies that selectively bound to antigens in biological tissues. Similarly to classical 2D histology, it involves different preparation steps. First, the tissue is fixed, embedded, and cut into slices. Then, the slices are deparafinatted, the antibody is incubated, the reaction between the antigen and the antibody is labelled and finally, the slices are counterstained [62].
SEM can give information about the fine structures of the chordae tendineae. However, it also requires sample preparation with a fixation step in glutaraldehyde 2.5 % for example, after that it is dehydrated and finally it is sputtered with a metal, e.g., gold [60].
Currently, classical 2D histology is widely used to describe the microstructure of soft tissues because of its high discriminating power, its low resolution (around 0.25 μm [19]) and the extensive knowledge about the technique and stains used [20, 63]. In addition, many 2D slices of biological samples allow a 3D qualitative reconstruction of the whole tissue. The microstructure of the chordae tendineae described above was mainly studied using *ex vivo* 2D histological analysis [11, 13, 14, 26, 31, 34, 64]. Different micromorphometric parameters such as the average diameter of the fibril or their concentration along the chordae were also studied using 2D histology [65]. Qualitative results regarding the 3D microstructure of the chordae are mainly based on 2D histology performing multiple sections on the same chorda and interpolating the 3D microstructure [13]. SEM has been used to describe the insertion site of the chordae but does not allow the study of the microstructure, only a 3D qualitative results of the surface of the chordae at the insertion site [33]. 2D *ex vivo* histology also allowed to characterize microstructural variations between chordae types [5, 12, 15, 28, 36, 37, 40].
However, this method has limitations. First, cutting the sample into slices can be referred to as destructive

since it affects the native structure of the tissue observed. It is also limited to a single section orientation [20, 63]. The fixation and embedding steps also alter the microstructure of the sample observed [19].

2.3.3 X-ray based 3D histology

An *ex vivo* non-destructive 3D standard imaging technique is the µCT, i.e., microfocus X-ray computed tomography [19, 20, 63]. This method is based on the attenuation of X-ray passing through the sample. During a µCT acquisition, the sample is rotated along one axis and is submitted to an X-ray beam allowing the allocation of an attenuation value to every point of the tissue. More precisely, the tissue is virtually divided into voxels which is an analogous version of a pixel in 3D, and to every voxel, an attenuation value is allocated. While this method is very efficient to study medical devices like stents or mineralized tissue such as heart valve calcifications, it is inherently limited by the attenuation capacity of soft biological tissue. Indeed, due to their low X-ray attenuation, µCT cannot allow any discrimination between soft tissues constituents, e.g., collagen and elastin fibres [19, 20, 66].

Fortunately, a specific type of µCT referred to as CECT, i.e., contrast-enhanced computed tomography, allows the study of soft tissues using CESAs, i.e., X-ray contrast-enhancing staining agents. The tissue sample is immersed into a solution made of diluted CESA that diffuses into the soft tissues allowing discrimination by enhancing their X-ray attenuation [20]. While CECT is thus highly dependent on the CESA chosen, little is actually known about their interaction and effect on the observed tissue. During the last decade, different CESAs were proposed, each of them having different affinities and limitations [19]. The most used CESAs reported for the study of soft tissues are Lugol's iodine, osmium tetroxide and polyoxometalates (POMs) [19, 20]. While those CESAs enable the observation of soft tissues, they are known to significantly alter the native conformation of the microstructure inducing shrinkage, deformation, dehydration or destruction [19]. To this end, A.Maes *et al.* [20] proposed POM-based CESAs such as Hf-WD 1:2 POM that allow soft tissue staining while inducing less deformation and shrinkage of the microstructure (Fig.2.15) [19].

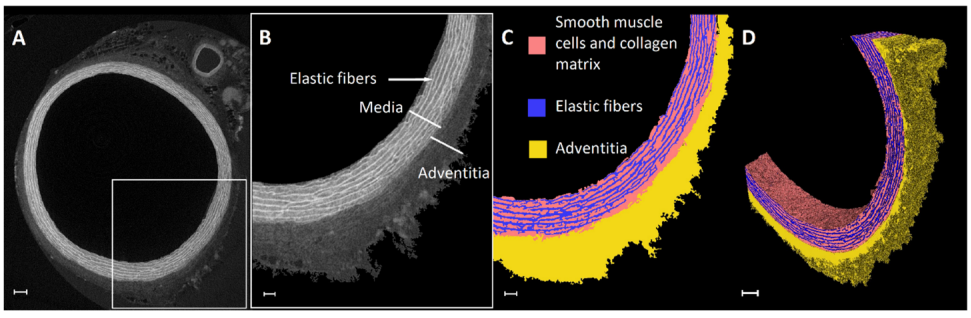

Figure 2.15: CECT of a rat aorta using Hf-WD 1:2 POM. The elastic fibres, collagen matrix, and adventitia are observable. The individual fibres are not visible (adapted from [19]).

While it effectively enables the observation of soft tissue constituents such as elastin and collagen fibres, the post-processing of the 3D images does not allow segmentation of the individual collagen and elastin fibres [20]. This is due to the limited spatial resolution achievable with the CECT [20], i.e., the smallest distance at which different objects can be distinguished as independent. To this end, A. Maes *et al.* proposed a new

technique referred to as cryogenic CECT or cryo-CECT [20]. This method consists in imaging the stained sample with µCT in its frozen state. It allows a high contrast between individual fibres and their surroundings due to the insolubility of the CESA in the crystallized water originating from the tissue (Fig.2.16).

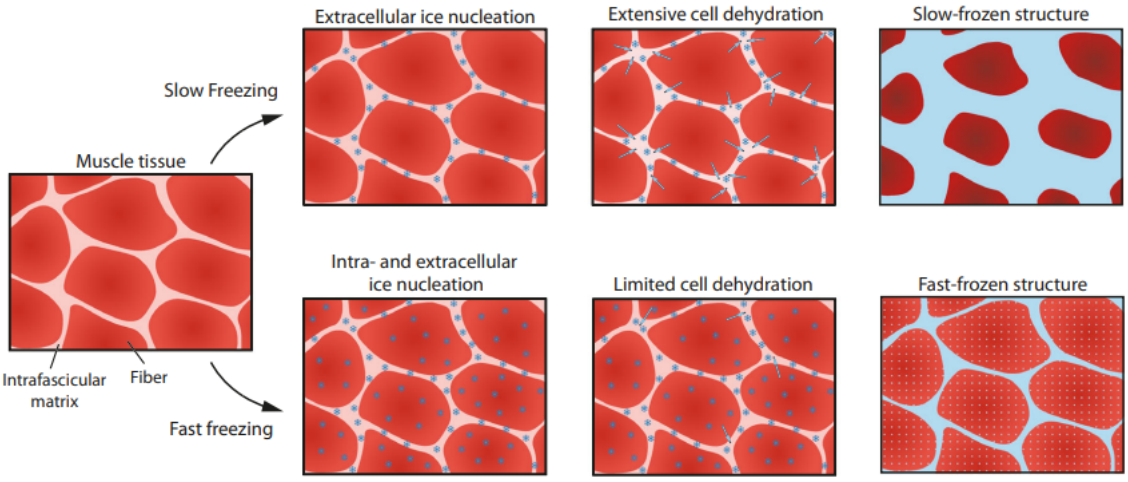

Figure 2.16: Fast vs low freezing rate of muscle tissue. Slow freezing results in the formation of extracellular ice crystal nuclei outside of the muscle fibres while fast freezing leads to the formation of ice crystals inside and outside the muscle fibres. Ice crystals are homogeneously distributed in the tissue (adapted from [20]).

While A. Maes *et al.* were successfully able to segment individual collagen fibres using this method (Fig.2.17), they also showed how inadequate freezing parameters could damage or alter the native microstructure of the observed tissue, e.g., slow freezing at -80°C resulted in the compression of the collagen fibres. Similarly to the CESAs, the freezing parameters are thus dependent on the biological tissue observed [20].

Using this technique for the characterization of the MV and chordae tendineae requires a fine-tuning of those parameters to obtain relevant results. Indeed, cardiac valves are composed of a lot of water which is critical regarding the frozen rate and intensity. To segment individual fibres of the chordae with minimum deformation of the native microstructure, fast freezing of the sample is thus needed.

In conclusion, cryo-CECT as proposed by A. Maes *et al.*, seems a relevant method to perform 3D quantitative analysis of the chordae tendineae microstructure and will be investigated in this study along with classical CECT.

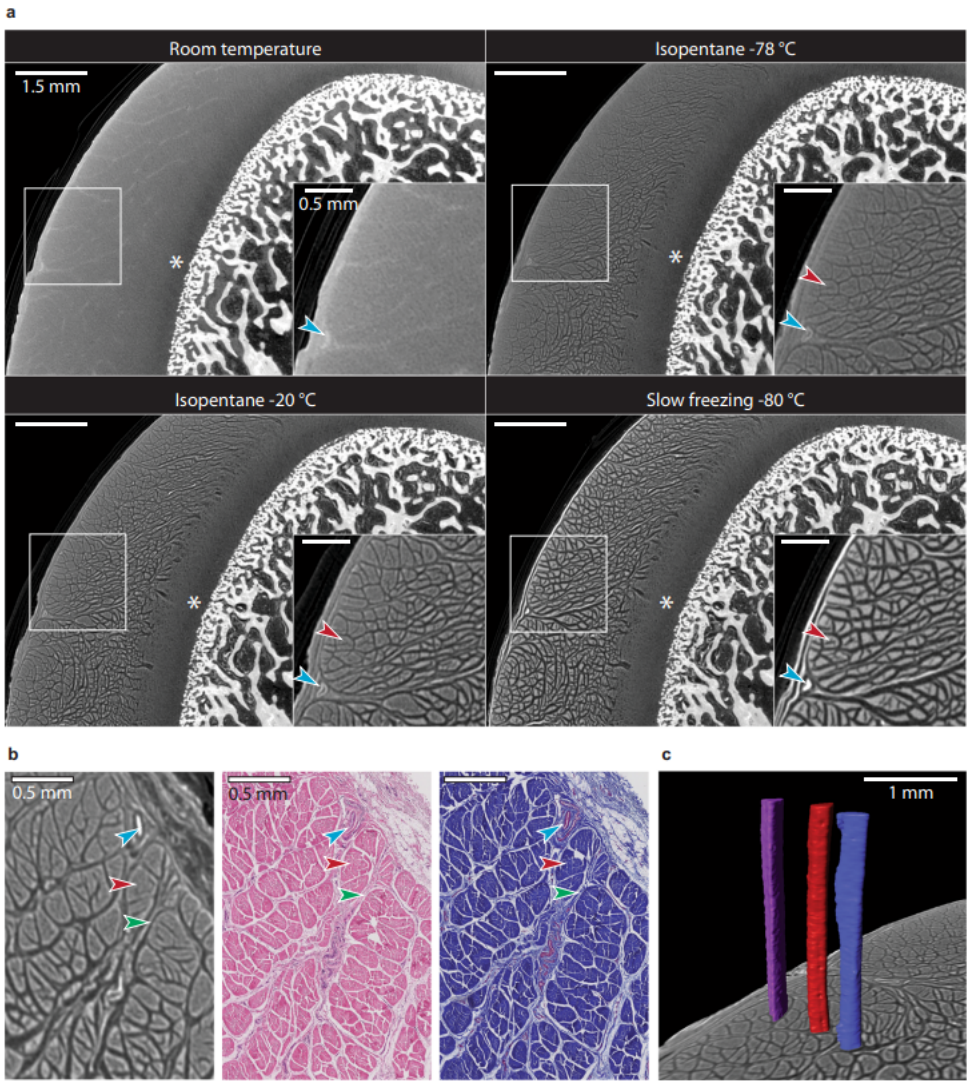

Figure 2.17: Achilles tendon section using CECT and cryo-CECT.(a) Comparison of the resolution using different freezing parameters and stained with Hf-WD 1:2 POM. The Slow freezing at $-80°C$ exhibits high contrast between the fibres. (red arrow) shows an individual collagen fibre and (blue arrow) a blood vessel. (b) Comparison of cryo-CECT result versus classical histology. (c) Individual collagen fibres 3D visualization (adapted from [20]).

3

Problem statement, aim and objectives

Microstructural features of chordae tendineae such as the proportion and arrangement of elastin, collagen, and glycosaminoglycans (GAGs), are crucial for their biomechanical function. Indeed, the structure of these connective tissues depends on their physiological purpose, which is to provide support, flexibility, and resilience to the cardiac valve system. Unravelling the microstructural characteristics of chordae tendineae might therefore bring valuable insights into their functional properties and overall performances.
As seen in the literature, classical 2D histology has helped to identify the main constituents of the chordae tendineae but is limited by its 2D nature and a 3D non-destructive imaging technique to assess the chordae microstructure is still lacking. Hf-WD 1:2 POM-based CECT was already performed on the entire murine heart allowing visualization of the muscle fibres with minimal deformation of the native microstructure. However, visualization of individual collagen and elastin fibres remains challenging. To this end, A. Maes *et al.* presented a new CECT method called cryo-CECT, which consists in imaging the stained tissue in its frozen state. This technique was previously performed on an Achilles tendon and allowed to segment individual collagen fibres. Both CECT and cryo-CECT gave promising results for 3D non-destructive microstructural assessment of soft tissues and more particularly, chordae tendineae which will be investigated in the context of this study.

The aim of this master thesis is to characterize the microstructure of the chordae tendineae with 3D CECT and cryo-CECT, and Hf-WD 1:2 POM as CESA, and to explore the potential applications of those imaging techniques in characterizing the chordae tendineae microstructure.

The aim of this master thesis can be divided into three specific objectives:

- Optimization of the sample preparation for obtaining high-resolution 3D images of the thin and tree-like structures of chordae tendineae.
- Comparison of the effectiveness of CECT and cryo-CECT in characterizing the chordae at various scales for observed (sub)structures.
- Quantitative and qualitative analysis of the chordae (micro)structure and comparison with the literature.

4 Materials and methods

4.1 Sample

The sample used in this study was dissected from a porcine heart obtained from WESTVLEES, a slaughterhouse located in Westrozebeke, Belgium. The heart was dissected with the following procedure. First, a cut was performed through the apex region of the heart allowing to distinguish the left and right ventricles. Then, the apex was excised until the beginning of the papillary muscles of the MV. The right heart and left atrium were excised. Care was taken not to damage any part of the mitral valve apparatus i.e., leaflet, papillary muscles and chordae tendineae. Once the MV apparatus was extracted, a cut was performed into the leaflet between the anterior and posterior leaflet to open the valve, trying to preserve as much as possible the native structure of the MV apparatus. Then, papillary muscles were excised until the insertion of the chordae tendineae. Finally, the sample was dissected from the insertions into the leaflet to the PM. Characterization of the sample anatomy and classification are described in the following section (Section 5.1).

4.2 Sample preparation

4.2.1 Sample fixation and CESA staining

Following dissection, the sample was fixed ($\geq$48h) in 4% formaldehyde (FA) at 4°C, then washed with PBS and stored at 4°C in fresh PBS for 48h. Then, the sample was incubated in 1ml of (1:2) Hafnium substituted Wells-Dawson polyoxometalate (Hf-WD 1:2 POM) solution for 24h on a shaker plate at room temperature. Synthesis of the Hf-WD 1:2 POM was performed as described in the literature [67]. The Hf-WD 1:2 POM staining solution was prepared by dissolving 35 mg/mL of Hf-WD 1:2 POM in PBS, as described by A. Maes *et al.*[20].

4.2.2 Sample mounting and holders

Throughout this study, two sample holders were used. The first sample holder (Fig.4.1) was a standard toothpick made of birchwood. The toothpick base was wrapped in parafilm and then inserted in a hollow cylindrical aluminium holder.

Figure 4.1: Sample holder n°1,the toothpick. On the left the toothpick is inserted in the aluminium holder. The sample corresponds to the darker dot on the toothpick. The parafilm outer layer is also visible.

For the second sample holder, a scalpel was used to refine the upper part of a toothpick by longitudinally scratching it, resulting in a half-circle cross-section. The base of this half toothpick was then wrapped in parafilm and then inserted in a hollow cylindrical aluminium holder as for the second sample holder.
Independently of the sample holder type, the same mounting protocol was followed (Fig.4.1). First, the sample holder was wrapped in a layer of parafilm. Then, the sample was put around it, trying to separate the chordae branches. Finally, a second layer of parafilm was wrapped around both the sample and sample holder. Based on the obtained 2D axial cross-section of the sample mounted with the two different sample holders, the position of the sample on the holder and in the field of view can be assessed. Moreover, the different holder's radii can be evaluated and are of 2 mm and below 1 mm for the toothpick and half toothpick respectively (Fig.4.2).

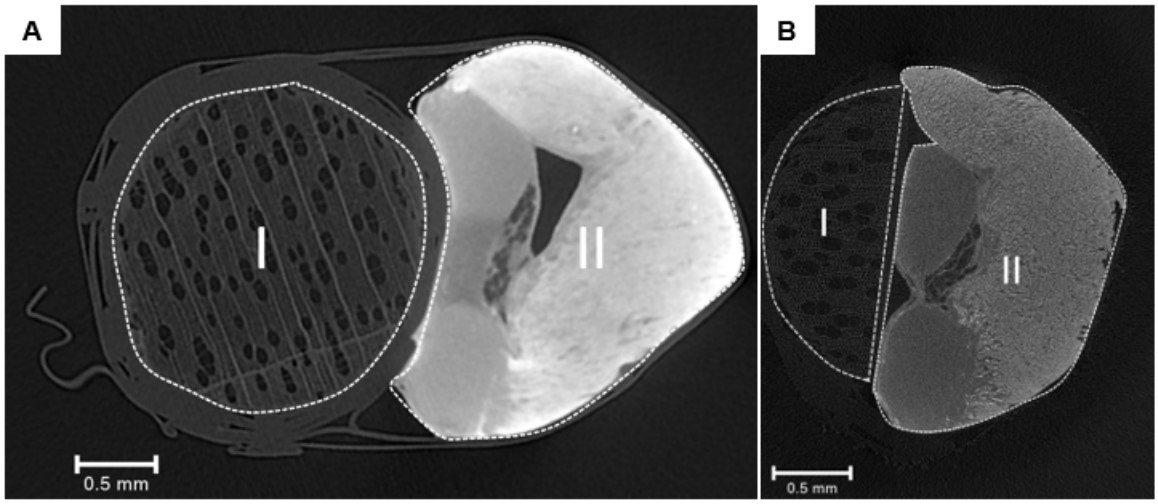

Figure 4.2: Sample holder cross sections (I) and position of the sample (II) in the field of view (FOV). (A) Cross section of the 1st sample holder (toothpick) with a diameter of 2 mm. The sample is not centred in the field of view. (B) Cross section of the 3rd sample holder (half toothpick) with a smaller radius below 1 mm. The sample is in the centre of the FOV.

4.2.3 Freezing protocol

When performing cryo-CECT, the mounted sample was frozen before image acquisition. Two freezing protocols were used. In both cases, the sample was fast frozen during 30s in isopentane, as described in the literature [20]. The first protocol was a fast freezing (FF) at -45°C and the second at -80°C. The isopentane had an initial temperature of -80°C. In the first freezing protocol, the isopentane was therefore allowed to

equilibrate to room temperature under a laboratory fume hood, increasing its temperature from -80°C to -45°C before immersion of the sample to perform fast freezing.

4.3 MicroCT acquisition parameters

All datasets were generated using a Phoenix Nanotom M (Waygate Technicals Baker Hughes). When performing cryo-CECT imaging, the sample was kept frozen using a cryo-stage designed and described by A. Maes *et al.* [20]. It maintained the sample at a temperature of approximately -35°C throughout the imaging process. In this study, different zones of the sample were imaged, the full volume of the sample (i.e. overview), the muscle insertion, which corresponds to the region where the chordae inserts into the muscle, and the leaflet insertion region. Four acquisition protocols were applied to those different regions of interest (Table 4.1).

Table 4.1: MicroCT acquisition parameters

		Overview	Muscle insertion			Leaflet insertion
	Protocol number	1	2	3	4	4
	Imaging protocol	CECT	CECT	Cryo-CECT	Cryo-CECT	Cryo-CECT
Sample preparation	Sample holder	Toothpick	Toothpick	Toothpick	Half-toothpick	Half-toothpick
	Freezing temperature (°C)	NA	NA	-45	-80	-80
Acquisition parameters	Tube voltage (kV)	70	70	70	70	70
	Tube current (µA)	180	220	220	220	220
	Focal spot size (µm)	2.98	0.92	0.92	0.92	0.92
	Voxel size (µm)	6.8	1.4	1.5	1.2	1.2
	Mode	0	1	1	1	1
	Collimator	W	W	W	W	W
	Exposure time (ms)	500	750	1000	1000	1000
	Average	3	3	3	3	3
	Skip	1	1	1	1	1
	Scan duration (min)	65	126	166	360	360
	Number of images	1800	2400	2400	2600	2600

4.4 Reconstruction parameters

After the acquisition, every dataset was reconstructed using the *datos.2x software* (Waygate Technicals Baker Hughes). The reconstruction parameters can be found in Table 4.2. The resulting images were saved as 16-bit slices in the .tiff format and subsequently transformed into 8-bit .BMP format using a custom MatLab tool. This tool was designed in-house and applies histo-windowing techniques to the dynamic range specific to each dataset [68].

Table 4.2: MicroCT reconstruction parameters

Reconstruction parameters	Value
Scan optimizer	ON
Inline median	ON
ROI-CT	ON
Filter volume	ON
Beam hardening correction	7

4.5 Image processing and analysis

Image processing and analysis of all datasets were conducted using the Avizo software (Thermo Fisher Scientific, Bordeaux, France).

4.5.1 Artefact removal

The initial preparation of the raw datasets involved the removal of cross-sectional images at the top and bottom of the sample due to the presence of cone-beam artefacts. The number of removed images was visually assessed based on the presence of artefacts and varied between the different datasets. On average, 200 images were removed at the top and bottom of each dataset.

4.5.2 Segmentation of the sample from the background

For all datasets, segmentation of the sample from the background was performed using the *histogram tool*, and *brush tool* and *lasso tool* conjoined with the *interpolation tool*.

4.5.3 Anatomical features and morphology

In the dataset obtained with low-resolution CECT (protocol n°1), a visual assessment was used to extract a subvolume containing only the chordae. One of the chordae was chosen for further morphological assessment. The curved length was obtained using the *Spatial graph statistics tools* on a *skeletonized* chorda obtained with the *Centerline tree tool* with default parameters and a number of branches set to 1. The aspect ratio and area were also obtained using *Label analysis tool* but with an XY interpretation and *Append* sequence mode. Visualisation of the variation of the aspect ratio and area along the chorda was performed using the *Sieve analysis tool* with a number of values chosen in order to optimize the visualisation of the desired features along the chord. The aspect ratio was calculated as the ratio between the length and width of the chordae 2D sections.

4.5.4 Microstructure

4.5.4.1 Adipocytes

For the qualitative assessment of the location of the adipocytes, fat droplets were grossly segmented using the *Magic wand tool* in the images obtained with low-resolution CECT (protocol n°1). Segmentation of individual fat droplets was conducted on high-resolution CECT (protocol n°2) using the *Magic wand tool*. The *Separate object tool* was then used to separate the droplets. Microstructural analysis was then performed on the individually labelled droplets. Two parameters were assessed using the label analysis tool. The sphericity was implemented in a *Measure group* and expressed as $\psi = \frac{\pi^{\frac{1}{3}} * (6V)^{\frac{2}{3}}}{A}$. In this formula, V represents the volume of the object and A represents the surface area of the object. Both parameters were obtained using the *Label analysis tool*.

4.5.4.2 Muscle, collagen and elastin fibres orientation

In the datasets obtained with high-resolution cryo-CECT (protocol n°4) of the muscle insertion, muscle, collagen and elastin fibres orientation was computed using the *Local orientation tool* on the full volume of the muscle insertion with a window histogram on the same range as of the fibres (130-255) with a block size of 64. The *Local orientation tool* is based on principal component analysis techniques to calculate local orientation information in the 3D image. Specifically, it determines the primary local orientation. The image is first divided into user-defined blocks of a size that is a power of two, which can overlap. Then, the Fourier transform was applied to each block to extract the amplitude. The inertia matrix is computed on each Fourier-transformed block. Since the matrix is symmetric, the Jacobi iterative method can be employed to extract the eigenvalues and eigenvectors. The main fibre orientation is determined by the eigenvector associated with the lowest eigenvalue. The *OrientView* object was then used conjointly with the *Grow tool* of the segmentation editor and *Label analysis* to improve the 3D visibility of the fibres and their orientation.

4.5.4.3 Vessels

To assess the contrast difference between vessels and surrounding tissue using CECT and cryo-CECT, the *Line probe tool* was used on approximately the same vessel visible in the axial section using CECT and cryo-CECT. This vessel was visually identified on approximately the same axial slice obtained with high-resolution CECT (protocol n°2) and cryo-CECT (protocol n°3) Those protocols were chosen because they were performed on the same sample holder and subsequently, which allow for a more accurate vessel identification. Segmentation of the vessels was performed for low-resolution CECT (protocol n°1), high-resolution CECT (protocol n°2) and cryo-CECT(protocol n°4) using the *Magic wand tool* on part of the vessel network. Selection of the grey values was tuned using the *Magic wand tool* to keep as much of the vessel network while only taking blood vessels. This operation was performed on all the identified vessels.
Microstructural assessment of the vessels was performed on two of the segmented vessels located on the opposite side of the muscle and obtained with high-resolution cryo-CECT (protocol n°4). The chosen vessels were automatically divided into segments using the *Centerline tree tool* based on the number of branching

nodes visually assessed. Automatic assessment of the curved length, corresponding to the total Euclidean distance between the branching nodes, was performed for each vessel segment using the *Spatial graph statistics tool*. This same tool was used to automatically assess the mean radius of the vessel which is computed based on the thickness of the vessels at each point and assumes that the blood vessel has a tubular shape.

4.5.4.4 Muscle fibers

Muscle fibres were segmented on a zoomed region at their insertion into the chordae in the images obtained with high-resolution cryo-CECT (protocol n°3). Segmentation was performed using the *Magic wand tool*, then *Remove small spots* was used to erase undesired small regions. Finally, a vessel was visually identified and segmented manually using the *Magic wand tool*.

4.5.5 Leaflet insertion

The segmentation process of the various sub-branches of the chordae involved the following steps. First, the segmentation of the "outer light layer" was performed to separate the sub-branches. The segmentation was achieved by using the *Magic wand tool* along the leaflet insertion to accurately delineate the outer layer of the chordae (sub-)branches. Subsequently, the segmented "outer layer" was employed as a contour to effectively separate the distinct chordae sub-branches.

4.5.6 Chordal layers

Using high-resolution cryo-CECT of the muscle region (protocol n°3-4), bright laminae were observable in the elastin-rich outer layer of the chordae. Segmentation of those laminae was performed using the *Histogram tool* and cropping the histogram to highlight those structures. Then, on 2D axial sections, in the region where they were separable visually, the number of those laminae was counted every 50 slices.

5 Results and discussion

To analyze the macro- and microstructure of chordae tendineae, this master thesis aimed to investigate the distinct (sub)structures of interest described previously in Chapter 2, and observed in our sample. The research involved a systematic examination of each (sub)structure to determine the most suitable acquisition protocol. Additionally, a thorough evaluation of microstructural parameters was conducted. Alongside examining anatomical and morphological characteristics, this study focused on examining specific microstructures, including adipocytes, fibre organization, the junctional zone, blood vessels, muscle fibres, and chordal layers. Those substructures are visible in the supplemental videos of the muscle insertion, for high-resolution CECT (protocol n°2) (Supplementary video 1 [link: Video 1]) and cryo-CECT (protocol n°4) (Supplementary video 2 [link: Video 2]).

5.1 Anatomical features and morphology

Based on a visual examination of the sample, two distinct chordae were identifiable, both of which insert at the edge of the first scallop of the posterior leaflet. They are therefore referred to as marginal chordae as discussed in Section 2.2.4.1 (Fig 5.1.A). The left one appeared more round, while the right one is more flat (Fig.5.1.B). A translucent sheath is visible on both sides of this chord, extending from the branching of both chordae to the leaflet, which is only visible at the upper end of the right chord (Fig.5.1.B). The analysis of dissected chordae alone (Fig.5.1.B) is insufficient for anatomical assessment, classification, and characterization in the context of MV study. It remains essential to rely on visual inspection of the complete MV apparatus to determine the origin and placement of the chordae tendineae. This aspect should be duly considered when investigating the chordae tendineae, as their type and location might have an impact on their macro- and microstructure as described in Section 2.2.4.4. In the present study, while focusing on individual chordae, meticulous tracking of their respective origins was imperative to ensure comprehensive understanding.

The low-resolution CECT (protocol n°1) enabled more detailed visualization of the sub-branches at the insertion into the leaflet (Fig.5.2.A) and was therefore used. Indeed, three chordae were visible (Fig.5.2.B) instead of only two visually detected (Fig.5.1.B). The low-resolution CECT (protocol n°1) enabled the acqui-

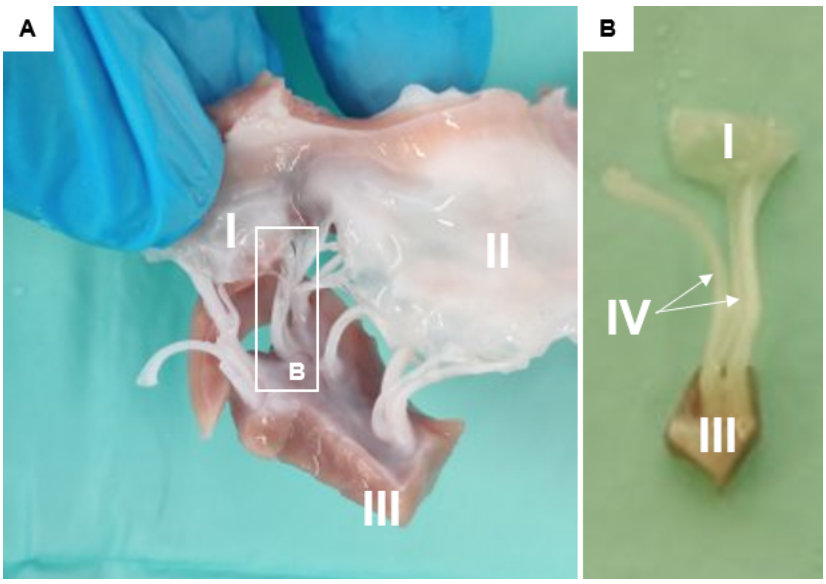

Figure 5.1: Visual assessment of the chordae anatomy and macromorphology. (A) Mitral valve apparatus with the chordae used in this study, the white inset is shown in (B). (I) The anterior leaflet,(II) P1, the first anterior scallop of the posterior leaflet, (III) papillary muscle. (B) Chordae used in this study and dissected from the mitral valve (I) the posterior leaflet,(III) the PM and (IV) 2 chordae visible.

sition of the entire volume of the sample, which in turn facilitated precise quantification of the morphometric parameters of the sample (Fig.5.2.C-D-E). For instance, with this technique, it was first possible to manually evaluate the length of the three individual chordae identified (Fig.5.2.B). To measure the length of the chordae tendineae, a digital cut was employed to separate them from the leaflet and muscle insertion; however, it should be acknowledged that this visually located cut may introduce inaccuracies. Given the inherent merging of the leaflet and muscle within the chordae, there is currently no definitive method to precisely determine their starting and ending points. Consequently, it is crucial to establish a reliable protocol for identifying the exact boundaries of the chordae, as this is essential for comparative analysis of their size. Such a protocol was not developed in this study since it would necessitate investigations of different chordae tendineae and the evaluation of different parameters at different scales. However, further studies may investigate macrostructural parameters such as the cross-sectional area that might increase at the leaflet and muscle insertion as subsequently discussed or microstructural parameters like the orientation of the fibres. The ability to accurately evaluate in 3D and at multiple scale chordae tendineae is therefore crucial and further highlights the added value of CECT and cryo-CECT. That said, the measured lengths are respectively 5.7, 6.71 and 6.52 mm for chordae 1,2 and 3. By automatically tracing the centreline of the first chorda, an evaluation of its curved length was also performed. The curved length is a more accurate measure than what could be obtained manually because it accounts for the curvature and overall mounting of the sample and is 10.42 mm for the chorda 1. The difference between the curved length for the same chorda may be attributed to inaccuracies while manually measuring the length or to the nature of both measures. Automated methods are more consistent and precise, reducing the variability inherent in manual measurements that may be prone to human errors and discrepancies.

Low-resolution CECT (protocol n°1) also renders it possible to quantitatively evaluate the variation in cross-sectional area along the height of the sample (Fig.5.2.D). Chorda 1 was thinner in the middle and had the

largest area at the bottom end. The mean cross-sectional area was 0.27 mm^2. The cross-sectional shape was also assessed in terms of the aspect ratio, which is the ratio between the length and width of the axial cross-section of the chorda. A ratio of 1 means that the chorda has a round shape. Assessment of the chorda 1 exhibits that it is less circular in the upper end, at the leaflet insertion (Fig.5.2.C). Lower in the chorda, a region is almost circular and overall, the aspect ratio is closer to 1 at the bottom of the chorda. The average shape ratio was 0.35.

Both the cross-sectional area and the aspect ratio variation along the chordae could be used to assess the anatomical variation due to a disease as previously done in the literature for the mitral regurgitation [69]. The aforementioned study focused solely on primary chordae, as the number and distribution of secondary chordae exhibited significant variation among individuals. Consequently, it underscored the necessity for standardizing measurement methodologies for this chordae subtype. However, the application of low-resolution CECT offers the potential to address this limitation by enabling a more precise 3D assessment and facilitating automated measurements of chordae length and area [69].

It is worth mentioning that chorda 1 was the only one to be extensively studied because it is the only one that could be accurately segmented as a single individual. Chordae 2 and 3 could not be segmented as individuals for several reasons. First, the exact branching point between them could not be precisely located. Second, there is a partial volume effect between their outer layers. Both chordae, therefore, appeared merged in some places and could not be divided automatically. While an inaccurate segmentation of the chordae should not have an impact on their curved length, it is likely that the cross-sectional shape and area would be impacted and would not reflect the true anatomical features of the chordae and were therefore not investigated. This issue could be avoided when the chordae would be positioned apart during the sample mounting for CECT imaging.

At present, numerical predictive models are predominantly used by researchers to comprehend the functioning of the complete MV apparatus, but these models are unable to consider morphological variations due to the absence of 3D reconstruction of the MV [70]. The acquisition protocol used in this study confirmed that low-resolution CECT has the capability to account for the anatomical variations of the chordae and enable 3D modelling. Nonetheless, given that only individual dissected chordae were examined, the anatomical positioning and classification of the sample should be visually assessed while still attached to the entire MV apparatus.

In conclusion, our investigations show that low-resolution CECT is an appropriate imaging technique for the 3D characterization of morphological parameters of the chordae, but additional research is necessary to determine the possibility to image the complete MV sub-apparatus at once with low-resolution CECT. Such research would likely involve the development of another sample holder that permits the visualisation of the MV apparatus at low resolution, which may be challenging because our results revealed that the positioning of the chordae tendineae has an impact on image processing and analysis. When situated next to each other, the different chordae were still observable, but could not be automatically segmented as distinct structures. Further studies should take this into account when investigating the potential to examine the entire MV sub-apparatus.

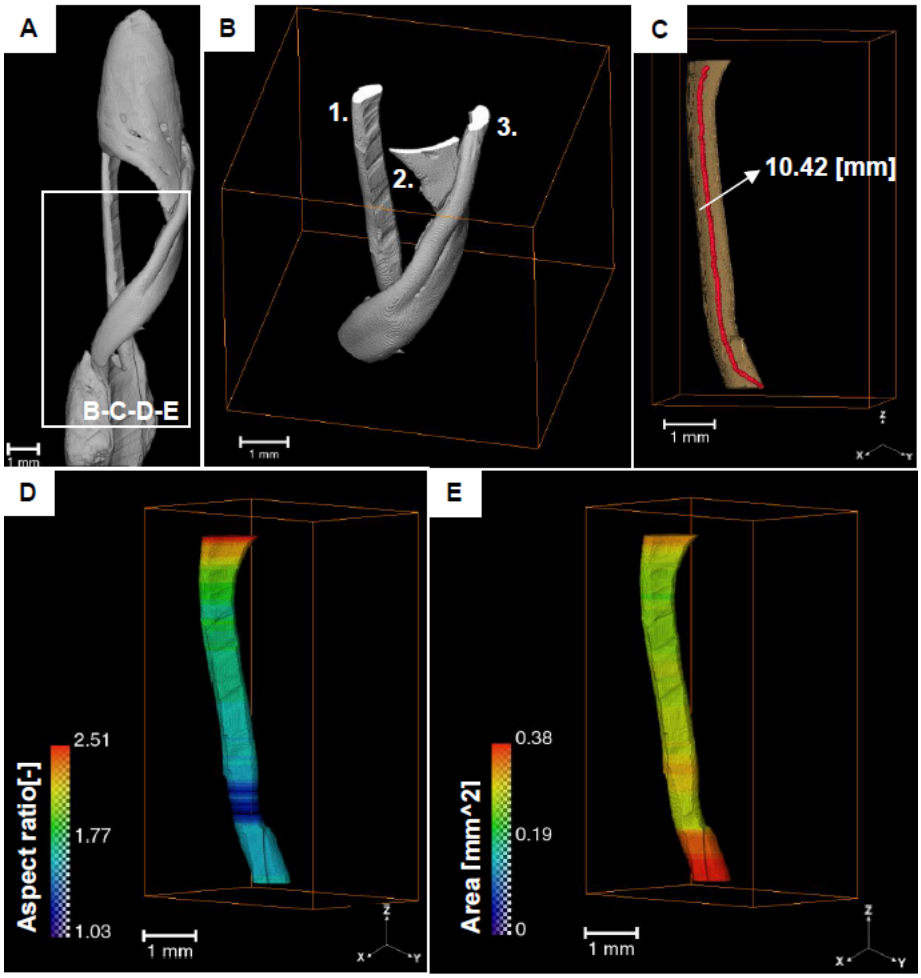

Figure 5.2: Quantitative assessment of the chordae morphology. (A) 3D rendering of the entire sample obtained with low-resolution CECT (protocol n°1). The white inset indicates the zoom region used in (B) where three chordae are visible. (B) 3D rendering of the zoomed region obtained with low-resolution CECT (protocol n°1) in which individual chordae are respectively named 1,2 and 3. Chorda 1 is represented in (C-E). (C) 3D rendering of the first chorda, the centerline (red) was used to assess the curved length of the chorda which is equal to 10.42 mm^2. (D) 3D rendering of chorda 1 coloured depending on the aspect ratio. (E) 3D rendering of the chorda 1 coloured depending on the cross-sectional area. The evolution of the axial cross-sectional area over the height of chorda 1 is observable.

5.2 Adipocytes

5.2.1 Comparison between different acquisition protocols

In addition to the challenges in visualizing and analysing the complete chordae tendineae with low-resolution CECT due for example to the impact of the positioning on image processing and analysis, the comparison of 2D axial sections of the same region of the sample (Fig. 5.3.I) obtained with different protocols exhibited several differences (Fig.5.3.A-H).

Since every dataset was not normalized, the contrast difference between adipocytes and surrounding tissue for the different protocols was not investigated. However, a comparison between low-resolution (protocol n°1) (Fig.5.3.A-B) and high-resolution CECT (protocol n°2) (Fig.5.3.C-D) shows the important difference

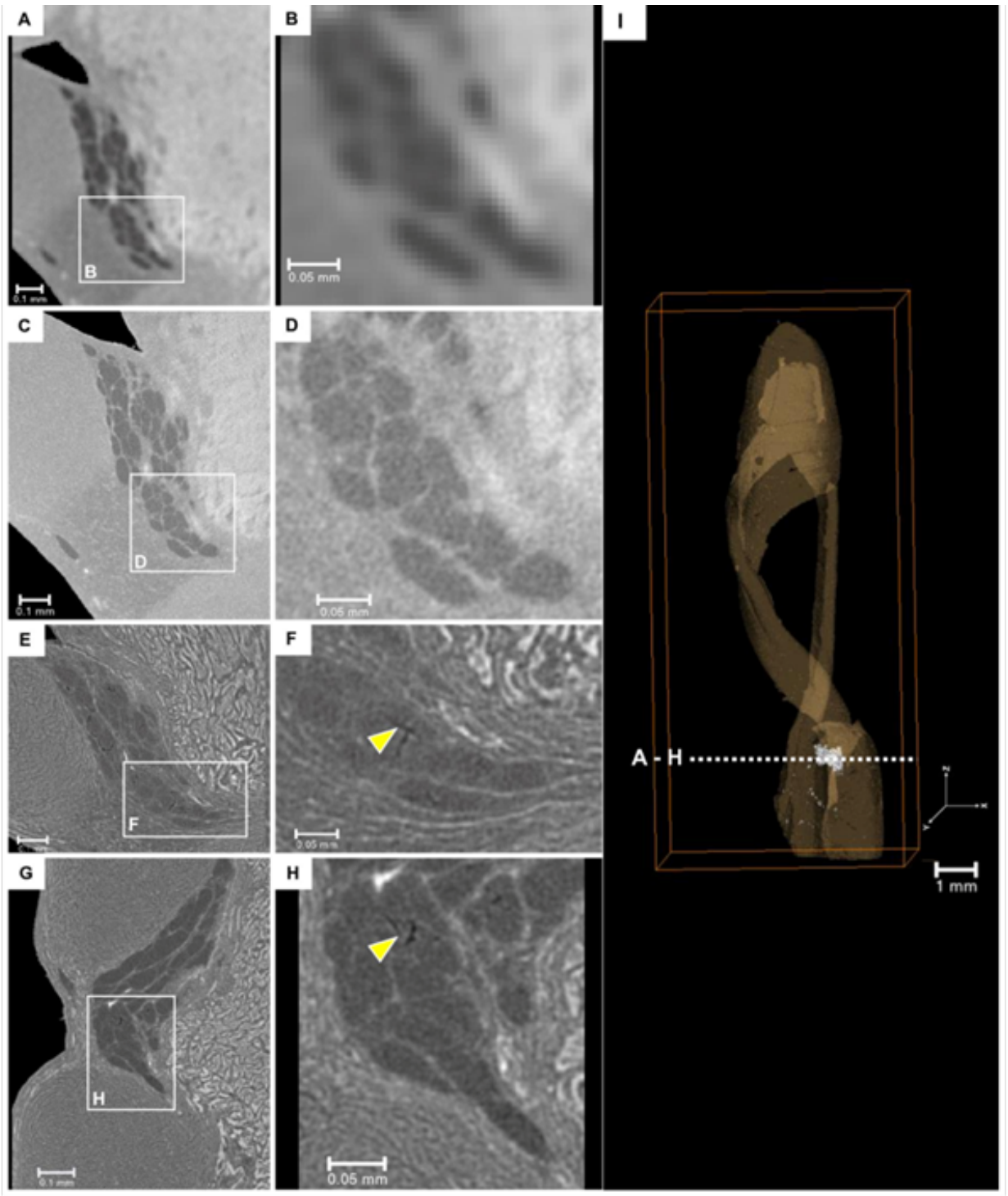

Figure 5.3: Qualitative comparison of the visibility and preservation of the adipocytes between different acquisition protocols. (A-H) 2D axial section of the muscle insertion region containing adipocytes, obtained with low-resolution CECT (protocol n°1)(A-B), high-resolution CECT (protocol n°2)(C-D), high-resolution cryo-CECT (protocol n°3) (E-F) and high-resolution cryo CECT (protocol n°4) (G-H). The white inset shown on images of the left column corresponds to the zoom region used in the right column. (B) shows the zoomed region with low contrast between the adipocytes and the surrounding tissue due to partial volume effect, (D) the zoomed region, where there is satisfying contrast between the adipocytes and the surrounding tissue, and (F) where identifying individual adipocytes is difficult and a dark region is observable (yellow arrow). In comparison to (E), individual adipocytes are identifiable more easily in (H) and a dark region is also shown (yellow arrow). (I) 3D rendering of the entire sample obtained with low-resolution CECT (protocol n°1). The white dotted line indicates the location of the axial regions used in (A-H).

in adipocyte visual delimitation with the surrounding. Using low resolution, the adipocyte outlines were blurred. This may be due to the partial volume effect, i.e., the attenuation within a single voxel is influenced by the mixture of multiple different tissue types or materials within that voxel. It is therefore likely that a voxel size of 6.8 μm is not sufficient to correctly identify individual adipocytes. Nonetheless, the low resolution allows the overall visualisation of adipocytes.

Compared to high-resolution CECT (Fig.5.3.C-D), adipocytes are difficult to differentiate from the surrounding tissue based only on the grey value with high-resolution cryo-CECT (Fig.5.3.E-F). Moreover, black areas are visible at different locations in the adipocytes only with cryo-CECT (Fig.5.3.F (yellow arrow)). They may be a consequence of the freezing process, which might cause segregation of the CESA in the region due to ice crystal growth.

The second high-resolution cryo-CECT protocol (protocol n°4) has a temperature of freezing of -80°C. In 2D axial sections (Fig.5.3.G-H), only one dark area (Fig.5.3.H (yellow arrow)) was observed while five could be counted using a -45°C freezing. Since fast freezing at -80°C was applied after the one at -45°C, the disappearance of the black regions supports the hypothesis that the fast freezing at -45°C did not induce permanent deformation of the tissue. If it was the case, those black regions could have been assimilated to fissures in the tissue. The hypothesis of segregation is, therefore, likely.

Moreover, when performing CECT (protocol n°1-2) and cryo-CECT at -45°C (protocol n°3), the chordae were more stretched apart than using high-resolution cryo-CECT at -80°C (protocol n°4) and the fibres that make up the region located between them are subjected to distinct stresses. This may also have an impact on the visibility of the adipocytes.

In conclusion, high-resolution CECT allows the best visualisation of the adipocytes with satisfying contrast between fat droplets and surrounding tissue. Images of the muscle insertion region obtained using this protocol were therefore used to assess the microstructure of the individual adipocytes. Since a precise segmentation of individual fat droplets was not needed to evaluate their overall location through the full volume of the sample, low-resolution CECT of the full volume of the sample (protocol n°1) was also used.

5.2.2 Microstructural assessment

Low-resolution CECT of the full volume of the sample (protocol n°1) showed that a majority of the adipocytes were located near the muscle insertion region (Fig.5.4.A) and none are located in the chordae nor in the leaflet insertion. In the literature, the role of adipose tissue in the mitral valve has primarily been focused on the leaflet. Studies have produced conflicting results; some studies suggest that adipocytes are consistently present in the mitral valve structure [71], while others link their presence to rheumatic mitral valve disease [72]. No data were available to assess the role nor the proportion of fat droplets in the lower part of the MV apparatus. However, fat droplets were studied in the cardiac muscle and a lot of studies relate the presence of adipocytes in the heart as detrimental and correlated with obesity [73]. Moreover, the presence of adipocytes was also studied in other tendons, e.g. around Achilles tendon [74, 75], and between parietal and visceral layers of the paratenon in rat tail tendon [76].

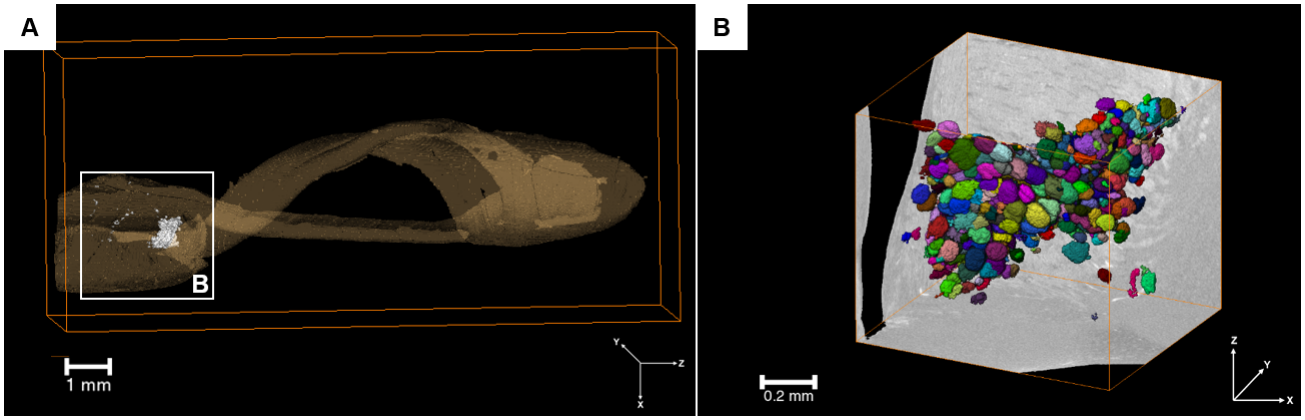

Figure 5.4: Qualitative assessment of the location and packing of the adipocytes. (A)3D rendering of the entire sample obtained with low-resolution CECT (protocol n°1). The white inset indicates the zoom region used in (B) where most of the identified adipocytes lie. (B) 3D rendering of the zoomed region obtained with high-resolution CECT (protocol n°2) in which individual adipocytes are represented in different colours.

Overall, the function and presence of fat droplets in muscle and tendon are still not fully understood, some of the proposed explanations being energy storage, structural support and inflammation modulation [77]. Depending on their shape, individual fat droplets have different functions [77]. A previous study on rat myotendinous junction showed that the arrangement of the surrounding collagen fibres has an impact on adipogenesis i.e., the process by which undifferentiated mesenchymal stem cells differentiate into adipocytes. The same study also showed that adipocyte development was mainly observable in regions with unorganised collagen fibres that are mostly located near the muscle insertion [78]. To better understand the role of the adipocytes, it is, therefore, necessary to assess their microstructure and arrangement.

The 3D qualitative assessment obtained in this study for adipocytes showed that a majority of them were packed in the region between the two chordae by the side of the muscle tissue. Based on its position, we can hypothesize that the function of this fat depot is mechanical and that this "fat pad", previously described by Z.jin *et al.*, may reduce friction between the chordae and the muscle during repeated elongation cycle [79]. However, while the current study allowed to assess the packing and location of fat droplets throughout the sample, it is premature to assert the role of the fat droplets observable and further studies on other chordae tendineae should be performed.

Quantitatively, several parameters can inform the function of individual droplets and the overall fat depot. First, hyperplasia and hypertrophy of the fat tissue respectively refer to an increase in the number of adipocytes in a given tissue and an increase in their volume. Larger adipocytes have a higher lipid content and secrete more chemoattractants e.g., cytokines, chemokines, and complement proteins [80]. Adipose tissue expansion by hypertrophy and hyperplasia can be referred to as hypertrophic growth and can be related to fibrosis, hypoxia or inflammation of the fat tissue. The hyperplasia can be caused by obesity and is associated with elevated levels of insulin during fasting and reduced responsiveness to insulin [81]. The number of identified droplets (n = 600), can therefore inform on possible hyperplasia [81] and the volume of individual adipocytes (Fig.5.5.B) on possible hypertrophy.

Based on high-resolution CECT (protocol n°2), the sphericity of the individual fat droplets was investigated (Fig.5.5.A). It is a value ranging from 0 to 1. 1 can be assimilated to a perfectly round object and 0 means

an irregular shape. For the adipocytes, the sphericity is related to the degree of lipid droplet packing within the adipocyte, a lower sphericity could be related to a higher ability to store lipids [81]. Our results show that individual droplets had highly variable sphericity ranging, from 0.3 to 0.9.

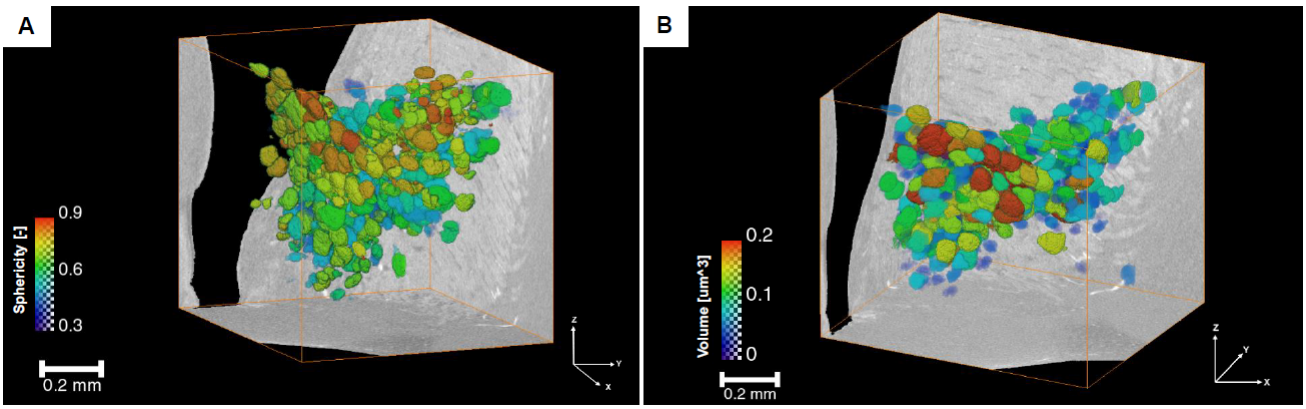

Figure 5.5: Quantitative assessment of the sphericity and volume of individual adipocytes.(A) 3D rendering of the zoomed region represented in the white inset in (Fig.5.4.A) obtained with high-resolution CECT (protocol n°1), individual adipocytes are coloured depending on their sphericity, red adipocytes have high sphericity while blue has lower one. The sphericity varies from 0.3 to 0.9 [-], and the mean sphericity is 0.64. (B) 3D rendering of the zoomed region (Fig.5.4.A) obtained with high-resolution CECT (protocol n°2), individual adipocytes are coloured depending on their volume, red adipocytes have a bigger volume. The volume varies from 0 to 0.5 um^3. The colourmap upper limit is 0.2 um^3 in order to highlight the variability between smaller individual adipocytes. The mean volume is 0.05 um^3.

Based on the 3D rendering of the adipocytes showing the volume and sphericity of individual droplets (Fig.5.5.A-B), the largest adipocytes were located in the centre of the fat depot and had volumes below 0.5 μm^3. Further studies may focus on imaging different samples to be able to compare the proportion, packing, volume and sphericity variation from one sample to the other.

In conclusion, there is to date limited research investigating the 3D microstructure, location, and distribution of adipocytes within the chordae tendineae. However, this study provides new insights by demonstrating the utility of low- and high-resolution CECT for analyzing the 3D microstructure of adipocytes in this tissue and proposing image processing and analysis workflow to assess parameters of interest.

5.3 Muscle, collagen and elastin fibres organisation

5.3.1 Comparison between acquisition protocols

Comparison between 2D sagital sections of the same sample obtained with different imaging protocols showed that high-resolution cryo-CECT (protocol n°3-4) is the only one allowing visualisation of individual muscle and collagen fibres (Fig.5.6). At higher resolution CECT (protocol n°2), little improvement was observed but, no individual fibres were visible nor are their overall orientation. In comparison with CECT, high-resolution cryo-CECT allowed the visualisation of some individual fibres, which had a crimped shape, and their overall orientation was visible. It is worth mentioning that a beam hardening artefact was observed as the edge of your samples was much more pronounced than the rest (Fig.5.6). Beam hardening is due to an energy increase of the beam as it passes through the sample, the recognition and avoidance of those types

of artefacts have been described in the literature [82].

A visual comparison between high-resolution cryo-CECT with a FF at -80°C and FF at -45°C showed no significant differences in fibre detection. Both cryo-CECT protocols had the same performance in terms of image quality but in terms of practical considerations, the use of FF at -45°C necessitates an additional heating step, rendering it less convenient. From the four different imaging protocols to image the muscle insertion region, high-resolution cryo-CECT with fast freezing at -80°C (protocol n°4) was, therefore, the one used to analyse the microstructure of the fibres in the chordae tendineae. That said, it is premature to assert that a fast freezing temperature of -80°C is optimal. Indeed, A. Maes *et al.* previously studied different freezing methods to optimize visualisation in muscle and Achille's tendon tissue. In this previous study, the optimal freezing temperature described was -20°C for a tendon. Further study may therefore investigate other freezing temperatures to determine if FF at -80°C truly is the best freezing temperature and whether better visualisation cannot be achieved.

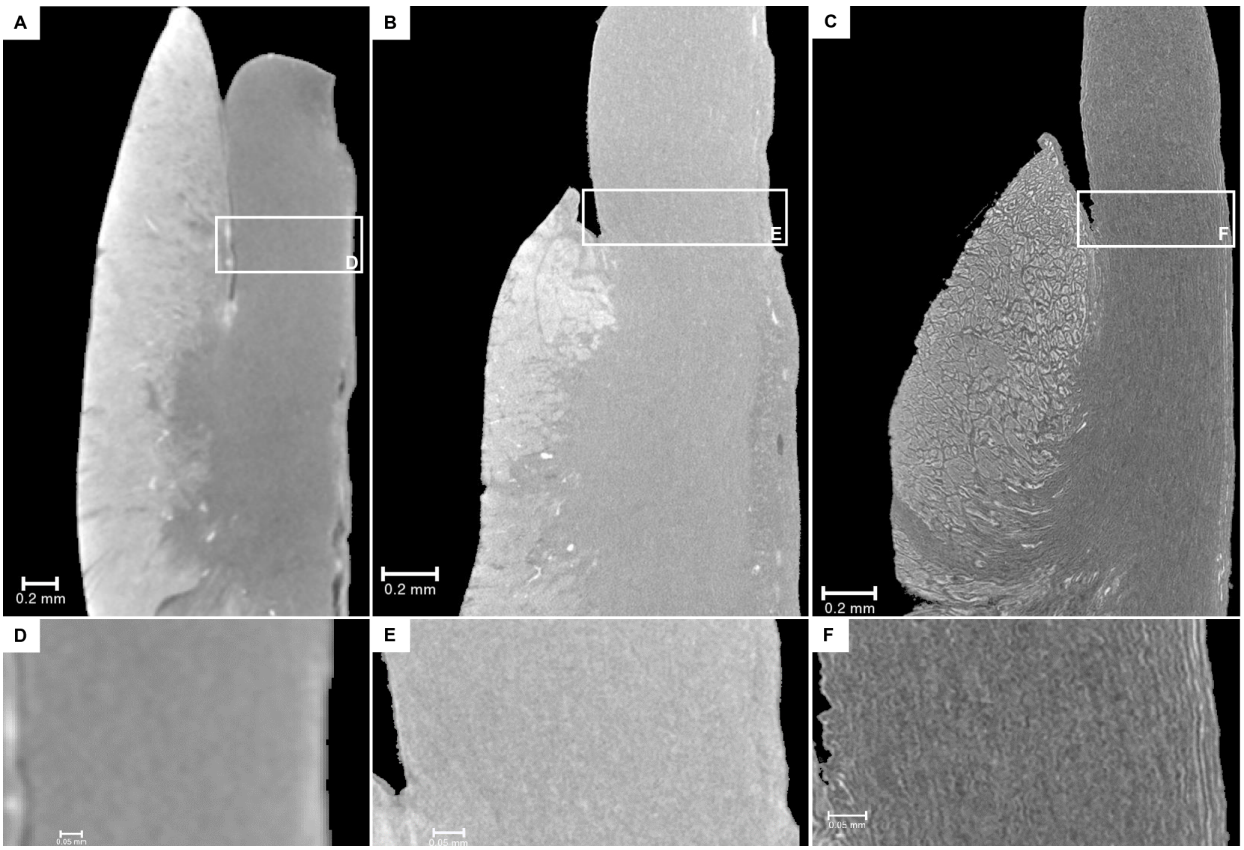

Figure 5.6: Qualitative comparison of the visibility and preservation of the fibres. (A-F) 2D sagital section of the muscle insertion region obtained with low-resolution CECT (protocol n°1) (A-D), high-resolution CECT (protocol n°2) (B-E) and high-resolution cryo-CECT (protocol n°4). (A) Sagital section of the sample with visible beam-hardening, in the dotted white inset. (D) Zoomed region where the chorda is homogeneously grey and no fibres are visible. (E) No fibres are visible but in comparison to (D), the centre of the chorda is not homogenously grey. (F) Individual fibres are observable and have a crimped shape.

5.3.2 Microstructural assessment

Qualitative assessment of the fibre organisation in the muscle insertion allowed the identification of different regions (Fig.5.7.B). Closer to the leaflet, the fibres were more crimped (Fig.5.7.B (I)). Inversely, near

the muscle insertion (Fig.5.7.B (II)), the fibres were less densely packed and seemed more elongated, and less crimped. The orientation of the fibres also varied going from parallel to the chordae long axis in the region I (Fig.5.7.B (I)) to perpendicular when inserting into the muscle. The overall organisation also varied with fibres heterogeneously oriented when inserted into the muscle. Another region could be distinguished, which is located in the outer layer of the chordae and was composed of highly stained laminae (Fig.5.7.B (IV)). This layer was visible all around the chorda before insertion into the muscle and also covered the surface of the muscle after the insertion of the chordae. Muscle fibres (Fig.5.7.B (III)) also changed in shape and thickness when inserted into the chorda compared to fibres located the furthest from the insertion. The fibre orientation qualitatively assessed is consistent with what was previously described in Section 2.2.4.2, and all the other features such as the crimping and fibre concentrations visible with high-resolution cryo-CECT were already described in previous studies using classical 2D histology and SEM.

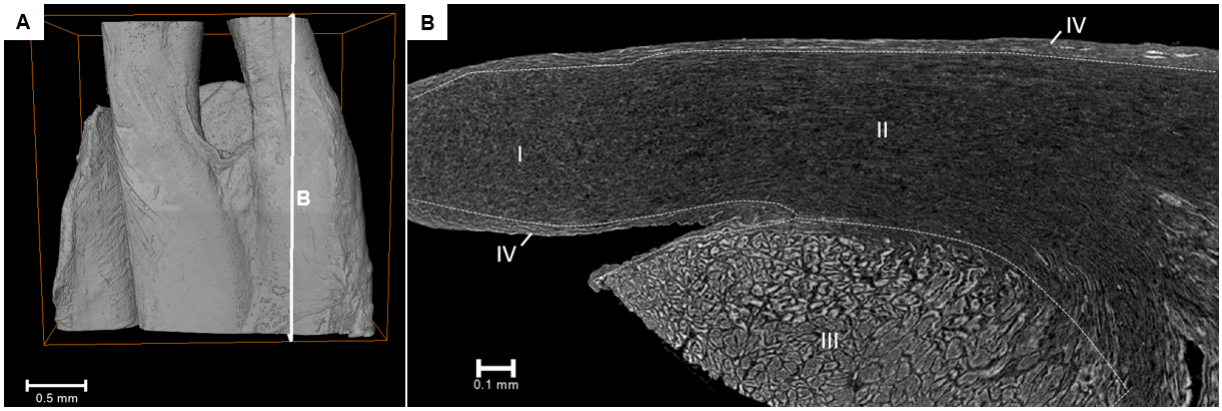

Figure 5.7: Qualitative assessment of the fibre organisation and orientation.(A)3D rendering of the muscle insertion obtained with high-resolution cryo-CECT (protocol n°4). The white line indicates the position of the cut in (B) where the fibre organisation and orientation is observable. (B) 2D sagittal section showed in (A), the organisation of the fibre is visible with a region more densely packed and crimped (I), a looser and less crimped region (II), the muscle fibres (III) and outer sheaths (IV).

Nevertheless, in addition to the identification of different regions in the chordae tendineae at its insertion site to the PM, cryo-CECT allowed studying the orientation of the fibres in 3D. The local orientation was numerically assessed in every subvolume of the sample and was visualised in 3D (Fig.5.8.A-B). It is possible to see how the orientation of the muscle and collagen fibres are arranged through the sample, notably in the muscle insertion where the change in orientation of phi can be observed (Fig.5.9.A-B), and the colourmap from the muscle to the centre of the chorda gradually goes from hot to cold tones. This means that muscle fibres were oriented horizontally, while collagen fibres in the centre of the chorda are mainly oriented vertically, and at the insertion of the collagen fibres into the muscle, a gradual change of orientation is visible (Fig.5.9.C-D). The theta orientation, which informs on the angle that segments make with the positive x-axis is measured from the x-axis towards the xy-plane. In other words, theta determines the horizontal direction of the segments and its quantitative assessment shows in the axial section (Fig.5.10.A-B), that muscle orientation varies gradually until the insertion, the chordae core which is overall filled with cold tones.

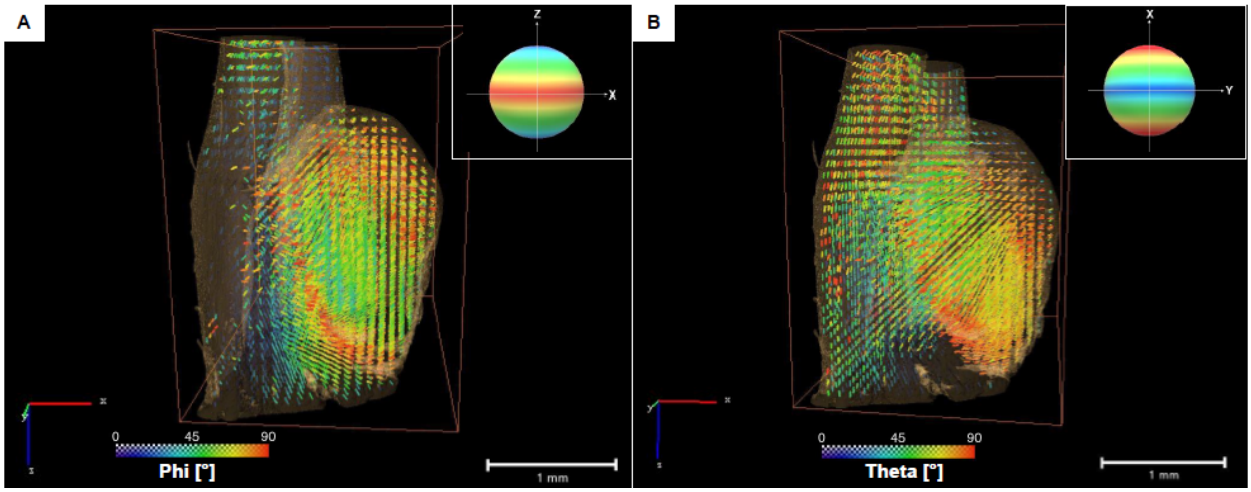

Figure 5.8: Quantitative assessment of the orientation of the muscle and collagen fibres. (A) 3D rendering of the muscle insertion obtained with high-resolution cryo-CECT (protocol n°4). Segments oriented in the direction of local orientation are visible and coloured based on their phi orientation. In the white inset, an interpretation of the phi orientation and the colourmap is represented, hot tones mean that the segments are oriented in the xy-plane . (B) 3D rendering of the muscle insertion obtained with high-resolution cryo-CECT (protocol n°4). Segments oriented in the direction of local orientation are visible and coloured based on their theta orientation. In the white inset, an interpretation of the theta orientation and the colourmap is represented, cold tones mean that the segments are oriented in the yz-plane.

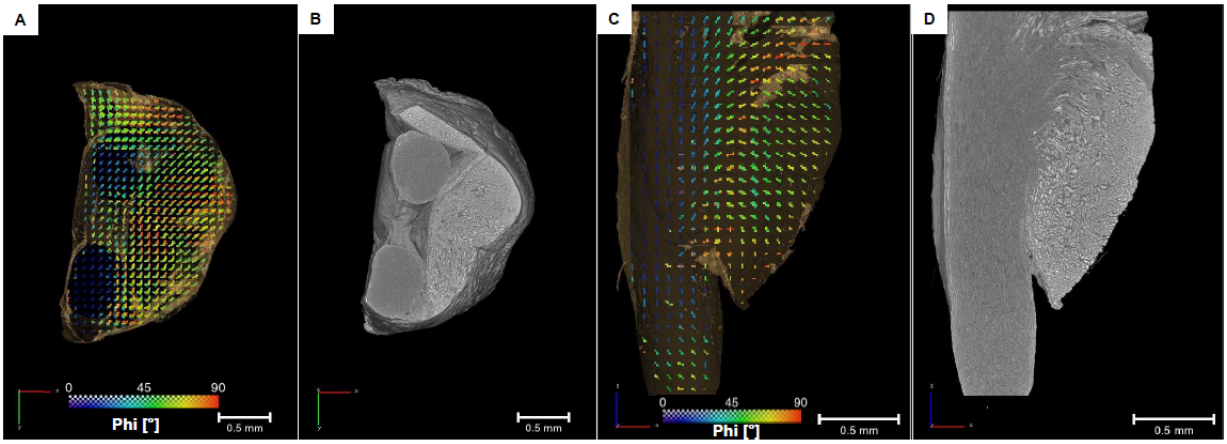

Figure 5.9: Qualitative assessment of the phi orientation of the muscle and collagen fibres. (A) 3D rendering of the muscle insertion obtained with high-resolution cryo-CECT (protocol n°4) from an axial point of view, the coloured segments are visible and in the middle of the muscle insertion, blue segments are located in the centre of the chordae. (B) 3D rendering of the muscle insertion obtained with high-resolution cryo-CECT (protocol n°4) represented in (A), both chordae are visible at the left. (C) 3D rendering of the muscle insertion obtained with high-resolution cryo-CECT (protocol n°4) from a sagittal point of view, the coloured segments are visible and in the middle of the muscle insertion, blue segments are located in the centre lower part of the chorda visible, the orientation change from the muscle to the chorda is visible with muscle fibres gradually changing orientation from horizontal to vertical. (D) 3D rendering of the muscle insertion obtained with high-resolution cryo-CECT (protocol n°4) from a sagital point of view represented in (C), the chorda centre is darker and the fibre orientation is visible. The phi orientation variation through the sample can be found in the supplemental video (Supplementary video 3 [link: Video 3]).

Segmentation of individual collagen fibres was not possible when using our high-resolution cryo-CECT of the muscle insertion (protocol n°3-4), and microstructural parameters of individual collagen fibres such as the orientation. It is also worth noting that the local orientation of the fibres was only performed on the muscle insertion region and not on the leaflet insertion because high-resolution cryo-CECT (protocol n°4) did not allow for visually assessing the overall orientation of the fibres. Since the method used to analyse the local

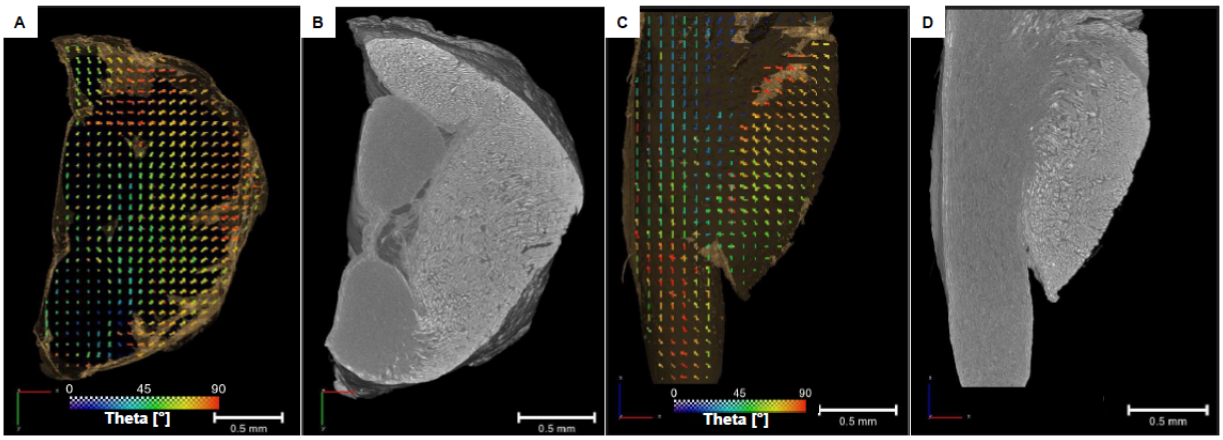

Figure 5.10: Qualitative assessment of the theta orientation of the muscle and collagen fibres. (A) 3D rendering of the muscle insertion obtained with high-resolution cryo-CECT (protocol n°4) from an axial point of view, the coloured segments are visible.(B) 3D rendering of the muscle insertion obtained with high-resolution cryo-CECT (protocol n°4) represented in (A), both chordae are visible at the left. (C) 3D rendering of the muscle insertion obtained with high-resolution cryo-CECT (protocol n°4) from a sagital point of view, the coloured segments are visible. (D) 3D rendering of the muscle insertion obtained with high-resolution cryo-CECT (protocol n°4) from a sagital point of view represented in (C), the chorda centre is darker and the fibre orientation is visible. The theta orientation variation through the sample can be found in the supplemental video (Supplementary video 4 [link: Video 4]).

orientation relies on the ability to crop the grey-value histogram and focus the analysis on the overall fibres, performing the local orientation analysis on the leaflet orientation was not achievable. Also, the variation of the fibre architecture in chordae tendineae at the insertion into the leaflet, under varying mechanical loads was investigated in 2D with polarized spatial frequency domain imaging (pSFDI) in a previous study [83]. A similar investigation could be performed in 3D. However, it may be necessary to develop a new sample holder and preparation technique that would account for the difficulties already described such as the elongated shape of the sample or its small size while allowing to tune the stress applied to the sample. Finally, it is worth mentioning that the imaging and sample mounting protocols developed in the present study do not account for deformation due to possible stretching of the sample during mounting and further highlight the necessity to develop or enhance the current protocols to better account for such deformation. A good example of mechanically induced deformation of the sample can be seen in the "junctional zone" described in the subsequent section.

5.4 Muscle fibres

Having knowledge about muscle geometry, especially the arrangement of muscle fibres, holds great significance in creating biomechanical models for the musculoskeletal system. Currently, classical 2D histology is the most used method to collect such data [84]. However, CECT and cryo-CECT could be used to derive the architecture of the muscle fibre non-destructively and in 3D. Indeed, using cryo-CECT at high resolution (protocol n°3-4), it was possible to visualize the individual muscle fibres and segment them (Fig.5.11). It is therefore likely that using a similar method to what has been described by A.Maes *et al* for the assessment of individual muscle fibres could allow accurate quantification of the diameter, tortuosity and orientation of the individual fibres in the PM [20]. Such parameters could be useful for comparative microstructural studies

between diseased and healthy tissues, and overall modelling of the mitral valve apparatus. However, such a study was not performed in the context of this work and might be investigated in further studies. Compared to high-resolution cryo-CECT, CECT did not allow the visualisation of individual muscle fibres and therefore excluded a potential use of CECT for such investigations.

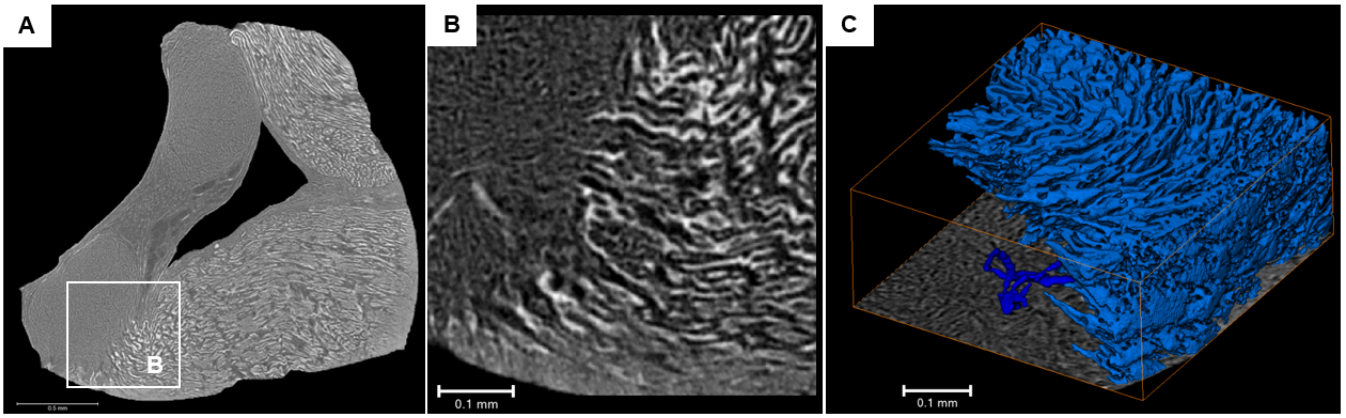

Figure 5.11: Qualitative analysis of the muscle fibres visibility and segmentation(A) 2D axial section of the muscle insertion region with cryo-CECT (protocol n°3). (B) 2D axial section of the zoomed region. (C) 3D rendering of the zoomed region, (light blue) muscle fibres; (dark blue) blood vessels.

5.5 Junctional zone

There is a visible difference between the experiments conducted using the second holder (toothpick) and the third one (half toothpick), i.e. protocol n°3 and protocol n°4. This difference is the most obvious in the region in between chordae, the "junctional zone". In the literature, chordae tendineae are described as tendons composed of a single fascicle, and in tendons, fascicles are surrounded by several layers called, the paratenon, the endotenon and the epitenon. The paratenon is a thin layer of connective tissue that surrounds the entire tendon and works as an elastic sleeve that provides a protective covering and allows for the tendon to slide smoothly against surrounding tissues. The epitenon is a layer of connective tissue that is made of a dense fibrillar network and surrounds individual bundles of tendon fibres within the tendon and provides mechanical support to the tendon and helps to distribute forces evenly across its surface. The endotenon is a slender connective tissue layer that ensheaths individual tendon fibres. Within the endotenon, its fibrils intertwine with the tendon fibrils, providing a cohesive binding force between them. It provides a protective covering for the fibres and helps to maintain their alignment within the tendon [85]. Together, these layers help to maintain the integrity and function of tendons, allowing for smooth movement and transmission of forces between muscles. It is plausible that the area referred to as the "junctional region" situated between the chordae (Fig.5.12) corresponds to one or more of these layers or analogous structures, and may be susceptible to mechanical strains. When examining the mounted chordae on the toothpick, a noticeable separation was observed, in contrast to the half-toothpick condition. This separation could be attributed to the disparity in the junctional region and underscores the significance of the sample holder and preparation, since chordae tendineae, being soft tissues, are extremely sensitive to stretching and may exhibit dissimilar microstructural characteristics from one trial to another.

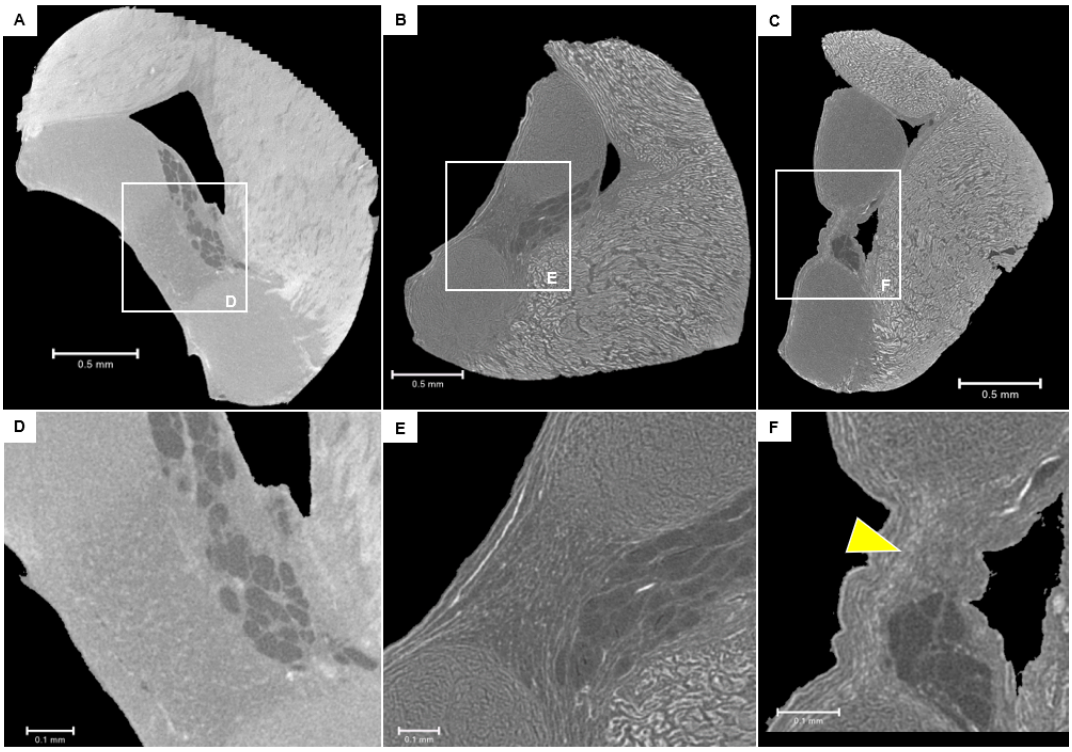

Figure 5.12: Qualitative comparison of the junctional zone between acquisition protocols.(A) 2D axial section of the muscle insertion obtained with high-resolution CECT mounted on the full toothpick (protocol n°2). The white inset is the zoom region shown in (D) with the junctional zone visible. (B) 2D axial section of the muscle insertion obtained with high-resolution cryo-CECT mounted on the full toothpick (protocol n°3). The white inset is the zoom region shown in (E) with the junctional zone visible. (C) 2D axial section of the muscle insertion obtained with high-resolution cryo-CECT mounted on the half toothpick (protocol n°4). The white inset is the zoom region shown in (F) with the junctional zone not visible and the two chordae are less stretched apart in comparison with (A) and (B). (D) In the zoomed region shown in (A), the junctional zone is overall homogeneously and comprised of vessels and fat droplets. (E) The zoomed region shown in (B), the junctional zone is composed of bright elastin fibres and dark interstitial spaces, vessels and fat droplets are also present. (F) Zommed on the junctional region shown in (C), the junctional zone is not visible and should be located at the indicated position (yellow arrow).

5.6 Vessels

5.6.1 Comparison between acquisition protocols

The 3D visual analysis of the CECT and cryo-CECT results revealed a reduction in the number of discernible vessels with the implementation of cryo-CECT. Vessels appeared bright in CECT images because the CESA used in this study, Hf-WD 1:2 POM, has a high affinity for connective tissue comprised in the vessel walls, but also to fibrin [86] which is a fibrous protein that is formed during the blood clotting process. The difference in the visibility of the vessels observed between both protocols (Fig.5.13) may be due to the fast freezing of the sample. During freezing, two processes occur, vitrification and crystallisation. The first mechanism is caused by a fast temperature decrease that traps the molecules in the disordered, amorphous, state. Conversely, crystal formation can be divided into two steps, crystal nucleation and growth, and will result in the crystal organisation of the molecules. Since the freezing rate is high, little crystal growth is expected. However, the difference observable between CECT and cryo-CECT may be due to the presence of blood clots that may react differently to the freezing. Indeed, it is likely that vitrification and nucleation

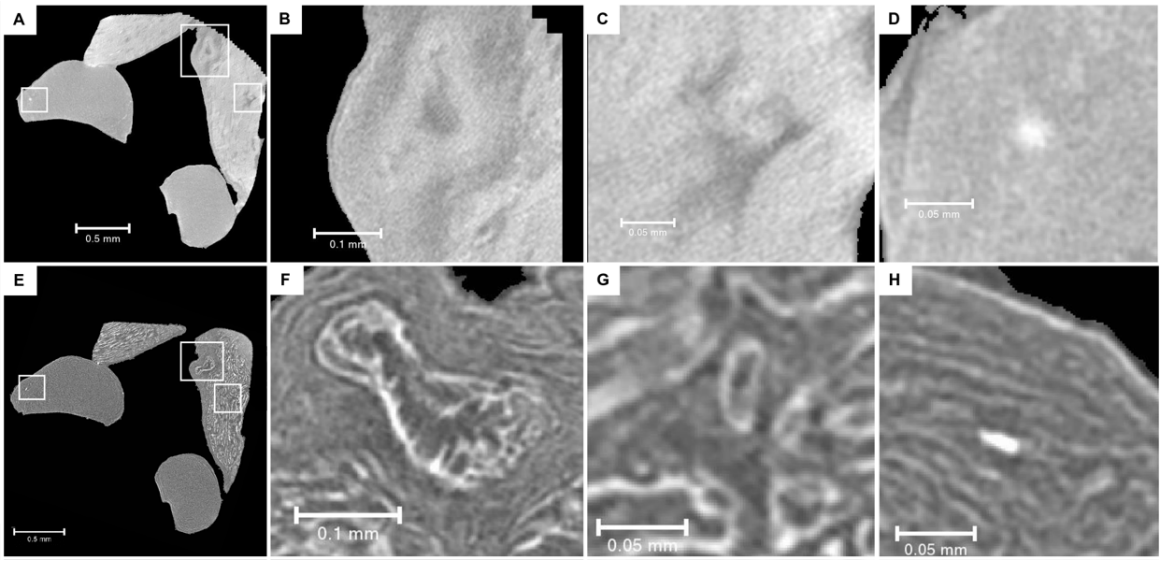

Figure 5.13: Comparison of the vessels visible between CECT and cryo-CECT, and vessels of different sizes. (A-D) 2D axial sections of the muscle insertion region with high-resolution CECT (protocol n°2), the white insets visible in (A) represent from left to right the vessels zoomed in (D), (B) and (C). (B) the large vessel is shown in (A). (C) Medium size vessel shown in (A), the lumen of the vessel is not clearly visible. (D) A small vessel running into the chorda appears as a bright and blurry dot. (E-H) 2D axial sections of the muscle insertion region were obtained with high-resolution cryo-CECT (protocol n°3) with the white insets indicating the 3 vessels of varying sizes corresponding to vessels shown in (A) and represented in (F-G-H). (F) The large vessel is shown in (E). (G) In the medium-sized vessel shown in (E), the vessel wall can be separated from the surrounding tissue and the lumen. (H) Small vessel running into the chorda shown in (E).

do not occur homogeneously and that nucleation may preferentially occur in the blood clots and may cause visual discrepancies because the CESA is insoluble in crystal ice. This phenomenon may locally impair vessel visualisation depending on the presence of blood and the size of the vessel and was investigated (Fig.5.13). Overall, the vessels exhibited better contrast with their direct surrounding when using cryo-CECT e.g., the lumen of the medium-sized vessels was not observable with CECT can be seen (Fig.5.13.C-G). For the small vessels (Fig.5.13.D-H), their segmentation is easier with cryo-CECT because there is an observable improvement in the contrast of the vessel compared to the surrounding tissue. For larger vessels (Fig.5.13.B-F), the same observation can be done because the vessel wall and lumen are visible. Hence, the underlying reason for the reduction in vessel visibility cannot be attributed to a decrease in the contrast between the vessels and surroundings using cryo-CECT.

Consistent with previous observations, analysis of the vessels detectable in multiple 2D axial sections across the sample showed a general decrease in the number of identified vessels when using cryo-CECT compared to CECT (Fig.5.14.A-B). However, vessels that are visible with CECT and not with cryo-CECT are primarily located within the muscle insertion and muscle fibres. Investigation of the visibility of the vessels in this region was therefore conducted on two identical axial sections (Fig.5.14). A vessel visible with CECT was identified in the corresponding section obtained with cryo-CECT (Fig.5.14.A-B). Visual assessment of the vessel corroborated with a previously described improvement of the contrast because the lumen not observable with CECT was visible with the implementation of cryo-CECT. However, an analysis of the contrast and grey-value intensity along a profile line going through the muscle tissue and the vessels exhibited that muscle fibres in the zoomed region had an intensity comparable to the one of the vessel walls. Using CECT,

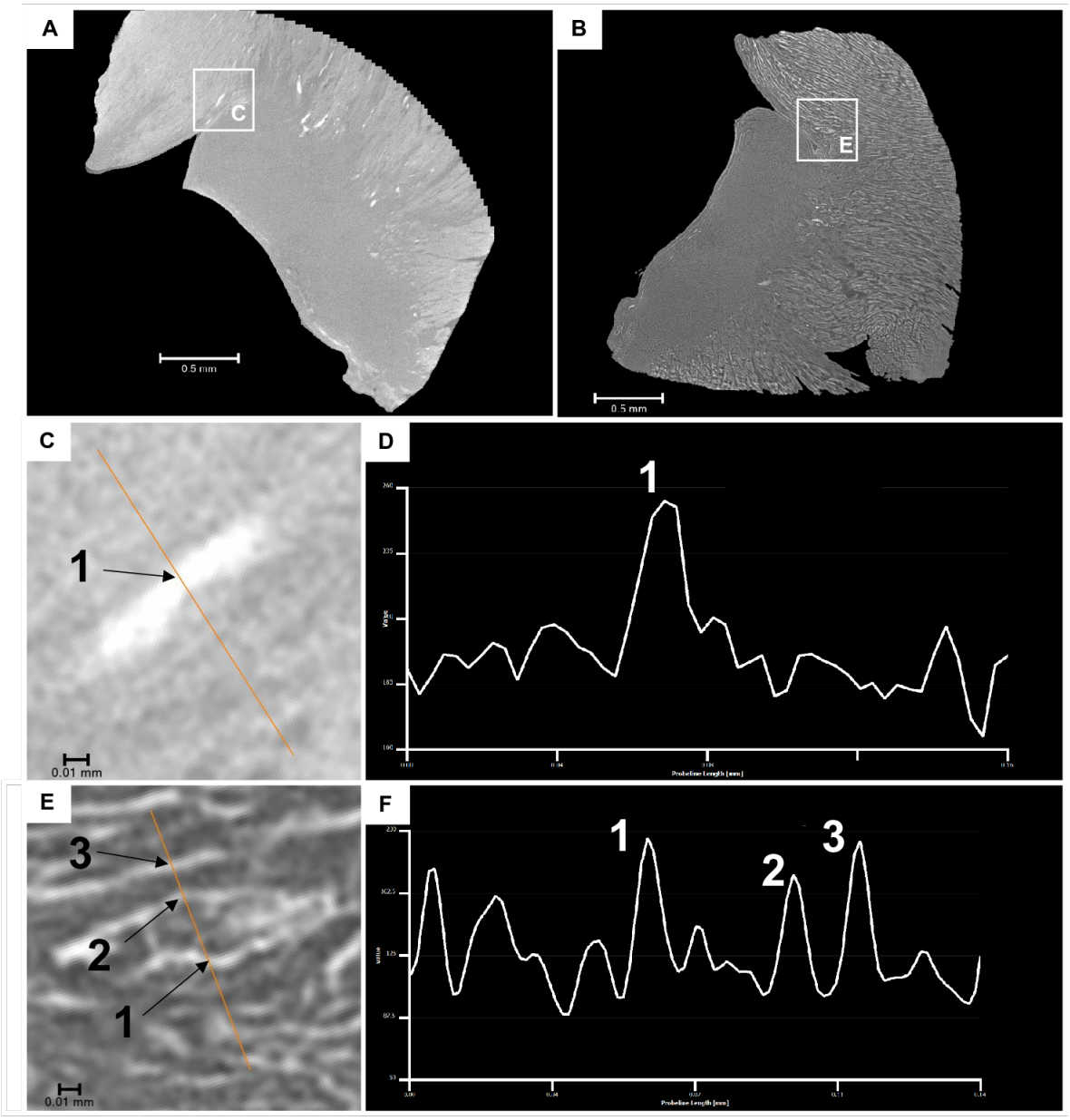

Figure 5.14: Quantitative comparison of the fibre visibility based on the number of observable vessels and contrast in the muscle insertion. (A)2D axial section of the muscle insertion region obtained with high-resolution CECT (protocol n°2) where there is plenty of vessels corresponding to the bright dots. The white inset indicates the zoom region used in (C) where a vessel is present. (B) Approximately the same 2D axial section of the muscle insertion region showed in (A) obtained with high-resolution cryo-CECT (protocol n°3). There are few vessels observable in the muscle region. The white inset represents the zoomed region used in (E). (C) The zoomed vessel is visible with the line traced through the thickness of the vessel and surrounding tissue used to evaluate the grey-value intensity in (D). One bright region can be visually observed and correspond to the vessel. (D) Grey value evaluated over the line traced in (C), one peak is visible and corresponds to the vessel. (E)The zoomed vessel is visible with the line traced through the thickness of the vessel and surrounding tissue used to evaluate the grey-value intensity in (F). Different bright lines are visible and correspond to the walls of the vessel (1-2) and muscle fibre (3). (F) Grey value intensity variation along the line shown in (E), 3 peaks can be identified and correspond to the vessel walls and muscle fibre visible in (E).

only one peak was observed while several were observed with cryo-CECT, and may imply that CECT could be preferred for the study of vessels running inside the muscle because they can be more easily identified. Moreover, the intensity variation between those peaks and valleys is larger using cryo-CECT. These findings

support the hypothesis that the decrease in the number of observed vessels could be attributed to their indistinguishability from the muscle fibres and must therefore be taken into account when performing image segmentation and analysis.
In summary, cryo-CECT and CECT are complementary methods for evaluating the microstructure of vessels in the chordae tendineae at the muscle insertion. Cryo-CECT enhances vessel visualization in regions where muscle fibres are absent with the possibility to visualize the vessel lumen, while CECT allows for the observation of vessels with less contrast between their direct surrounding regardless of their location in the sample.

5.6.2 Microstructural assessment of the vessel network

Low-resolution CECT (protocol n°1) of the full volume of the sample allowed visualisation of the blood vessels. A vessel is observed running straight along the left chorda without any visible branching (Fig.5.15). The majority of the vessels segmented were located in the muscle region and no vessels were observable in the leaflet insertion and upper part of the chordae (Fig.5.15). As the low-resolution CECT-based segmented network appeared to have many missing vessels, the blood vessels identified could not be considered an interconnected structure. Hence, it was not possible to evaluate the interconnectivity of vessels across different regions of the sample. This limitation highlights the need to study those structures at a higher spatial resolution with CECT and cryo-CECT to more accurately evaluate the number of vessels and branching running into the chordae. Nevertheless, these observations already support the hypothesis developed in recent studies that chordae tendineae are not avascular and the small degree of branching observed of the vessel in the chorda may indicate a limited supply of blood in the chordal tissue and raise some questions about the function of these vessels [36, 37].
In comparison with low-resolution CECT, high-resolution CECT (protocol n°2) and cryo-CECT (protocol n°3) imaging on the muscle insertion showed that multiple vessels (n=3) were present in the left chorda and right chorda (Fig.5.15.B). These vessels displayed a straight course with minimal branching as observable at low resolution. Vessels in the chordae were only located in the outer layer and none were observed in the core. This supports what has already been described in the literature (Fig.2.10) [12]. Vessels segmented based on high-resolution CECT and cryo-CECT are more interconnected in comparison to low-resolution CECT. This may be due to a higher resolution that could increase the visibility of the vessels and allow a faster and more accurate segmentation. High-resolution cryo-CECT (protocol n°4) allowed to segment of the vessels running in the chordae more easily due to an improvement of the contrast of the vessels with their surrounding in this region (Fig.5.13.D-H) and since those vessels are the ones of interest, cryo-CECT was used to qualitatively and quantitatively assess their microstructural parameters.

First, there is no observable connection between the three vessels identified running along the chordae and the vessels coming from the muscle (Fig.5.15.B). The three vessels originated only from the opposite side of the muscle. Moreover, no connection was identified when using high-resolution CECT (protocol n°2).
An image analysis workflow was developed to quantitatively assess the curved length and radius of two chosen

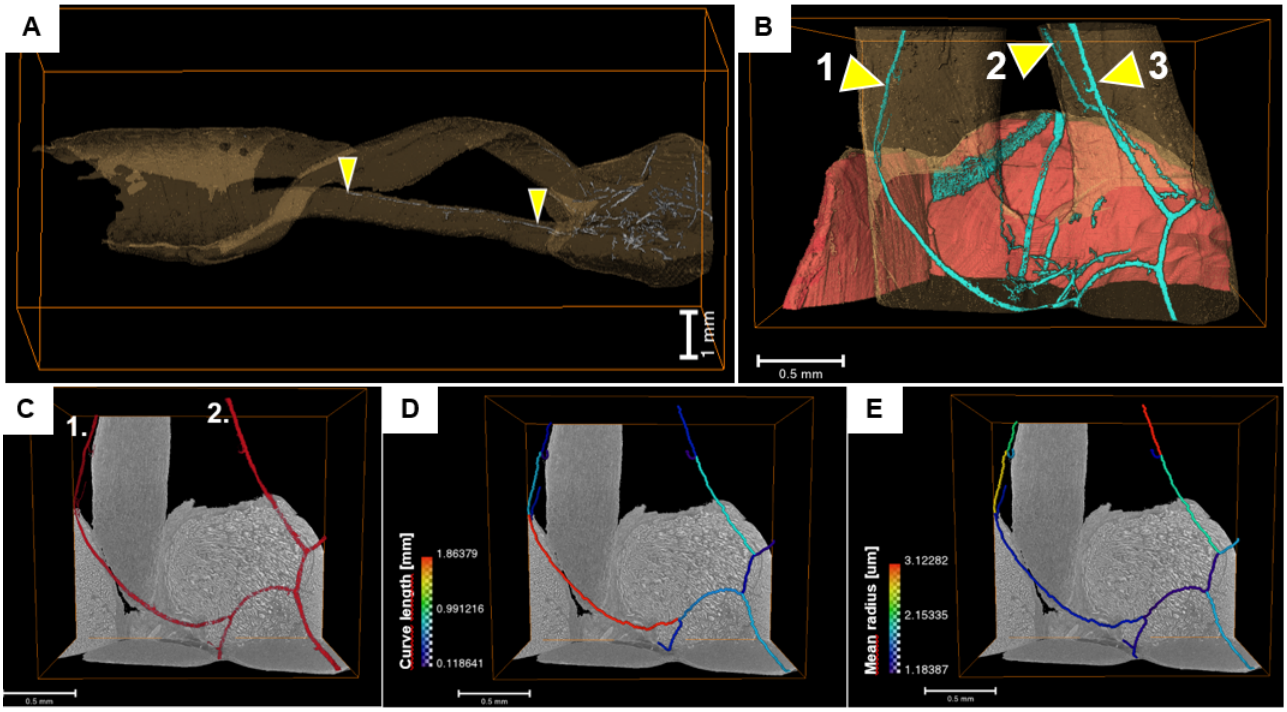

Figure 5.15: Quantitative assessment of the curved length and mean radius of the vessels running into the chordae. (A)3D rendering of the vessels segmented in the full volume of the sample obtained with low-resolution CECT. The surface of the sample is coloured orange and the vessels are white. A vessel runs through the left chorda until the middle of its length. Two vessels appear running respectively in the left and right chord. (B) 3D rendering of the muscle insertion region obtained with high-resolution cryo-CECT (protocol n°4), the muscle is segmented (pink), and the segmented vessels are visible (blue). 3 vessels are observable running along the chordae (yellow arrow). (C) 3D rendering of the two blood vessels quantitatively studied in (D-E) and shown in (B). (D) The curved length of the individual segments is represented and ranges from 0.12 to 1.9 mm. (C) The mean radius of the segments is visible, and the largest values are attributed to the upper segments. The full segmented vessel network using high-resolution CECT (protocol n°2) is available in the supplemental video (Supplementary video 5 [link: Video 5]).

vessels obtained with cryo-CECT (protocol n°4) (Fig.5.15.C). The assessment of the number of branching nodes, which was found to be 6, enabled the division of the selected vessels into segments with a curved length range of 0.1 to 0.9 mm. It is premature to classify the degree of branching as either low or high in this study, as no other chordae were investigated. Nonetheless, the curved length and number of branching nodes could be used in future studies to evaluate and compare the degree of branching and bifurcation of the segmented vessels in the chordae. This could provide valuable insight into understanding the causes and consequences of the presence of vasculature, and aid in determining the degree of branching and number of vessels in a healthy versus a diseased chordae. Interestingly, the mean radius computed increased while going up into the chord, and may be due to biological factors, or to limitation of the technique, and further investigations may be needed to determine the cause of this radius increase.

In conclusion, the present study shows that low-resolution CECT, high-resolution CECT and cryo-CECT allowed the visualisation in 3D of the vasculature in the chordae in a non-destructive fashion. Currently, blood vessels in the chordae tendineae have been exclusively studied using classical 2D histology [36, 37] that cannot inform accurately and non-destructively on the degree of branching and shape of the blood vessels in the chordae. Conversely, a 3D assessment gives valuable insets into the microstructural parameters needed in order to properly evaluate the role and proportion of the vessel observed in the chordae tendineae. Overall,

the results of this study proved the presence of vasculature in the chordae tendineae which has been disputed in the literature and gives insets about the function of those vessels based on their shape and the level of branching.

5.7 Leaflet insertion

High-resolution cryo-CECT of the leaflet insertion regions (protocol n°4) showed heterogeneously located layers and regions of different grey intensities. Although the contrast difference between these regions was highly variable, some layers appeared clearly while others were blurry (Fig.5.16). The interaction of the CESA suggested that the lighter area was comprised of more elastin fibres. In Section 2.2.2, the MV leaflet was described as having four layers, namely the spongiosa (0.2 elastin wt%), fibrosa (0.01 elastin wt%), ventricularis (0.5 elastin wt%) and atrialis (0.6 elastin wt%) [8]. Based on the grey value intensity of the regions and their position, it is likely that the darker zone (Fig.5.16(I)) corresponds to the fibrosa, while the lighter layer (Fig.5.16(II)) may be related to the spongiosa. The thin light layer (Fig.5.16(III)) could correspond to a layer of endothelial cells, atrialis or ventricularis. According to the literature, the atrialis and ventricularis should be adjacent to the spongiosa and fibrosa, respectively, which would suggest that these layers are distinguishable. However, this distinction is not observed in our study (Fig.5.16.B). The chordae tendineae examined in this study were identified as marginal chordae inserted at the leaflet edge and may explain why the layers cannot be differentiated. At the leaflet edge, the outer layer of the chordae merges with both layers, whereas secondary chordae, which only insert in the rough zone of the leaflet, only merge with the ventricularis. This distinction between marginal and secondary chordae suggests that microstructural differences would likely be observed if a secondary chordae was imaged using the same protocol. Therefore, caution should be exercised in investigating the location and insertion sites of the chordae which would likely help to better comprehend its microstructure at the insertion into the leaflet.
While the highly stained outer layer of the sample assimilated to the ventricularis, atrialis and endothelial cells was visually distinguishable throughout the leaflet insertion, it was not the case for the layers identified as the spongiosa and fibrosa because their shape, thickness and overall contrast between each other varied a lot along the sample. While they were visually distinguishable on top (Fig.5.16.B), they were difficult to follow and accurate segmentation in 3D was not possible (Fig.5.16.C-D-F). It was therefore difficult at the current stage to assert the true nature of a given region in the sample, and an assessment of the sample's microstructure in this area using classical 2D histology is required.

Since the described layers (Fig.5.16.B) cannot or difficulty be followed from top to bottom (Fig.5.16.B-C-D). A qualitative investigation of these layers was performed on a subvolume where both the hypothetical spongiosa and fibrosa could be identified (Fig.5.16.G). The 3D rendering allowed to visually assess the difference between those regions. The lighter region (II) is comprised of more connective tissue, and hence the overall orientation of the fibres could not be visually assessed. The darker region (I) is comprised of less elastin, the overall orientation of the fibres can be visually assessed with fibres running parallel to the surface of the sample. With high-resolution cryo-CECT (protocol n°4), the lighter and outer layer of the

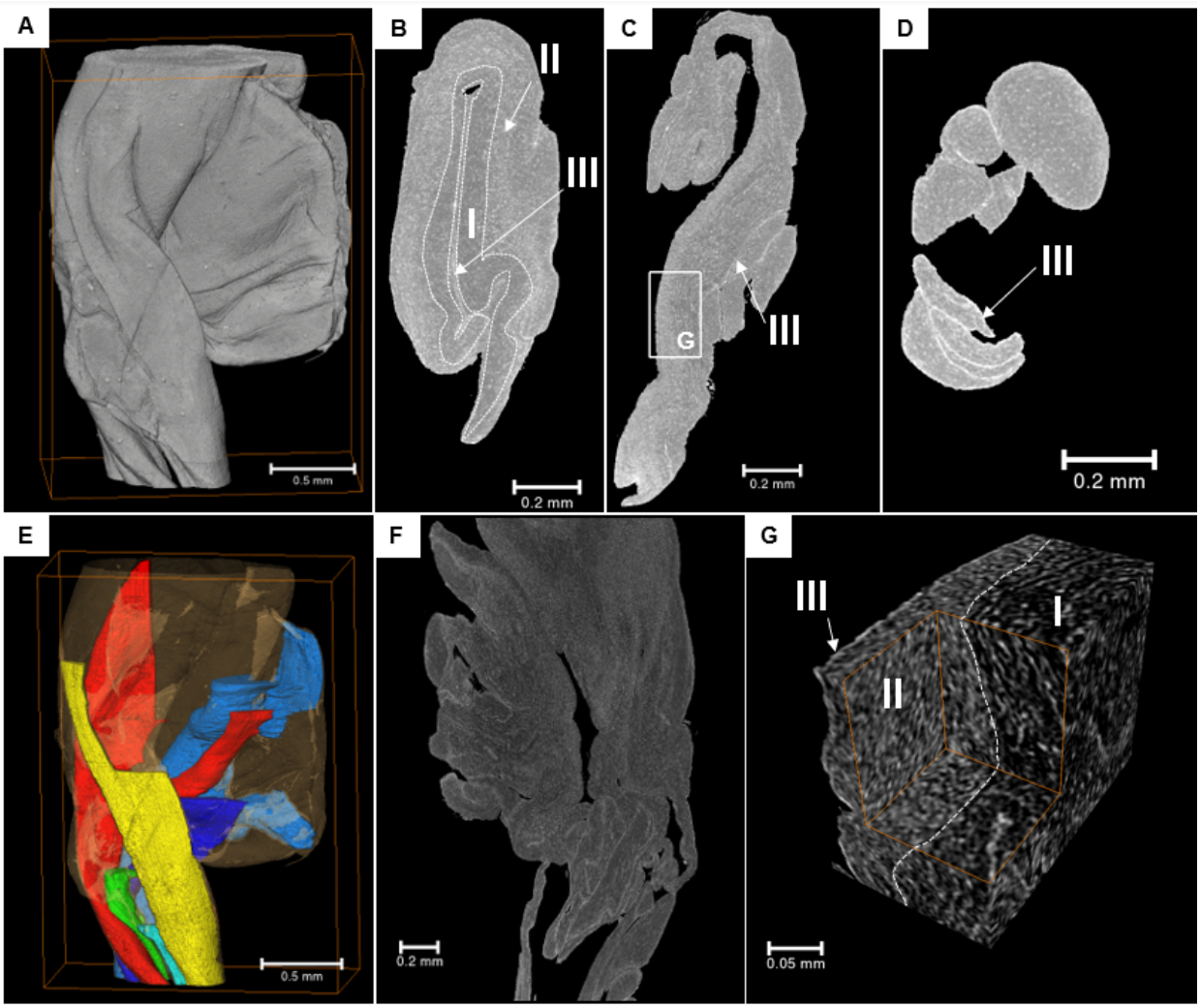

Figure 5.16: Qualitative and quantitative assessment of the leaflet insertion of the chordal layers visibility and the number of chordae tendineae. In (B-C-D-G), (I) indicates the darker layers referred to as the fibrosa, (II) to the lighter layer, referred to as the spongiosa and (III) the thin surrounding lighter layer referred to as the ventricularis, atrialis or endothelial cells. (A) 3D rendering of the leaflet insertion region with high-resolution cryo-CECT (protocol n°4). (B) Axial section in the upper part of the region, (C) Axial section in the middle part of the region. (D) An axial section in the bottom part of the region. (E) 3D rendering of individually segmented chordae. (F) Sagital section of the leaflet insertion. (G) 3D subvolume with both layers visible.

chordae (Fig.5.16.D(III)) could be identified in the sample allowing segmentation and visualisation of chordae sub-branches (Fig.5.16.E) that were previously not visible. This outer layer could also be seen in the sagital section (Fig.5.16.F) and helped to differentiate the different sub-branches to a certain extent. A total of 8 sub-branches can be identified before insertion into the leaflet (Fig.5.16.D). Some could be followed high into the leaflet insertion and separated into sub-branches while others were only identified in the lower part. Overall, compared to the muscle insertion obtained with the same high-resolution cryo-CECT protocol (protocol n°4), the individual collagen fibres were less visible and barely distinguishable.

In summary, the results obtained from the leaflet insertion raise some questions regarding the actual number of observable chordae in the mitral valve. Visual inspection distinguished two chordae, while low-resolution CECT showed three, and high-resolution cryo-CECT counted up to 8, suggesting that previous studies relying solely on visual inspection and low-resolution techniques may underestimate the number of

chordae and sub-branches. The study also emphasized the significance of proper sample mounting as the different chordae were not separated and were compressed against each other, making image processing and analysis challenging.

5.8 Chordal layers

Qualitative and quantitative assessment of the centre of the chordae and the layers composing it were investigated on subvolumes from the upper part of the muscle insertion (Fig.5.17.A) and from the lower part of the leaflet insertion (Fig.5.17.B), both obtained using high-resolution cryo-CECT (protocol n°4). With this technique, the outer laminae surrounding the chordae before insertion into the muscle (Fig.5.17.B) are not visible before the leaflet (Fig.5.17.E). The shape and number of identified laminae varied depending on the location in the sample. While this number varied between both subvolumes, quantitative assessment of the number of laminae in the region where they were visible also revealed heterogeneity in the axial plane (Fig.5.17.C) and through the height of the sample (Fig.5.17.F). While the elastin-rich layer has already been described surrounding the chordae core, investigations on the number of those laminae composing it and their variation are scarce. In a previous study, µCT was used to investigate the layers of the chordae tendineae, enabling differentiation between the endothelial layer, spongiosa, and fibrosa, which correspond to the elastin-rich layer and the core of the chordae, respectively [87]. However, no laminae were observed inside the spongiosa then, nor using our CECT protocols developed in this current study. Hence, it is likely that cryo-CECT provides better visualization of these structures and may be preferred for further investigations.

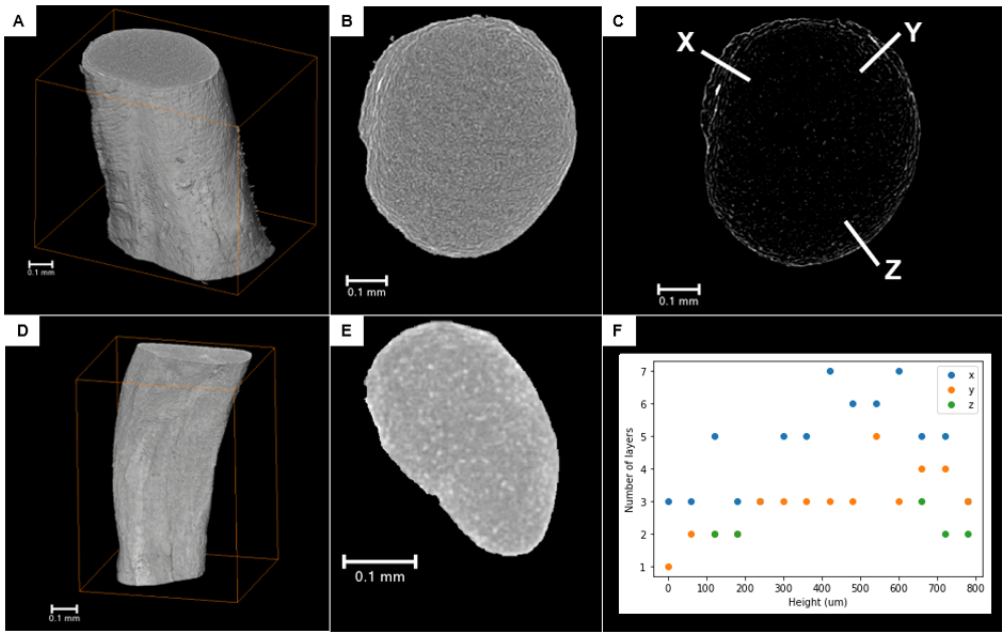

Figure 5.17: Quantitive and qualitative assessment of the number of elastin laminae.(A) 3D rendering of a chorda above muscle insertion. (B)The 2D axial section of the chorda is shown in (A). (C) Oversaturated section with three sections (x,y,z) and the layers visible. (D) 3D rendering of a chorda below the leaflet insertion. (E) 2D axial section of the chorda is available in (D). (F) Variation of the number of layers from bottom to top in the 3 sections (x,y,z) visible above in (C).

6 General conclusion and further perspective

The objectives of this master thesis encompassed three main aspects. Firstly, we aimed to develop a suitable sample preparation and mounting methodology for chordae tendineae, including the design of an effective sample holder. Subsequently, various acquisition parameters such as spatial resolution and freezing conditions were optimized, and their influence on image quality was assessed. Lastly, the investigation focused on evaluating the utility of CECT and cryo-CECT in enhancing the visualization of key structures of interest within the chordae tendineae. This comparative analysis aimed to highlight the advantages and limitations of the novel imaging techniques in relation to the conventional approach employed in previous studies. Furthermore, this research served as a pioneering endeavour in the field, acting as a proof of concept to validate the feasibility and effectiveness of employing CECT and cryo-CECT for the anatomical and microstructural characterization of chordae tendineae. By successfully demonstrating the use of these advanced imaging techniques, this study lays the foundation and paves the way for future investigations and advancements in the field of chordae tendineae analysis. It opens up opportunities for further studies to explore the vast potential and possibilities that these innovative imaging modalities offer.

The key messages derived from this study have important implications for future research in the field of chordae tendineae analysis. Firstly, the development of an appropriate sample holder that accounts for mechanical deformation is crucial for achieving accurate and reliable imaging results. The ability to maintain the structural integrity of the chordae tendineae during imaging is essential to ensure that the observed microstructures and morphological features are representative of their natural state. In order to achieve these objectives, future studies should consider the development of application-specific sample holders that enable the acquisition of the complete mitral valve apparatus, including the chordae tendineae, at low resolution. Additionally, there is a need for the development of sample holders capable of conducting mechanical testing on the chordae tendineae to assess microstructural variations under specific loading conditions. These advancements in sample holder design and functionality will facilitate a comprehensive understanding of the mechanical behaviour and microstructural changes of the chordae tendineae, further enhancing our knowledge in this field.

Secondly, this study emphasizes the complementarity of CECT and cryo-CECT for assessing the chordae tendineae anatomy and microstructure. Depending on the specific research question, one technique may

be preferable to the other. For instance, high-resolution cryo-CECT allows for the visualization of collagen, elastin and muscle fibres, whereas CECT is more suitable for identifying adipocytes. Additionally, it is important to note that while our high-resolution imaging provides enhanced image quality compared to low-resolution, even low-resolution imaging can have valuable applications and provide valuable insights into the micro- and macrostructure of the chordae tendineae. Moreover, this study highlights the advantages and limitations of both techniques based on the research question at hand. Currently, some challenges remain, such as the limited visibility of fibres at the leaflet insertion compared to the muscle insertion and the inability to segment individual fibres. Therefore, future studies should explore alternative freezing temperatures to determine the optimal temperature for visualizing chordae fibres and to enable the segmentation of individual fibres. These investigations will contribute to the refinement and improvement of cryo-CECT methodology for better characterization of the chordae tendineae microstructure. Furthermore, our study does not presently encompass a comparative analysis between the images acquired through our CECT and cryo-CECT protocols and classical 2D histology. Nonetheless, this analysis is currently underway, and an evaluation of the findings presented in this study alongside classical 2D histology is intended.
Finally, in this study, a comprehensive assessment of the morphology and microstructure of one chordae tendineae sample was conducted. One notable finding was the presence of vasculature, which had been a subject of debate in previous studies. Both CECT and cryo-CECT techniques provided a 3D investigation of each substructure, offering new insights and addressing some of the limitations reported in earlier research. Moving forward, it is recommended that further studies focus on employing CECT and cryo-CECT to examine additional chordae tendineae samples. These techniques have the potential for comparative studies, enabling a deeper understanding of the morphological and microstructural differences between different types of chordae tendineae, such as first and second-order chordae. Such investigations would help account for intra-variability within individuals and inter-variability across different donors, ultimately enhancing our knowledge of chordae tendineae ruptures and associated diseases. Furthermore, analyses could be conducted to compare the proportion and distribution of substructures, including blood vessels and adipose tissue, in healthy and diseased tissues. This would provide insights into their functions and whether their presence is consistent or associated with specific diseases. Additionally, a comparative study involving different species, such as sheep, cow, and human, could be undertaken to assess the applicability of findings from animal models to human cases.

In summary, even if challenges remain, we think that further studies utilizing CECT and cryo-CECT techniques have the potential to expand our understanding of chordae tendineae by addressing intra- and inter-variability, comparing healthy and diseased tissues, investigating cross-species differences, and improving MV models. Such investigations will contribute to advancements in the treatment and management of chordae tendineae-related conditions.

Bibliography

[1] Unraveling the etiologies of discrete subaortic stenosis: A focus on left ventricular outflow tract hemodynamics. https://corescholar.libraries.wright.edu/cgi/viewcontent.cgi?article=3620&context=etd_all. (Accessed on 12/17/2022).

[2] Valve mitrale - incci. https://www.incci.lu/fr/les_maladies/maladie-2/valve-mitral/. (Accessed on 12/17/2022).

[3] Marvin H Eng, Tiberio Frisoli, Dee Dee Wang, and William W O'Neill. Transcatheter mitral valve therapy: Repair and replacement. *Current Cardiovascular Risk Reports*, 13:1–8, 2019.

[4] Mitral leaflet anatomy revisited - sciencedirect. https://www.sciencedirect.com/science/article/pii/S002252230801670X?via%3Dihub. (Accessed on 10/30/2022).

[5] Chordae tendinae — mitral valve repair center. https://www.mitralvalverepair.org/chordae-tendinae. (Accessed on 11/17/2022).

[6] Ranganathan N Lam JH Wigle ED. Silver md. morphology of the human mitral valve. ii. the value leaflets. *Circulation*, 41:459–467, 1970.

[7] Mohammad Javad Sadeghinia, Bjørn Skallerud, Gerhard A Holzapfel, and Victorien Prot. Biomechanics of mitral valve leaflets: Second harmonic generation microscopy, biaxial mechanical tests and tissue modeling. *Acta biomaterialia*, 141:244–254, 2022.

[8] Chung-Hao Lee, Christopher A Carruthers, Salma Ayoub, Robert C Gorman, Joseph H Gorman III, and Michael S Sacks. Quantification and simulation of layer-specific mitral valve interstitial cells deformation under physiological loading. *Journal of theoretical biology*, 373:26–39, 2015.

[9] Stephen Karas Jr and Ronald C Elkins. Mechanism of function of the mitral valve leaflets, chordae tendineae and left ventricular papillary muscles in dogs. *Circulation research*, 26(6):689–696, 1970.

[10] Muralidhar Padala, Michael S Sacks, Shasan W Liou, Kartik Balachandran, Zhaoming He, and Ajit P Yoganathan. Mechanics of the mitral valve strut chordae insertion region. 2010.

[11] Colton J Ross, Junnan Zheng, Liang Ma, Yi Wu, and Chung-Hao Lee. Mechanics and microstructure of the atrioventricular heart valve chordae tendineae: a review. *Bioengineering*, 7(1):25, 2020.

[12] Jennifer Ritchie, James N Warnock, and Ajit P Yoganathan. Structural characterization of the chordae tendineae in native porcine mitral valves. *The Annals of thoracic surgery*, 80(1):189–197, 2005.

[13] John J Fenoglio Jr, Tuan Duc Pham, Andrew L Wit, Arthur L Bassett, and Bernard M Wagner. Canine mitral complex: ultrastructure and electromechanical properties. *Circulation research*, 31(3):417–430, 1972.

[14] Ling Chen, Ph. D Frank CP Yin, MD, and Karen May-Newman, Ph. D. The structure and mechanical properties of the mitral valve leaflet-strut chordae transition zone. *J. Biomech. Eng.*, 126(2):244–251, 2004.

[15] Keping Zuo, Thuy Pham, Kewei Li, Caitlin Martin, Zhaoming He, and Wei Sun. Characterization of biomechanical properties of aged human and ovine mitral valve chordae tendineae. *Journal of the mechanical behavior of biomedical materials*, 62:607–618, 2016.

[16] José M Icardo, Elvira Colvee, and José M Revuelta. Structural analysis of chordae tendineae in degenerative disease of the mitral valve. *International journal of cardiology*, 167(4):1603–1609, 2013.

[17] Jesper Hjortnaes, Josh Keegan, Patrick Bruneval, Eugenia Schwartz, Frederick J Schoen, Alain Carpentier, Robert A Levine, Albert Hagège, and Elena Aikawa. Comparative histopathological analysis of mitral valves in barlow disease and fibroelastic deficiency. In *Seminars in Thoracic and Cardiovascular Surgery*, volume 28, pages 757–767. Elsevier, 2016.

[18] Tirone E David, Joanne Bos, and Harry Rakowski. Mitral valve repair by replacement of chordae tendineae with polytetrafluoroethylene sutures. *The Journal of thoracic and cardiovascular surgery*, 101(3):495–501, 1991.

[19] Lisa Leyssens, Camille Pestiaux, and Greet Kerckhofs. A review of ex vivo x-ray microfocus computed tomography-based characterization of the cardiovascular system. *International Journal of Molecular Sciences*, 22(6):3263, 2021.

[20] Arne Maes, Camille Pestiaux, Alice Marino, Tim Balcaen, Lisa Leyssens, Sarah Vangrunderbeeck, Grzegorz Pyka, Wim M De Borggraeve, Luc Bertrand, Christophe Beauloye, et al. Cryogenic contrast-enhanced microct enables nondestructive 3d quantitative histopathology of soft biological tissues. *Nature communications*, 13(1):1–14, 2022.

[21] Jo Henkel. Mechanics of Heart Valves - Cardiovascular Systems, July 2022.

[22] Jason A. Shar. Unraveling the etiologies of discrete subaortic stenosis: A focus on left ventricular outflow tract hemodynamics. https://corescholar.libraries.wright.edu/cgi/viewcontent.cgi?article=3620&context=etd_all, 2021. (Accessed on 10/30/2022).

[23] Jennifer Ritchie. The material properties of the chordae tendineae of the mitral valve: An in vitro investigation. https://smartech.gatech.edu/bitstream/handle/1853/5892/Ritchie_Jennifer_L_200412_MS.pdf?sequence=1&isAllowed=y. (Accessed on 10/30/2022).

[24] Augustinas Tumenas, Laima Tamkeviciute, Reda Arzanauskiene, and Monika Arzanauskaite. Multimodality imaging of the mitral valve: Morphology, function, and disease. *Current Problems in Diagnostic Radiology*, 50(6):905–924, 2021.

[25] Karen P McCarthy, Liam Ring, and Bushra S Rana. Anatomy of the mitral valve: understanding the mitral valve complex in mitral regurgitation. *European Journal of echocardiography*, 11(10):i3–i9, 2010.

[26] Martin Misfeld and Hans-Hinrich Sievers. Heart valve macro-and microstructure. *Philosophical Transactions of the Royal Society B: Biological Sciences*, 362(1484):1421–1436, 2007.

[27] Siew Yen Ho. Anatomy of the mitral valve. *Heart*, 88(suppl 4):iv5–iv10, 2002.

[28] Jun Liao and Ivan Vesely. A structural basis for the size-related mechanical properties of mitral valve chordae tendineae. *Journal of biomechanics*, 36(8):1125–1133, 2003.

[29] Michael G. Bateman, Jason L. Quill, and Alexander J. Hill. *Detailed anatomical and functional features of the cardiac valves*. 2015. Cited by: 0.

[30] Carla Stecco. *Functional atlas of the human fascial system*. Elsevier Health Sciences, 2014.

[31] Sotirios Korossis. *Structure-function relationship of heart valves in health and disease*. IntechOpen, 2018.

[32] Connective tissue: The histology guide. https://www.histology.leeds.ac.uk/tissue_types/connective/connective_groundS.php. (Accessed on 11/15/2022).

[33] Luciana Wang Gusukuma, José Carlos Prates, and Ricardo Luiz Smith. Arquitectura de las cuerdas tendinosas en la union con el musculo papilar. *International Journal of Morphology*, 22(4):267–272, 2004.

[34] J Hutchison and P Rea. A comparative study of the morphology of mammalian true chordae tendineae of the atrioventricular valves. *Journal of Morphological Sciences*, 32(02):071–077, 2015.

[35] M Cocchieri and G Bardelli. False chordae tendineae. *Minerva Cardioangiologica*, 40(10):353–358, 1992.

[36] Narbada Saini, Uma Nahar Saikia, Daisy Sahni, and Rana Sandip Singh. Vascularity of human atrioventricular valves: A myth or fact? *The Journal of Thoracic and Cardiovascular Surgery*, 147(1):517–521, 2014.

[37] Is tendon vascular or avascular? – short-facts. https://short-facts.com/is-tendon-vascular-or-avascular/. (Accessed on 11/17/2022).

[38] Jun Liao and Ivan Vesely. Skewness angle of interfibrillar proteoglycans increases with applied load on mitral valve chordae tendineae. *Journal of biomechanics*, 40(2):390–398, 2007.

[39] Milan Toma, Charles H Bloodworth, Eric L Pierce, Daniel R Einstein, Richard P Cochran, Ajit P Yoganathan, and Karyn S Kunzelman. Fluid-structure interaction analysis of ruptured mitral chordae tendineae. *Annals of biomedical engineering*, 45(3):619–631, 2017.

[40] Anastassia Pokutta-Paskaleva, Fatiesa Sulejmani, Marissa DelRocini, and Wei Sun. Comparative mechanical, morphological, and microstructural characterization of porcine mitral and tricuspid leaflets and chordae tendineae. *Acta Biomaterialia*, 85:241–252, 2019.

[41] Alexandra A Degandt, Patricia A Weber, Hashim A Saber, and Carlos MG Duran. Mitral valve basal chordae: comparative anatomy and terminology. *The Annals of thoracic surgery*, 84(4):1250–1255, 2007.

[42] Uri Gabbay and Chaim Yosefy. The underlying causes of chordae tendinae rupture: a systematic review. *International journal of cardiology*, 143(2):113–118, 2010.

[43] Eusebio Real, José Manuel Icardo, Gaspar Fernández-Barreras, José Manuel Revuelta, Marta Calvo Díez, Alejandro Pontón, José Francisco Gutiérrez, José Miguel López Higuera, and Olga María Conde. Identification of human pathological mitral chordae tendineae using polarization-sensitive optical coherence tomography. *Sensors*, 19(3):543, 2019.

[44] KOON O Lim and DR Boughner. Morphology and relationship to extensibility curves of human mitral valve chordae tendineae. *Circulation research*, 39(4):580–585, 1976.

[45] Glycosaminoglycan profiles of myxomatous mitral leaflets and chordae parallel the severity of mechanical alterations — journal of the american college of cardiology. https://www.jacc.org/doi/abs/10.1016/S0735-1097(03)00626-0. (Accessed on 11/18/2022).

[46] Thomas A Orszulak, Hartzell V Schaff, Gordon K Danielson, Jeffrey M Piehler, James R Pluth, Robert L Frye, Dwight C McGoon, and Lila R Elveback. Mitral regurgitation due to ruptured chordae tendineae: early and late results of valve repair. *The Journal of Thoracic and Cardiovascular Surgery*, 89(4):491–498, 1985.

[47] Paul WM Fedak, Patrick M McCarthy, and Robert O Bonow. Evolving concepts and technologies in mitral valve repair. *Circulation*, 117(7):963–974, 2008.

[48] Computational modeling. https://www.nibib.nih.gov/science-education/science-topics/computational-modeling. (Accessed on 11/20/2022).

[49] Andrew W Siefert, Jean-Pierre M Rabbah, Eric L Pierce, Karyn S Kunzelman, and Ajit P Yoganathan. Quantitative evaluation of annuloplasty on mitral valve chordae tendineae forces to supplement surgical planning model development. *Cardiovascular engineering and technology*, 5(1):35–43, 2014.

[50] Amir H Khalighi, Andrew Drach, Charles H Bloodworth, Eric L Pierce, Ajit P Yoganathan, Robert C Gorman, Joseph H Gorman, and Michael S Sacks. Mitral valve chordae tendineae: topological and geometrical characterization. *Annals of biomedical engineering*, 45(2):378–393, 2017.

[51] Amir H Khalighi, Bruno V Rego, Andrew Drach, Robert C Gorman, Joseph H Gorman, and Michael S Sacks. Development of a functionally equivalent model of the mitral valve chordae tendineae through topology optimization. *Annals of biomedical engineering*, 47(1):60–74, 2019.

[52] Heart imaging: Benefits, risks, types, preparation. https://www.medicalnewstoday.com/articles/heart-imaging. (Accessed on 12/18/2022).

[53] David Tibor Lauber, András Fülöp, Tibor Kovács, Krisztián Szigeti, Domokos Máthé, and Attila Szijártó. State of the art in vivo imaging techniques for laboratory animals. *Laboratory animals*, 51(5):465–478, 2017.

[54] GARY S Mintz, MORRIS N Kotler, BERNARD L Segal, and WAYNE R Parry. Two-dimensional echocardiographic recognition of ruptured chordae tendineae. *Circulation*, 57(2):244–250, 1978.

[55] THOMAS SWEATMAN, ARTHUR SELZER, MASANOBU KAMAGAKI, KEITH COHN, and Judith Basford. Echocardiographic diagnosis of mitral regurgitation due to ruptured chordae tendineae. *Circulation*, 46(3):580–586, 1972.

[56] Patrick Carnahan, John Moore, Daniel Bainbridge, Elvis CS Chen, and Terry M Peters. Multi-view 3d transesophageal echocardiography registration and volume compounding for mitral valve procedure planning. *Applied Sciences*, 12(9):4562, 2022.

[57] Lan Lan, Huijuan Hu, Wenbo Sun, Rongqing Sun, Gonghao Ling, Tingyi Du, Xuan Li, Jianmin Yuan, Yaowen Xing, Xiaopeng Song, et al. Feasibility of cardiovascular magnetic resonance imaging at 5t in comparison to 3t. 2022.

[58] Jia Tao, Fujian Duan, Jili Long, Qinglong Meng, Bing Zhang, Zhenhui Zhu, and Hao Wang. The role of the submitral apparatus in hypertrophic obstructive cardiomyopathy. *Journal of the American Society of Echocardiography*, 2022.

[59] Reza Reyaldeen, Simrat Kaur, Amar Krishnaswamy, Jay Ramchand, Habib Layoun, Paul Schoenhagen, Rhonda Miyasaka, Shinya Unai, Samir R Kapadia, and Serge C Harb. Role of cardiac computed tomography in planning transcatheter mitral valve replacement (tmvr). *Current Cardiology Reports*, pages 1–16, 2022.

[60] Bo Wang, Leslie N Sierad, Jeremy J Mercuri, Agneta Simionescu, Dan T Simionescu, Lakiesha N Williams, Ryan Vela, Pietro Bajona, Matthias Peltz, Sharan Ramaswamy, et al. Structural and biomechanical characterizations of acellular porcine mitral valve scaffolds: anterior leaflets, posterior leaflets, and chordae tendineae. *Engineered Regeneration*, 3(4):374–386, 2022.

[61] Yaling Shi and Ivan Vesely. Characterization of statically loaded tissue-engineered mitral valve chordae tendineae. *Journal of Biomedical Materials Research Part A: An Official Journal of The Society for Biomaterials, The Japanese Society for Biomaterials, and The Australian Society for Biomaterials and the Korean Society for Biomaterials*, 69(1):26–39, 2004.

[62] JA Ramos-Vara and MA Miller. When tissue antigens and antibodies get along: revisiting the technical aspects of immunohistochemistry—the red, brown, and blue technique. *Veterinary pathology*, 51(1):42–87, 2014.

[63] Camille Pestiaux, Louise Quirynen, Christophe Beauloye, Jean-Louis Vanoverschelde, and Greet Kerckhofs. Ex vivo microfocus computed tomography and contrast-enhanced computed tomography applied to heart valves. In *8th Belgian symposium on Tissue Engineering*, 2021.

[64] Agata Krawczyk-Ożóg, Mateusz K. Hołda, Danuta Sorysz, Mateusz Koziej, Zbigniew Siudak, Dariusz Dudek, and Wiesława Klimek-Piotrowska. Morphologic variability of the mitral valve leaflets. *The Journal of Thoracic and Cardiovascular Surgery*, 154(6):1927–1935, 2017.

[65] Shengda Chen, Candra Ratna Sari, Hao Gao, Yang Lei, Patrick Segers, Matthieu De Beule, Guixue Wang, and Xingshuang Ma. Mechanical and morphometric study of mitral valve chordae tendineae and related papillary muscle. *journal of the mechanical behavior of biomedical materials*, 111:104011, 2020.

[66] Brian D Metscher. Microct for comparative morphology: simple staining methods allow high-contrast 3d imaging of diverse non-mineralized animal tissues. *BMC physiology*, 9(1):1–14, 2009.

[67] A. P. Ginsberg. *Inorganic Syntheses*. Wiley, 2009.

[68] A. Maes. Cryogenic contrast-enhanced microct enables nondestructive 3d quantitative histopathology of soft biological tissues (github, 2020). https://doi.org/10.5281/zenodo.7034265.

[69] Elongation of chordae tendineae as an adaptive process to reduce mitral regurgitation in functional mitral regurgitation — european heart journal - cardiovascular imaging — oxford academic. https://academic.oup.com/ehjcimaging/article/17/5/500/1745584. (Accessed on 05/20/2023).

[70] Hyab Mehari Abraha, Sina Javadpour, Sandra Sunil, Fergal O'Brien, and Claire Conway. Contrast-enhanced μct for ex-vivo digital reconstruction of whole heart and mitral valve in an aged population. *Tissue Engineering Research Group, Anatomy & Regenerative Medicine, Royal College of Surgeons in Ireland (RCSI), Ireland; Trinity Centre for BioEngineering (TCBE), Trinity College Dublin (TCD), Ireland; Advanced Materials and Bioengineering Research Centre (AMBER), Ireland*, 2021.

[71] Anatomic, histologic, and two-dimensional–echocardiographic evaluation of mitral valve anatomy in dogs in: American journal of veterinary research volume 72 issue 9 (). https://avmajournals.avma.org/view/journals/ajvr/72/9/ajvr.72.9.1186.xml. (Accessed on 05/05/2023).

[72] New insight into the role of lipid metabolism-related proteins in rheumatic heart valve disease — lipids in health and disease — full text. https://lipidworld.biomedcentral.com/articles/10.1186/s12944-022-01722-x. (Accessed on 05/05/2023).

[73] Full article: Mapping body fat distribution: A key step towards the identification of the vulnerable patient? https://www.tandfonline.com/doi/full/10.3109/07853890.2011.605387. (Accessed on 05/05/2023).

[74] Three-dimensional imaging of the fibrous microstructure of achilles tendon entheses in mus musculus - sartori - 2018 - journal of anatomy - wiley online library. https://onlinelibrary.wiley.com/doi/full/10.1111/joa.12837. (Accessed on 05/05/2023).

[75] A quality optimization approach to image achilles tendon microstructure by phase-contrast enhanced synchrotron micro-tomography — scientific reports. https://www.nature.com/articles/s41598-021-96589-w. (Accessed on 05/05/2023).

[76] Sci-hub — the structure of rat tail tendon — 10.3109/03008208509089839. https://sci-hub.hkvisa.net/10.3109/03008208509089839. (Accessed on 05/05/2023).

[77] Ijms — free full-text — ppars-orchestrated metabolic homeostasis in the adipose tissue. https://www.mdpi.com/1422-0067/22/16/8974. (Accessed on 05/05/2023).

[78] Sci-hub — histology of the stroma in developing rat subcutaneous adipose tissue — 10.2527/jas1982.5561336x. https://sci-hub.hkvisa.net/10.2527/jas1982.5561336x. (Accessed on 05/05/2023).

[79] Bio-friction — springerlink. https://link.springer.com/article/10.1007/s40544-013-0004-4. (Accessed on 05/05/2023).

[80] Structural and biochemical characteristics of various white adipose tissue depots - wronska - 2012 - acta physiologica - wiley online library. https://onlinelibrary.wiley.com/doi/epdf/10.1111/j.1748-1716.2012.02409.x. (Accessed on 05/05/2023).

[81] Adipose-tissue plasticity in health and disease - sciencedirect. https://www.sciencedirect.com/science/article/pii/S0092867421014549#sec2. (Accessed on 05/05/2023).

[82] Julia F Barrett and Nicholas Keat. Artifacts in ct: recognition and avoidance. *Radiographics*, 24(6):1679–1691, 2004.

[83] Bioengineering — free full-text — mechanics and microstructure of the atrioventricular heart valve chordae tendineae: A review. https://www.mdpi.com/2306-5354/7/1/25. (Accessed on 05/06/2023).

[84] Nathan S Jeffery, Robert S Stephenson, James A Gallagher, Jonathan C Jarvis, and Philip G Cox. Micro-computed tomography with iodine staining resolves the arrangement of muscle fibres. *Journal of biomechanics*, 44(1):189–192, 2011.

[85] Pekka Kannus. Structure of the tendon connective tissue. *Scandinavian journal of medicine & science in sports*, 10(6):312–320, 2000.

[86] Greet Kerckhofs, Steve Stegen, Nick Van Gastel, Annelies Sap, Guillaume Falgayrac, Guillaume Penel, Marjorie Durand, Frank P Luyten, Liesbet Geris, Katleen Vandamme, et al. Simultaneous three-dimensional visualization of mineralized and soft skeletal tissues by a novel microct contrast agent with polyoxometalate structure. *Biomaterials*, 159:1–12, 2018.

[87] Shannon entropy as a reliable score to diagnose human fibroelastic degenerative mitral chords: A micro-ct ex-vivo study - sciencedirect. https://www.sciencedirect.com/science/article/pii/S1350453322001679. (Accessed on 05/07/2023).

UNIVERSITÉ CATHOLIQUE DE LOUVAIN
École polytechnique de Louvain
Rue Archimède, 1 bte L6.11.01, 1348 Louvain-la-Neuve, Belgique | **www.uclouvain.be/epl**